Development of Quantitative Multi-spectral Fluorescence Endoscopic Imaging for Early Cancer Detection

Chenying Yang

A dissertation
submitted in partial fulfillment of the
requirements for the degree of

Doctor of Philosophy

University of Washington

2014

Reading Committee:
Eric J. Seibel, Chair
Linda G. Shapiro
Ruikang Wang

Program Authorized to Offer Degree:
Department of Bioengineering

University of Washington

Abstract

Development of Quantitative Multi-spectral Fluorescence
Endoscopic Imaging for Early Cancer Detection

Chenying Yang

Chair of the Supervisory Committee:
Professor Eric J. Seibel
Department of Mechanical Engineering

The incidence of esophageal adenocarcinoma has been rising in the western world with a low 5 year survival rate of less than 15%, but it can be treated when diagnosed early. However, conventional white light endoscopy screening has significant limitations because early cancerous lesions usually lie flat on the tissue surface and do not differ in contrast relative to the surrounding area. In an effort to detect early stages of cancer, fluorescence molecular imaging was developed since it improves diagnostic sensitivity and specificity through targeted visualization of multiple biomarkers at the cellular and sub-cellular level. This dissertation presents technologies and algorithms developed for real-time wide-field and quantitative multispectral fluorescence endoscopy for image-guided biopsies and resections. The body of work includes a realistic Barrett's esophagus phantom model development with calibrated fluorescence targets, enhanced visualization and documentation of diagnostic endoscopic records through image mosaicking, real-time compensation for fluorophore emission cross-talk and mitigation of background tissue autofluorescence for high contrast and quantitative molecular endoscopy. Although the scanning fiber endoscope technology forms the basis of the multispectral imaging that was implemented, the concepts, algorithms, and techniques can be applied to a wide range of *in vivo* and *in vitro* imaging technologies. In the long term, this work provides the foundation and framework of computer-aided quantitative endoscopy for personalized diagnosis and treatment.

Contents

List of Figures

List of Tables

ACKNOWLEDGMENTS

First and foremost, I am heartily thankful to my advisor, Professor Eric Seibel, whose continuous guidance, encouragement and support enabled me to develop both a deep and broad understanding of my research subject. This thesis would not have been possible without his thoughtful insight into the field and directions on problem formulations. Beyond my research subject, Eric also encouraged me to grow professionally as a scientist and engineer by always having my best interests in mind. He gave me many opportunities to attend and speak at international conferences and various public events. He has also been fully supportive of my interests in developing business skills through additional classes and projects that at times hindered my research progress.

I owe my deepest gratitude to my mentor, Dr. Len Nelson. This thesis would not have been completed without his diligent efforts and commitment, which not only influenced the content of the thesis but also shaped my research methodology. His curiosity and dedication to science and engineering has deeply influenced and inspired me. The knowledge and skills that I have learned from him will continue to guide me in the future.

I would like to thank the rest of my committee: Professor Linda Shapiro, Professor Paul Kinahan, Professor Matt O'Donnell, Professor Ruikang (Ricky) Wang, and Professor Xiaohu Gao for their encouragement, insightful comments, and direction.

I am grateful to my colleagues David Melville and Richard Johnston – their expertise and guidance have helped me tremendously not only on my research but also on being a good engineer. I would like to thank Vivian Hou for her insight and help for my project and her friendship and encouragement. I am thankful for my collaborators Emily Girard at Fred Hutchinson Cancer Research Center in Seattle, and Dr. Thomas Wang, Dr. Bishnu Joshi, Xiyu Duan and other Wang lab members at University of Michigan, Ann Arbor. I would like to thank Coherent Inc. in their

collaboration for my research experiment. Last but not least, the entire Human Photonics Laboratory contributed to important discussions and guided my development throughout this project.

Bioengineering is a young and exciting field, an arena where interdisciplinary research truly happens. Graduate school has been a fantastic once-in-a-lifetime experience, where I have learned and experienced the world and grown as an individual. I have had the fortune to not only dive into my thesis/research related subjects, but also learned to lead without authority, communicate effectively, and solve complex and ambiguous problems with a diverse group of people.

Meanwhile, I am grateful for all the friends I have made and people who have impacted my life. I am especially thankful to have met Nick Gedge, who has given me so much love and support. And I would never have imagined how much of a positive impact he has made in my life. I am looking forward to our exciting journey together.

I am completely indebted to my parents, for their unending love, infinite generosity and understanding, for not only giving me life, but also raising me to be a person with diligence, integrity, curiosity and grit. Without their support this achievement would not have been possible.

DEDICATION

to my family

1 Introduction

Molecular imaging has drawn increasing interest in clinical diagnosis because it enables the visualization of specific markers that track disease progression at the cellular and sub-cellular level. This intersection of electronic imaging and molecular biology opens up great potential for early cancer detection, quantitative assessments and more targeted/personalized treatment of diseases based on their specific molecular expression profiles.

Among a broad spectrum of molecular imaging techniques, modalities such as positron emission tomography (PET), single-photon-emission computed tomography (SPECT) and magnetic resonance imaging (MRI) have been combined with exogenously administered contrast agents to visualize *in vivo* tissue with molecular specificities. Additionally some of these technologies have been successfully translated to clinical applications and begun to impact patient care.

In the past few decades, with advancements in optical technologies and contrast agent chemistry, optical imaging has also brought unique capabilities to disease diagnosis. Optical imaging uses relatively simple instrumentation to image tissue reflectance, or emitted fluorescence light from endogenous or exogenous fluorophores. Compared to other diagnostic modalities, optical imaging can provide high resolution tissue surface imaging in real time, and therefore offers high resolution and sensitivity for the diagnosis of diseases arising from the tissue surface, such as surface tumor lesions in the GI tract.

Fluorescence imaging is one of the emerging optical molecular imaging techniques. Fluorescent molecular probes have been routinely been used to identify specific DNA components in flow cytometry systems, DNA microarrays, and in microscopic histology examinations such as fluorescence in situ hybridization (FISH). A variety of fluorophore optical probes are under

investigation for *in vivo* clinical imaging to identify pre or early stage cancerous conditions, and/or guide intraoperative visualization and delineation of tumor margins. For example, in gastrointestinal endoscopy, the combination of topically applied fluorescent molecular probes and wide-field multi-modal endoscopic devices can provide visualization of the spatial location of disease lesions at the cellular or sub-cellular level. Targeted disease probes combined with advanced endoscopic devices have already shown promise to enhance diagnostic sensitivity and specificity for the characterization of early cancerous lesions which originate from the mucosal surface of GI tract.

A major effort is currently underway to use molecular endoscopic imaging for the detection of high-grade dysplasia (HGD) and early stage adenocarcinoma in Barrett's esophagus. The incidence of esophageal adenocarcinoma (EAC) has been rising in the western world and can be deadly once the cancer has metastasized (5 year survival rate 10-15% [1]). The mucosa of Barrett's esophagus has a much greater risk of progression to cancer (30 to 125 times greater than normal esophagus [2]). Therefore, surveillance of patients with Barrett's esophagus is critical for early detection and localization of dysplasia. However, conventional white light endoscopy screening has significant limitations because high-grade dysplasia and early adenocarcinoma lesions usually lie flat on the tissue surface and are endoscopically "invisible" as they do not differ in appearance or contrast relative to the surrounding mucosa. Therefore, there is a need for a targeted molecular imaging strategy for early detection and prevention of cancer in patients with Barrett's esophagus. Furthermore, many tumors express multiple cell surface and proteomic markers and these molecular signatures are heterogeneous across patients and may also have a time dependence. Therefore, simultaneous multi-fluorophore imaging of numerous molecular targets is needed for increasing the sensitivity of cancer diagnosis and personalized treatment.

The goal of this research is to develop wide-field and quantitative multi-spectral fluorescence endoscopic technologies for the early stage detection of HGD lesions in Barrett’s esophagus when

effective treatment is feasible. This entails the development of algorithms and methodologies for quantitative fluorescence endoscopic imaging, which includes the development of a realistic Barrett's esophagus (BE) phantom model with calibrated fluorescence targets. Meanwhile there is also a need to develop methods which generate enhanced visualization of electronic patient diagnostic endoscopic records for longitudinal surveillance. Finally, wide-field multi-spectral fluorescence molecular imaging with mitigation of fluorophore emission cross-talk and reduced tissue autofluorescence background are evaluated and implemented in a newly developed endoscopic device for in human applications. More specifically, this research has the following specific aims:

- Specific Aim #1. Development of a quantitative wide-field fluorescence /reflectance scanning fiber endoscope (SFE).
- Specific Aim #2. Multi-spectral fluorescence SFE imaging with mitigation of spectral cross-talk and reduced background autofluorescence.
- Specific Aim #3. Provide clinical tools for increasing detection sensitivity and contrast ratio in disease diagnosis using multi-spectral fluorescence endoscopic imaging.

Development of a quantitative phantom model and a Distance Compensation algorithm for quantitative endoscopic fluorescence imaging is addressed by Specific Aim #1 and is discussed in Chapter 2. An endoscope image stitching algorithm for enhanced diagnostic visualization and patient record keeping is also addressed by Specific Aim #1 and is discussed in Chapter 3. Evaluation of approaches to eliminate fluorophore emission cross-talk and reduce background tissue autofluorescence is addressed by Specific Aim #2 and is discussed in Chapter 4. Development of a new multispectral SFE system, combined with implementation of algorithms and methodologies to improve the detection sensitivity and contrast ratio of fluorescence molecular imaging for clinical applications is addressed by Specific Aim #3 and discussed in Chapter 5. Importantly, this prototype system was delivered to our clinical collaborators at the

University of Michigan, and all *in vitro* results of this dissertation were demonstrated and taught to the collaborating engineers and physicians in Ann Arbor, Michigan. Methodologies and algorithms developed in this thesis were also implemented on other flexible endoscope systems such as a FITC Endoscopic Molecular Imaging System (Gastrointestinal Videoscope, GIF-Y0029, Olympus Corp.) [3]. Finally, future directions are addressed and challenges discussed in Chapter 6, together with conclusions.

2 Color-matched and fluorescence-labeled esophagus phantom and its applications

2.1 Introduction

Molecular imaging (also known as immunophotodiagnostic imaging) has drawn increasing interest in the field of diagnostic medicine because of its potential to target disease biomarkers for biopsy and diagnostic purposes [4] [5] [6] [7]. For example, in gastrointestinal endoscopy, the combination of fluorescence labeled molecular probes with wide-field multi-modal endoscopic devices can provide visualization of detailed biological information at the cellular or sub-cellular level, holding promise to enhance diagnosis and characterization of early cancer lesions in the GI tract [8] [9] [10]. In the development of these molecular imaging approaches, it is critical to have realistic, stable and reproducible optical phantoms, to calibrate endoscope systems and evaluate their performance. Moreover, crucial problems in molecular imaging such as biomarker quantification and mapping of probed disease lesions can be explored *in vitro* using these realistic phantom models [11] [12].

One application of molecular endoscopic imaging is the detection of high-grade dysplasia and early adenocarcinoma in Barrett's esophagus [13] [14]. The mucosa of Barrett's esophagus has a much greater risk of progression to cancer (30 to 125 times greater than normal esophagus [2]). Therefore, surveillance of patients with Barrett's esophagus is critical for early detection and localization of dysplasia. However, conventional white light endoscopy screening has significant limitations because high-grade dysplasia and early adenocarcinoma lesions usually lie flat on the tissue surface and are endoscopically "invisible" as they do not differ in appearance to the surrounding mucosa [6]. Therefore, there is a need for a targeted molecular imaging strategy for early detection and prevention of cancer in patients with Barrett's esophagus. Furthermore, topical application of targeted fluorescent probes is favored over intravenously administered

markers since regulatory limitations are less restrictive for short term exposure to surface contrast agents. Fluorescein dye and its derivatives are readily conjugated with low molecular weight peptides that will diffuse into the upper mucosal layers. Short wavelength light sources [13] [14] are well matched to the strong fluorescein absorption band (~490 nm). A phantom model developed for simulating Barrett's esophagus, including the molecular probed surface dysplasia, and would be of value for the purposes of instrument calibration and diagnostic algorithm development.

Phantoms are often constructed to simulate tissue optical and/or morphological properties for the development of imaging techniques [15]. Among these phantom designs, some were employed with multiple materials to construct stable, multi-layer tissue phantoms with essential optical properties [16] [17] [18], some were fabricated with three-dimensional structures for the purpose of quantitative optical spectroscopy [19] and for the application in photodynamic therapy [20]. Additionally, work has also been done incorporating fluorescent nanoparticles into optical phantoms to act as quantitative molecular imaging standards [21] [22]. However, little has been addressed in the field of optical phantoms for the purpose of simulating fluorescent labeling of targeted surface biomarkers in clinical endoscopy [8] [9], specifically in the field of quantitative fluorescent molecular video-endoscopy. Therefore there is a need to develop optical phantoms for both research purposes and preclinical instrumentation evaluations, which incorporate the simulation of quantifiable surface molecular biomarkers into a multi-layer three-dimensional tissue phantom.

Recent studies have demonstrated three-dimensional tissue phantoms with a quantitative subsurface fluorescence contrast agent [22], subsurface tissue autofluorescence [23], as well as phantoms with quantitative quantum dot-based molecular imaging [21] .In these studies, deep tissue optical penetration was discussed since the biomarker was buried at the subsurface level.

Here, we introduce a synthetic phantom developed to simulate topically labeled fluorescent biomarkers. Since the biomarker labeling is applied topically to the esophageal tissue [24], the surface reflectance properties are modeled to accurately mimic the disease condition, whereas synthetic tissue transparency and deep tissue optical penetration were less relevant. This phantom was designed for assisting in the validation of a new multi-spectral fluorescence endoscope for diagnosing high grade dysplasia and neoplasia (in Barrett's esophagus (BE)).

A paintable elastomeric material (latex) was selected and used to fabricate a three-dimensional model that is flexible enough to mimic the essential body movements such as opening and closing of the lower esophageal sphincter while retaining its basic cylindrical shape. Then, a color matching methodology was developed to simulate the visual appearance and diffuse spectral reflectance properties of the tissue. Paint formulations were created to match the visible color properties for a broad spectral range (400 to 700nm), and a photostable dye was selected which mimics the properties of an FDA approved fluorescent dye (fluorescein). The dye was diluted to low concentrations and cast into optically thin, rigid forms, to represent low concentration of biomarker probed disease "hot-spot" locations. The resultant phantom (**Figure 1**) is stable, repeatable, economical to fabricate, and has been successfully used to develop image based biomarker labeled quantification techniques.

2.2 Materials and Methods

2.2.1 Phantom Materials

A low-odor, brush-on latex elastomer (RL-451-80, Silpak Inc., Pomona, CA) has been chosen as the structural base of the phantom. This latex is a water-ammonia mixture and has been widely used in making theatrical masks [25]. Once shaped into a durable, hollow, cylindrical form the flexible tube mimics adult human esophagus morphology while allowing for physiological

simulations, such as the opening and closing of the lower esophageal sphincter as well as other body motions.

Healthy and Barrett's esophagus mucosa layers were simulated through combining acrylic liquid-based paint colors (Golden Artist Colors, Inc. New Berlin, NY) and a gel-based matte medium (Golden Artist Colors, Inc. New Berlin, NY). The spectral characteristics of each paint color incorporated were established by obtaining the diffuse reflectance values at different dilutions (1:1, 1:3, 1:7, and 1:10) with Titanium White (Golden Artist Colors, Inc. New Berlin, NY). After characterization, paints that displayed the correct spectral features were then combined in appropriate proportions to match the target spectrum. To account for the high viscosity of the paint, reverse pipetting was used and no volumes less than 200μL were used for the creation of the finalized paint recipes. The mixture was then applied in layers onto the inner surface of the latex cylinder by first inverting the cast latex cylinder before painting. After the paint layers were applied, fluorescent dye-in-polymer targets were placed inside the cylinder to mimic biomarker labeled fluorescent hot-spots.

The dye-in-polymer material contained a substituted 1, 8-naphthalimide fluorescent dye (Fluorol, Exciton Inc., Dayton, Ohio) that was diluted in a clear two-part polyurethane resin (AquaClear Resin, ArtMolds, Summit, NJ). The Fluorol dye is well characterized [26], soluble and stable in polymer resins and its excitation and emission spectral features are close to fluorescein, an FDA-approved dye. Fluorescein itself was not selected for this study because it lacks long-term photostability, while Fluorol has been used in dye laser research where photostability is required [27].

2.2.2 Phantom Fabrication

The template mold for the latex was a tubular plastic PVC mandrel with 2.5cm outer diameter that matches the diameter of the adult human esophagus. A simple wooden dowel fixture held the PVC tube, about 25cm long, in a vertical position during application of the latex material. The latex phantom was fabricated by applying multiple layers of latex to the PVC mandrel in order to construct a phantom with dimensions that resemble that of a typical human esophagus, approximately 25cm in length and 2.5cm in diameter. A layer of aluminum foil was placed between the PVC mandrel and the first layer of latex; this prevented the latex from adhering to the PVC mandrel and allowed easy separation of the phantom and the mandrel. The first layer was applied in a thin coat to prevent formation of air pockets as recommended by the supplier of the latex material. Hot air (~75 °C) was applied using a hair dryer for approximately 2 minutes to accelerate the drying process of the first layer. This process of applying thin coats of latex and then drying was repeated until the desired thickness was reached with about 10 accumulated layers, giving a phantom which has ~3mm wall thickness. The thickness is appropriate for allowing the model to maintain both structural integrity and flexibility.

After storage for 24 hours at room temperature, the phantom was then easily removed from the PVC mandrel due to the release property of the aluminum foil layer. The aforementioned paint-gel medium was then brushed onto the inner surface of the latex cylinder in layers, with drying of each layer accelerated using the hair dryer. In this process, the paint formulation simulating healthy esophagus tissue was applied first on the entire inner surface, then the paint layer representing Barrett's esophagus was applied. Fluorescent targets were attached with transparent adhesive tape to the painted Barrett's esophagus regions to resemble biomarker labeled high-grade dysplasia (HGD) and early stages of cancer.

To fabricate the fluorescence targets, a dye-in-polymer material was formed by first dissolving the Fluorol dye powder into Part A of the polyurethane resin. Slow stirring and low temperature heating (~45-50 °C) were used to dissolve the dye in the resin. Initially a high dye-in-resin concentration (0.01mol/L) solution was prepared and served as the master batch for further dilution into the final target concentrations in the micromole/L range. Finally the diluted Part A-dye solution was mixed with Part B at a 1:1 ratio by volume, as instructed by the polymer manufacturer. Before mixing, the Part A solution was cooled to room temperature. The dilution effect of Part B was accounted for in computing the final dye concentration in the solid polymer. Air bubbles from the mixing process were rapidly removed by using a centrifuge (Thermo Scientific Sorvall® Legend® RT) operated at 2400 RPM for 2 minutes at 2 °C. The bubble-free liquid dye-in-resin mixture was then poured into 2.5cm diameter molds. After 24 hours curing at room temperature, the rigid dye-in-polymer material was removed from the mold; the solid cylindrical castings were then sliced into thin disks using a Saw Microtome (Leica SP1600, Leica Microsystems, Nussloch, Germany). The thin (0.5 to 1.0mm) disks were then die-cut into distinctive star shapes, which were then mounted onto the inner surface of the phantom to simulate targeted biomarker hot-spots. The concentration of these simulated fluorescent hot-spots was in the range of 1 to 100μmol/L to match the *in vivo* human topical dye-peptide concentration [28].

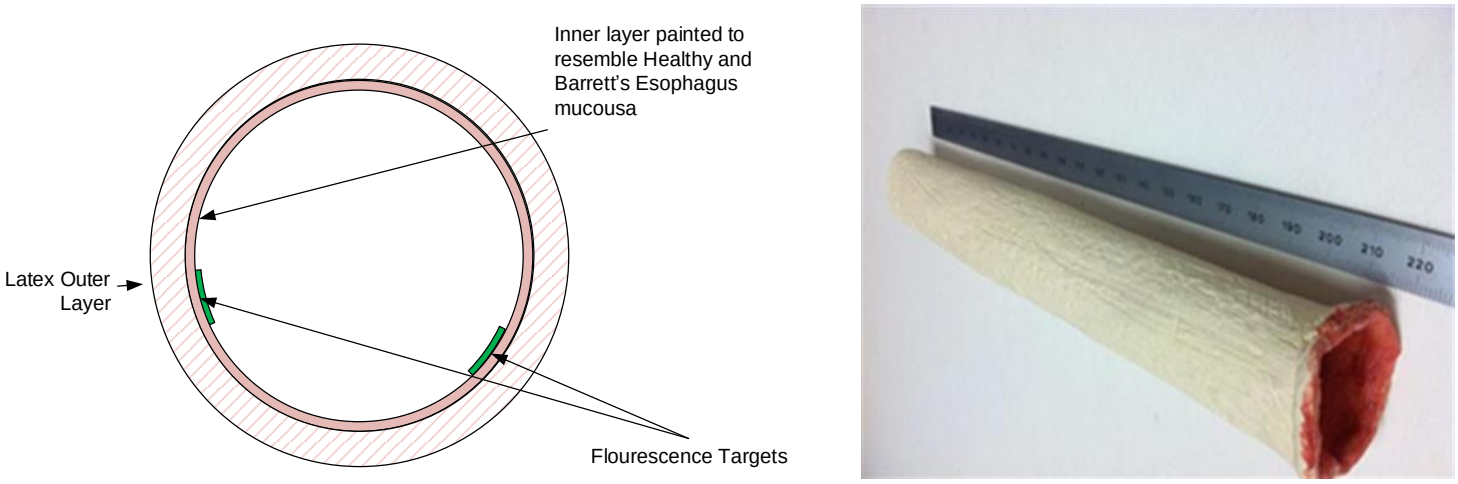

Figure 1 a A cross-sectional graph illustrating the phantom **b.** An overview of the resultant phantom design

2.2.3 Methods

The painted inner layer diffuse reflectance was measured with an Integrating Sphere (ISP-REF, Ocean Optics, Inc., Dunedin, Florida) and a spectrometer (USB2000+, Ocean Optics, Inc) [29]. A 99% diffuse reflectance Labsphere Spectralon target (SRT-99-020, North Sutton, NH) was used as the reference standard. Data were analyzed and plotted offline.

The fluorescent dye-in-polymer's capability as a quantitative standard was tested for validation. The experimental setup is shown schematically in **Figure 2**. These targets with concentration ratio of 1:2:3:4 were excited with a 444nm laser (Blue Sky Research, Milpitas, California) at a fixed distance and angle. The emission spectra were measured using the aforementioned Ocean Optics spectrometer; with a 450nm longpass filter (NT62-982, Edmund Optics Inc. Barrington, New Jersey) at the spectrometer entrance aperture to attenuate the excitation laser light [29]. The emission intensity for each fluorescent target was calculated as the area under the emission curve and then, the dye concentration vs. fluorescence intensity relationship was plotted.

2.2.4 Imaging Platform

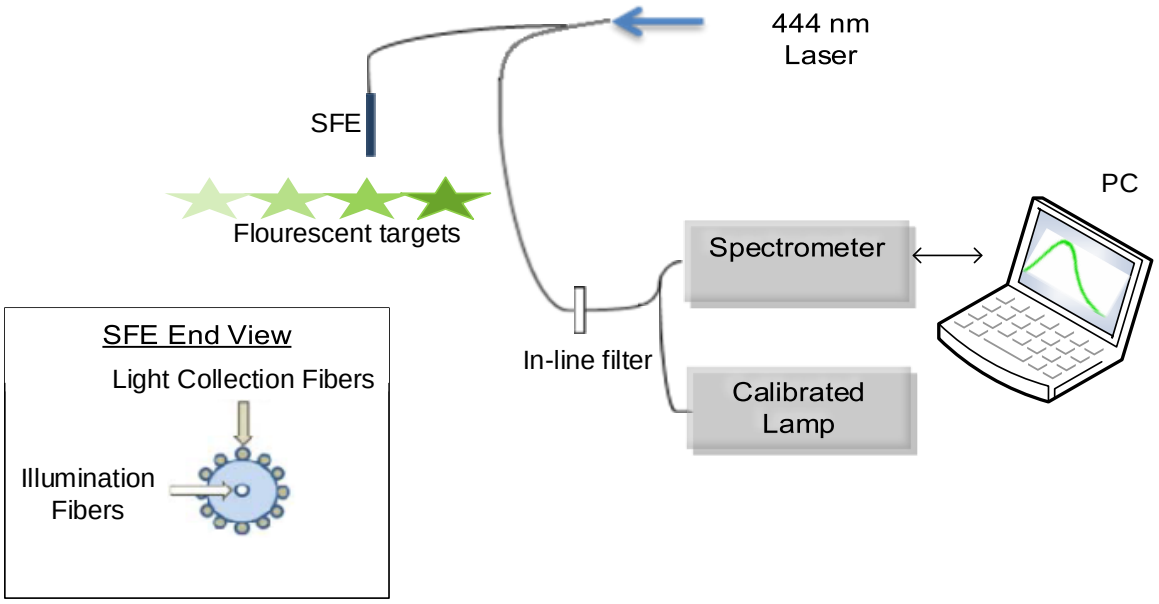

Figure 2 Schematic diagram of the experimental setup to quantify targets' fluorescence.

The SFE is an ultrathin and flexible endoscope device developed in our laboratory [30]. It provides high-quality live videos and images with wide field-of-view (up to 100-deg FOV). The SFE has been tested *in vivo* in digestive tracts (esophagus, stomach, and bile duct), as well as other parts of the body such as dental tissue and airways (pig).

In the present study, a 1.2mm diameter SFE endoscope was used. Briefly, red (635nm), green (532nm), and blue (444nm) lasers can be launched collectively or selectively at the proximal end of the SFE and transmitted to the distal end using a single mode illumination fiber. Diffuse reflected light from the target is collected by a concentric ring of optical fibers surrounding the central scanning fiber and lenses. For the 1.2mm diameter SFE, 68 high-NA (50μm diameter) multimode optical fibers were used. Details concerning the SFE imaging system are described elsewhere [30].

The ability of the SFE to perform fluorescence quantification was assessed by using the aforementioned calibrated dye-in-polymer targets. Fluorescence images of the targets excited by

a 444nm laser were taken with the SFE at a fixed angle and distance. The fluorescence intensity was calculated by selecting a target region in the resultant images and calculating an average intensity for all pixels enclosed in this target region. The dye-in-polymer concentration versus fluorescence intensity relationship was then plotted and compared to the spectrometer results to verify linearity.

White light reflectance SFE imaging of the phantom was performed and recorded. As illustrated in **Figure 3**, the standard SFE RGB reflectance imaging system uses blue (444nm), green (532nm) and red (635nm) laser illuminations and the RGB signals are then simultaneously detected and amplified by three individual photomultiplier tubes (PMTs).

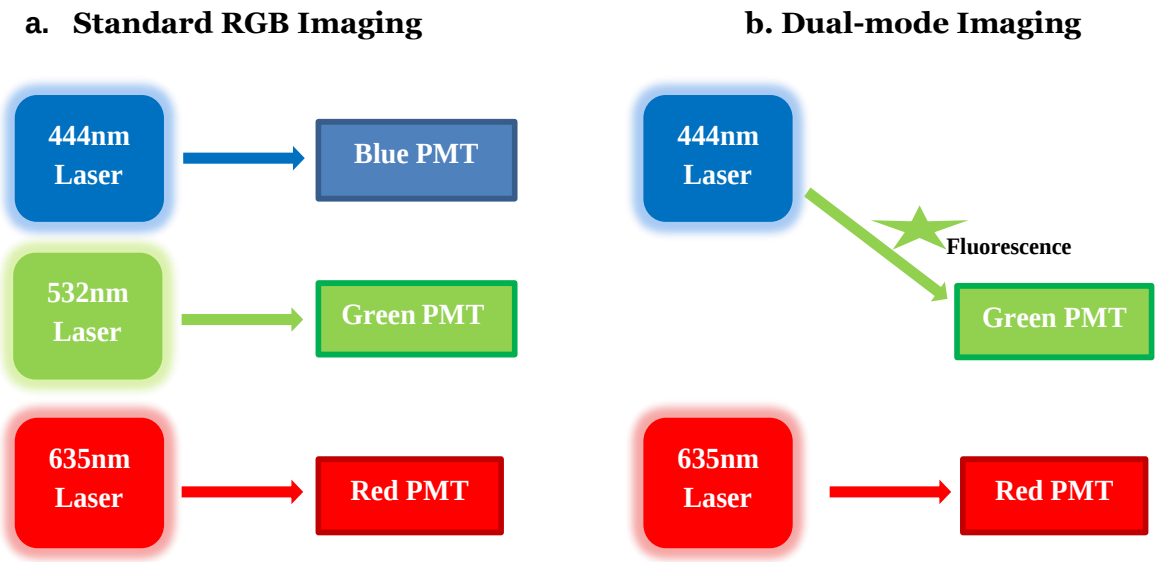

Figure 3 a. Standard SFE RGB imaging; b. SFE dual mode imaging, with the 532nm blue photomultiplier tube (PMT) channel inactive.

Concurrent dual-modal imaging was achieved by configuring the SFE such that the standard green channel was converted into the fluorescence mode by deactivating the standard green laser so that only fluorescence signals in the green spectrum were recorded. The standard red channel was used for simultaneous reflectance imaging.

2.3 Results

2.3.1 Color Matching and Diffuse Reflectance

Initially paint recipes were formulated wherein constituent paint ratios were adjusted so that the resulting diffuse reflectance values approached that of the published non-dysplastic BE [31] [32]. As the paint reflectance values approached those of the published spectrum, a disparity emerged between the formulated paint recipes and the widely reported salmon-red color appearance of Barrett's esophagus [6] [33].

Therefore, color calculations were conducted, based on the 1931 CIE spectral response functions ($\bar{x}$, $\bar{y}$, $\bar{z}$) [34], to quantify the visual appearance of the paint recipes. The color calculation methodology is shown in **Figure 4**. We found that the published spectral reflectance of non-dysplastic BE tissue corresponded to an off-white color instead of the widely recognized salmon-red BE color. Furthermore, a color calculation was also performed using the spectral reflectivity of salmon fish fillet [35]. In addition to the spectral reflectance data, the calculations included the relative spectral intensity of a xenon arc light source (Cermax® Xenon, Excelitas Technologies Corp., Fremont, CA) that is widely used in modern endoscopes [36]. The results are presented as **Figure 5** and **Table 1**.

In addition, color calculations based on the reflectance data collected from healthy oral mucosa [37] were consistent with our visual observation of oral tissue. Therefore, the salmon fillet spectra and oral spectra were selected as the representative baseline spectra for BE and healthy esophageal mucosa, respectively. Paint recipes were then optimized to match these guidelines. In addition, we solicited guidance from a panel of experienced Gastroenterologist clinicians to verify paint colors. The final paint recipes are shown in **Table 2**, all paints used are from Golden Artist Colors, Inc.

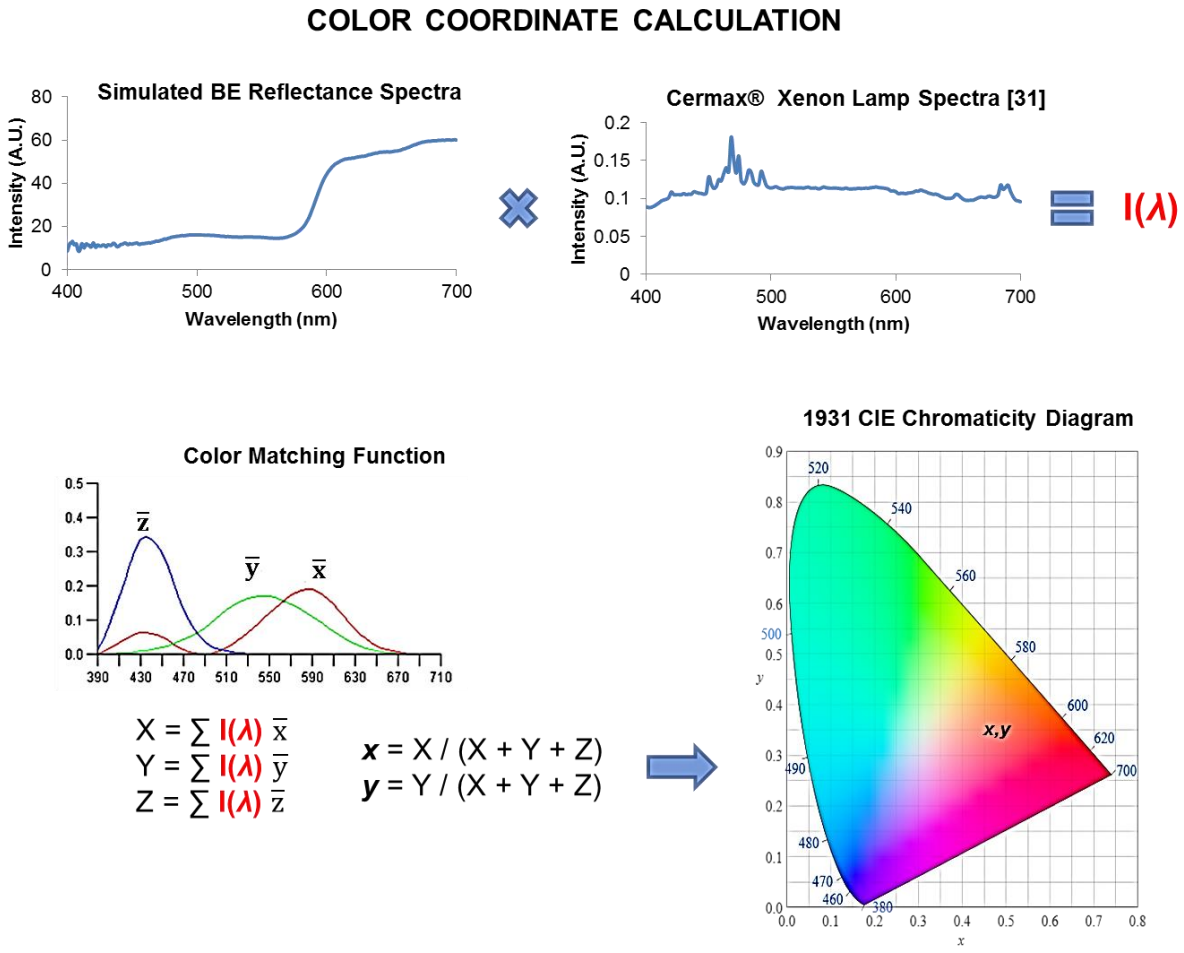

Figure 4 A summary diagram of the CIE color calculation methodology. Calculated color coordinates represent the visual appearance of a paint recipe viewed under illumination by the xenon Cermax lamp. Clinically BE is observed with an endoscope that incorporates a color CCD camera. The spectral response of modern endoscopic CCD cameras closely matches the ideal $\bar{x}$, $\bar{y}$ and $\bar{z}$ functions. Therefore, the calculated color coordinates correspond reasonably well to the clinically observed color of BE.

Table 1 Calculated Color Coordinates

Light Source	Ref. [31] BE	Phantom BE	Salmon [35]	Phantom Healthy
Cermax	0.2969,0.3286	0.4070, 0.3373	0.5089,0.3620	0.3769,0.3378

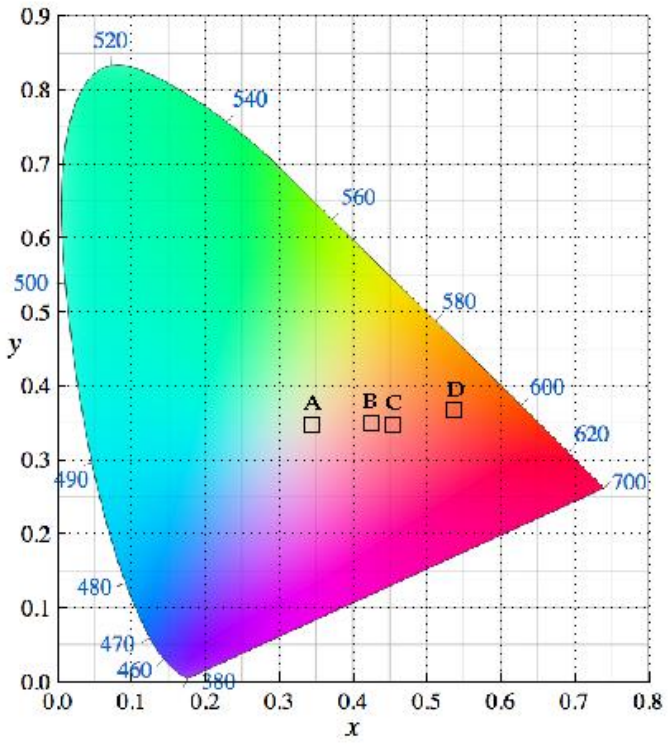

Figure 5 CIE color calculations of: A. reference [31] BE color, B. simulated healthy esophagus mucosa color, C. simulated BE color, D. Atlantic salmon fillet color [35]

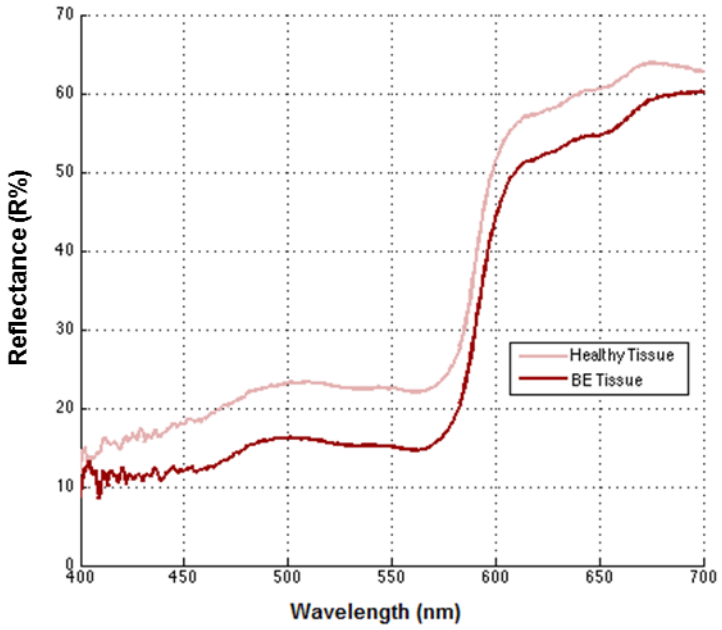

Figure 6 Diffuse spectra reflectance of simulated healthy esophagus and BE tissue from the phantom.

Table 2 Paint recipes of simulated tissue diffuse reflectance and colors

Tissue Type	Paint Ratios (by weight)
Healthy esophagus	(Pr:Qm:Hy:Pb:Gg:PgL:TW)(20:10:4:2:1:1:20)
Barrett's esophagus	(Qc:Pr:Gg:PgL:PrL)(16:6:4:3:6)

Pr= Pyrrole red

Qm = Quinacridone magenta

Hy = Hansa yellow

Pb = Phthalo blue

Gg = Green gold

PgL = Permanent green Light

TW = Titanium White

Qc = Quinacridone crimson

PrL= Pyrqrole red Light

2.3.2 Fluorol dye-in-polymer target calibration

The dye-in-polymer targets produced an emission that peaked at 500nm when excited by a 444nm SFE laser (**Figure 7**). The observed emission spectrum matched the published profile of the fluorescent dye in an acrylic plastic [26]. Targets were saw cut into 750 um thick disks and then die-cut into distinctive star shapes (**Figure 8**) with concentrations at 25, 50, 75, and 100umol/L. **Figure 9**(a) shows the fluorescence intensity as a function of dye-in-polymer concentration and **Figure 9**(b) presents the SFE fluorescence image analysis of the same dye-in-polymer targets. Both sets of data showed a similar linear behavior.

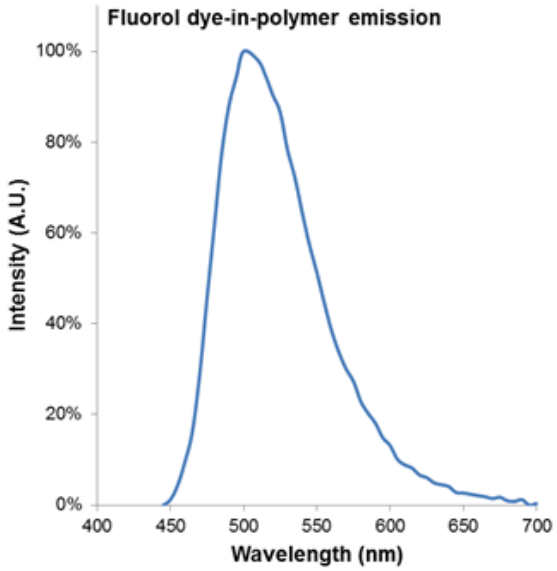

Figure 7 Fluorol dye-in-polymer emission spectra under 444nm laser excitation, measured by a calibrated spectrometer.

a. b.

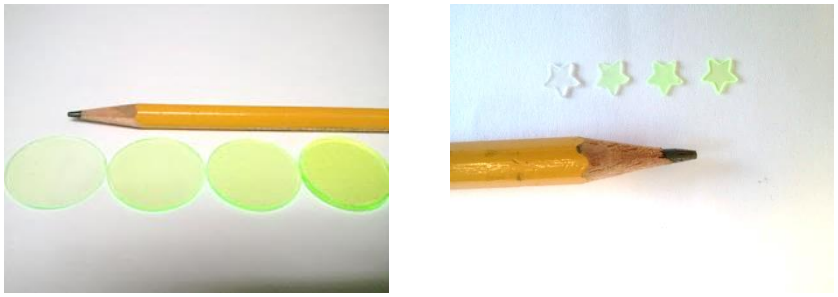

Figure 8 Photo representations of dye-in-polymer.

a. ~ 750 um thin disks, b. die-cut distinctive star shaped targets.

a. b.

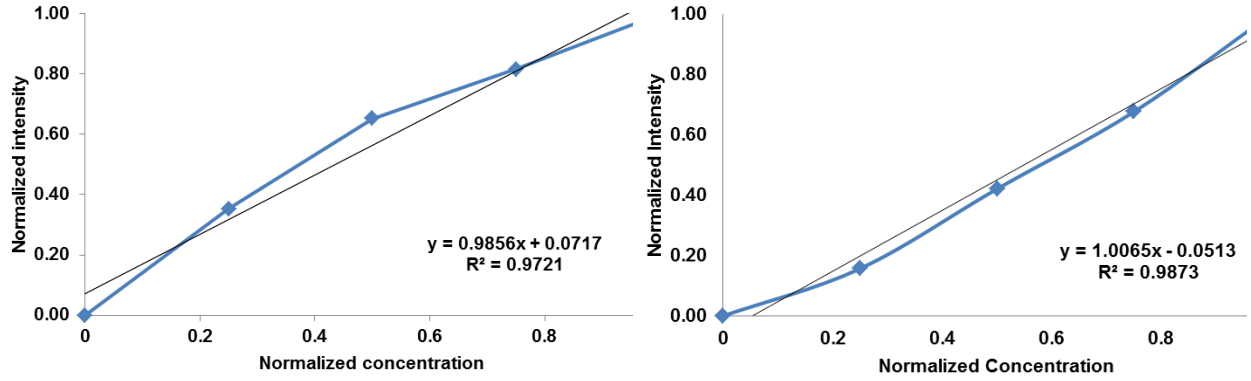

Figure 9 a. Fluorescent target emission intensity recorded with a spectrometer as a function of dye concentration b. Fluorescent target SFE image intensity as a function of dye concentration.

a. b.

Figure 10 Standard RGB SFE imaging of the phantom a. SFE images of the same phantom with with sphincter open (left) and sphincter closed (right). b. Endoscope images of a human Barrett's esophagus [36] © 2004 by Mayo Foundation for Medical Education and Research.

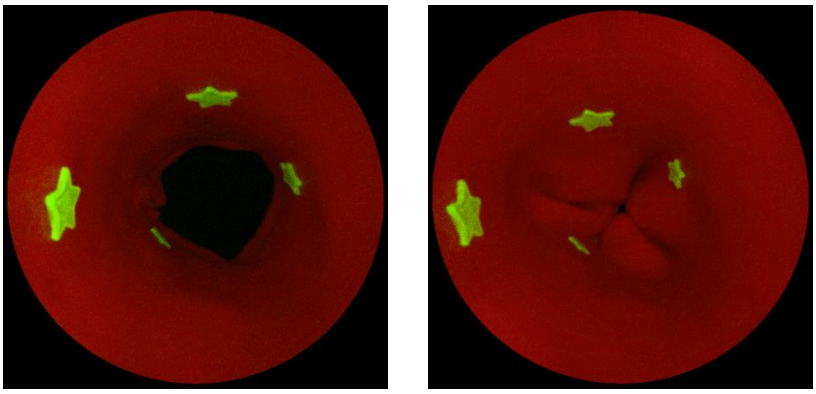

Figure 11 SFE fluorescence and red reflectance dual-modal imaging of the phantom 4 100umol/L fluorescent targets. Left: sphincter open. Right: sphincter closed

2.3.3 Phantom imaging using the SFE

The SFE probe was centered in the esophagus phantom via an in-house designed apparatus, which mimics an endoscope's working channel for transporting the SFE probe into the esophagus. White light and dual mode imaging of the lower esophagus phantom were performed with finger pressure to simulate the opening and closing of the artificial lower esophageal sphincter (**Figure 10**, **Figure 11**).

An *in vitro* SFE image-based fluorescence quantification study was conducted using the realistic esophagus phantom. Quantitative data were obtained by setting fixed gain and offset on the PMTs as well as the digital image formation process through the SFE's computer user interface. Therefore the pixel intensity of the images corresponded to the fluorescence target concentrations and distance from the SFE scope distal end.

The quantitative fluorescence imaging was achieved by using an empirically optimized non-linear ratio-metric algorithm, to compensate for the distance differences between the fluorescent targets and the endoscope due to the targets' relative orientation and separations (**Figure 12**). This

distance compensation algorithm was applied to the simultaneously acquired and thus co-registered fluorescence (F) and reflectance(R) images. A pixel-by-pixel intensity computation using a non-linear ratio of the fluorescence and red channel reflectance ($F / (R^{1.5})$) yielded excellent results.

Figure 12 Phantom application: the SFE distance compensation (DC) algorithm development

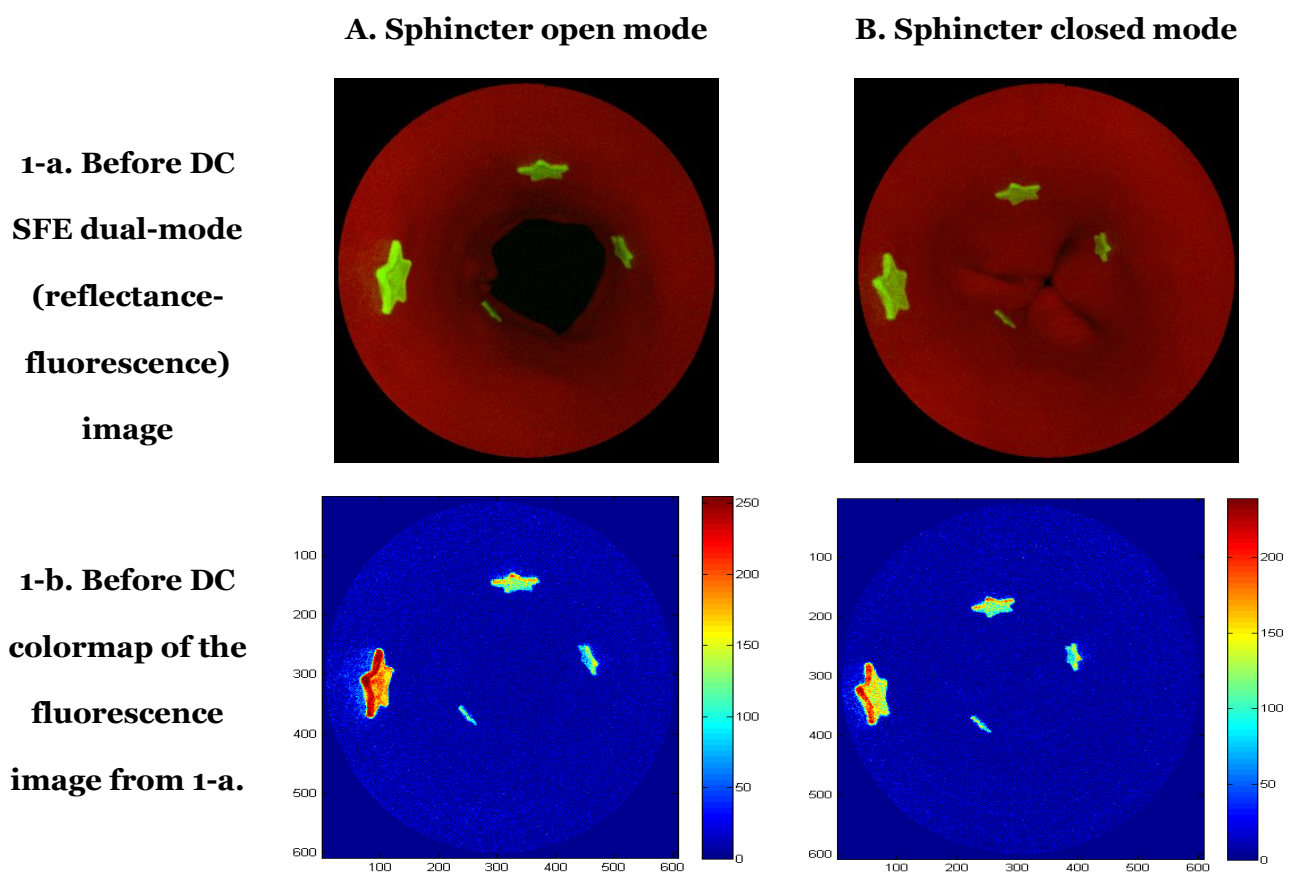

2. After DC colormap of the fluorescence image from 1-a.

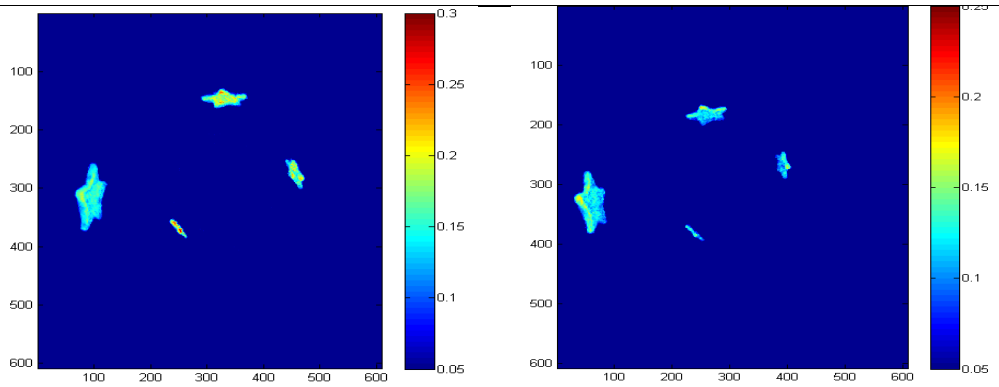

Before Distance Compensation (DC), the image intensity ratio of two targets with the same dye concentration yielded different values with average errors ~ 92% for sphincter open mode and ~39% for closed mode. However, the average error after correction was ~ 8% and ~4% respectively, resulting in a 91% error reduction for sphincter open mode and 89% for closed mode (**Table 3**). Statistical analysis (paired student-t test, one-tail, $\alpha=0.05$) compared the before and after correction image intensity errors, and result showed the algorithm significantly ($p<0.02$) increased accuracy of target quantification on both modes (**Table 3**).

A custom software user interface was also developed to allow real-time video processing and display of the color-coded map of the distance corrected fluorescence hot-spots with relative quantifications.

Table 3 Comparison of targets intensity readings before and after distance compensation (DC)

*IR = intensity ratio; *DC=distance compensation

a. Sphincter Open Mode

Location (L)	Expected IR*	before DC* IR	after DC IR	**before DC error**	**after DC error**
L1 / L2	1.000	1.685	0.858	**68.5%**	**14.2%**
L1 / L3	1.000	2.305	0.943	**130.5%**	**5.7%**
L1 / L4	1.000	3.042	0.915	**204.2%**	**8.5%**
L2 / L3	1.000	1.368	1.099	**36.8%**	**9.9%**
L2 / L4	1.000	1.806	1.066	**80.6%**	**6.6%**
L3 / L4	1.000	1.319	0.970	**31.9%**	**3.0%**
			paired student-t test (one-tail)		**p=0.013**

b. Sphincter Closed Mode

Location (L)	Expected IR*	before DC IR	after DC IR	**before DC error**	**after DC error**
L1 / L2	1.000	1.227	0.998	**22.7%**	**0.2%**
L1 / L3	1.000	1.510	1.087	**51.0%**	**8.7%**
L1 / L4	1.000	1.764	1.035	**76.4%**	**3.5%**
L2 / L3	1.000	1.231	1.089	**23.1%**	**8.9%**
L2 / L4	1.000	1.438	0.998	**43.8%**	**0.2%**
L3 / L4	1.000	1.169	0.952	**16.9%**	**4.8%**
			paired student t-test (one-tail)		**p=0.007**

2.4 Discussion

A BE phantom was constructed which matched the primary targeted geometric characteristics of the esophagus, measuring 2.5cm in width and 22cm in length. This phantom was firm enough to maintain its structure without extra support while also allowing for mechanical manipulation to simulate body motions such as lower esophageal sphincter open and closure.

White light SFE images of the phantom were recorded with a 1.2mm diameter SFE scope aligned at the center axis of the phantom looking in the direction of the simulated BE tissue. Under white light, the upper portion of the color-matched phantom presented whitish-pink normal esophagus mucosa and in the lower portion a salmon-reddish BE color. The overall appearance of the

phantom exhibited similar physical appearance compared to endoscopic images of a human Barrett's esophagus (**Figure 10** b).

The BE diffuse reflectance spectra from the phantom inner surface showed much higher orange-red reflectance compared to the blue-green reflectance. This was similar to the trend observed in the diffuse reflectance spectra feature of Atlantic salmon fillet [35]. As shown in the CIE 1931 color chromaticity diagram (**Figure 5**), the referenced Atlantic salmon fillet fell into a distinct red region whereas the previously published BE color [31] is located at an off-white region. The simulated BE color coordinates were close to the salmon-red color region. At the same time, the simulated normal esophagus color was white-pinkish. We think that the off-white color resulting from the BE reflectance spectra published in [31] was caused by pressure on the tissue by the probe contact. Recently, the effect of probe contact pressure on *in vivo* optical spectroscopy of soft liver tissue [38], oral mucosa [39], and mouse thigh muscle [40] has been studied and distortions of tissue spectra reflectance have been discussed.

In clinical video endoscopy, the perceived tissue colors, as well as disease-healthy tissue color contrast could serve as important diagnostic indicators [41] [42]. Therefore, phantoms designed with realistic tissue colors provide platforms to develop practical *in vivo* color image processing algorithms [42]. Recently real-time implementation of color enhancement algorithms for endoscopy have been reported that highlight subtle differences between cancerous and healthy tissues, and endoscopic imaging techniques using tissue color enhancement showed value assisting the detection, diagnosis and treatment of gastrointestinal diseases [43] [44]. When visualizing fluorescent targets, the realistic tissue color is important for the selection of pseudo color representations of the reflectance image to enhance contrast. Therefore, phantoms designed with realistic tissue colors could contribute to augmenting molecular imaging modalities for early cancer detection and diagnosis.

In dual mode SFE imaging, concurrent red reflectance image and fluorescent targets were readily visible (**Figure 11**, **Figure 12**). The real-time SFE concurrent fluorescence and reflectance view provides a geometric alignment that is lacking in systems with non-concurrent fluorescence/reflectance image capture. Moreover, Enhanced Spectral Imaging (ESI, also known as narrow band imaging) [41] is an enabled feature in the SFE [30] [45]. When wavelength specific spectral imaging is needed, for example in BE ablation surveillance [46] or observation of tissue vascular network, the ESI can be easily performed. One future modification of the phantom would be the addition of a simulated vascular network for the study of narrow band imaging in BE, or other common esophageal diseases such as esophageal varices.

The distance compensation algorithm was applied to both lower sphincter open and closed modes using a 1.2mm SFE endoscope. The results showed distance normalization of the perceived intensities (**Figure 12**). This compensation significantly improved the accuracy of image-based fluorescence hot-spots intensity quantification. According to the quantitative analysis in **Table 3**, after applying the distance compensation algorithm, the targets' intensity error for sphincter open and closed modes has been reduced by 91.3% and 88.8%, respectively. The red reflected light was selected because the red wavelengths are less absorbed by hemoglobin and therefore less influenced by changes in vascularity among diseased tissues. In addition, red reflected light is more uniformly scattered by the tissue morphology. Overall, red light provides a more uniform reflectance image of the target geometry than blue/green colors [47]. The robustness of this algorithm was also tested for scenarios when the endoscope is not aligned with the esophagus center axis, and results yielded consistent normalized image intensity (data not included).

The present esophagus phantom does not include autofluorescence (AF). Collagen is believed to be primarily responsible for esophageal AF [48] [6] [49] when the wavelength of the excitation

light is in the 350 to 370nm range. However, when the excitation wavelength is longer than 440nm, results from extensive searching of published collagen excitation-emission matrix (EEM) data [23] [50] [51] [52] [53] indicate that the collagen AF decreases by a factor of 3x to 5x compared to the maximum at 350-370nm excitation. Since the present phantom is intended for molecular imaging studies at wavelengths longer than 440nm, it was assumed that AF would not be a significant confounding factor. AF could be simulated if necessary by adding collagen material to the paint formulation.

In the current study, the net esophagus diffuse reflection, including surface and shallow sub-surface light scattering was simulated. Since the primary interest of this phantom is for simulation of topically applied surface fluorescent labels, deep tissue light optical penetration and scattering [48] [6] [54] were not included. A biomarker that is located on the cell surface is epithelial growth factor receptor (EGFR). However, this EGFR biomarker is overexpressed in only 35% of high-grade dysplasia (HGD) specimens in Barrett's esophagus [55]. HGD has a high probability of advancing to esophageal adenocarcinoma which in turn has a low survival rate (ten to fifteen percent) [1]. Therefore, molecular imaging devices may utilize more than one dye label to improve sensitivity and specificity [56]. The phantom model developed in this study can be adapted to include additional fluorescent dye species representing labeling of more than one biomarker. The coincident emission signature from multiple dyes is expected to provide a more accurate disease state diagnosis than a single wavelength marker [57]. This coincident emission signature from multi-spectral molecular probes could be obtained concurrently using the multi-channel photodetection feature of the scanning fiber endoscope. If the administration of multiple probes is restricted to time sequential applications, image alignment can be realized with an image stitching algorithm [58] [59] [60] .

Embedding CT/MRI fiducial markers, to allow for multi-modality imaging strategies for disease diagnostic and treatment, is another future embodiment of the phantom. For example, the co-registration of optical images with CT/MRI volumetric imaging could enable new optical-to-CT/MRI combined data for pre/post tumor resection surgery comparisons. Magnetic Microspheres (Bangs Laboratories, Inc) are stable and dispersible in the urethane resins or acrylic paints in our phantom, and can be made to contain both magnetic and fluorescent material. Properly functionalized spheres could be dispersed in urethane or acrylic paint resins and included in the phantom fabrication process to allow this bi-modal imaging.

In conclusion, we have demonstrated a new color-matched and fluorescence labeled esophagus phantom for clinical wide-field endoscopy applications. The 3D structure of the resultant phantom was semi-rigid with enough flexibility to mimic body movements. Also, through a color matching methodology, the perceived phantom tissue color and diffuse spectral reflectance were reconciled to simulate the clinically observed characteristics of typical human healthy and Barrett's esophagus. We also demonstrated a dye-in-polymer method to quantitatively simulate surface fluorescence labels. This proposed phantom provides exciting opportunities for assisting in the validation of novel endoscopic imaging systems, such as the wide-field multi-spectral fluorescence scanning fiber endoscope, as well as image-based fluorescence quantification, and other image processing algorithm developments.

3 Detecting fluorescence hot-spots using mosaic maps generated from multimodal endoscope imaging

3.1 Introduction

Within the field of medical diagnosis there has been increasing interest in molecular imaging because of its potential to target specific bio-markers at the cellular and molecular level. [4] [5] [6] [7]. In particular within the field of Gastrointestinal (GI) endoscopy, by combining fluorescence labeled molecular probes with wide-field multi-modal endoscopic devices there is significant potential to provide enhanced diagnosis and characterization of early cancer lesions by allowing for visualization of detailed biological information at the cellular or sub-cellular level. [61] [8] [62].

Currently, fluorescence peptides targeting the molecular signature of cells are under investigation for imaging of adenocarcinoma and high-grade dysplasia in Barrett's esophagus. These fluorescent peptides can be combined with a multimodal wide-field endoscopic imaging system to highlight suspect regions (also known as hot-spots) within the esophageal mucosa [8]. These hot-spots can be small and sparse and can be as small as only a few cells [5]. Additionally the detectability of the fluorescence signal is affected by both the level of background noise and distance from the fluorescence source to the endoscope.

In order to increase the effectiveness of this new technique it is important to investigate image processing algorithms and software tools, in parallel with the development of molecular probes and imaging hardware, which allows for meaningful and quantitative diagnostic information to be obtained from these small and sparse hot-spots. [11] [60] [63]. The image processing software, along with its graphical user interface, will perform analysis and visualization of the regions of interest from a combined white light reflectance and fluorescence imaging by allowing for an

augmented view of the area being scanned, through detecting and combining signals in a way that would not be possible without the automation.

In the present study, a combined image mosaicking and distance compensation algorithm is applied to endoscopic video, to enhance intraoperative visualization of these hot-spots. This proposed image processing tool has been shown to improve recognition of fluorescent regions by registering together the concurrently acquired and thus co-registered reflectance images. The resulting video mosaic can be extended to create anatomical maps of the esophagus and labeled hot-spots to assist biopsy and to serve as documentation of the procedures.

3.2 Method

3.2.1 Imaging Platform

In the current study, a 1.2mm diameter scanning fiber endoscope (SFE) was used. The SFE is an ultrathin and flexible endoscope developed in the Human Photonics Laboratory. It provides wide field-of-view (up to 100-degree) and high-quality live videos and images. This endoscope device has been tested *in vivo* in esophagus [58], bile duct [64] and stomach [58], as well as dental tissue [65], colon (mouse) [8] and airways (pig) [66]. In the operation of the SFE, red (635nm), green (532nm), and blue (444nm) laser light is launched collectively or selectively at the proximal end of the SFE and transmitted to the distal end using a single mode illumination fiber. This fiber tip is scanned in a spiral pattern at near its resonant frequency by a custom tubular piezoelectric actuator. A lens assembly provides wide field and large depth of focus of this apparent white-light illumination. Diffuse reflected and/or excited fluorescence from the target is collected by a concentric ring of optical fibers surrounding the central scanning fiber and lenses.

As illustrated in **Figure 13** a, the standard SFE reflectance imaging system uses red, green, and blue (RGB) laser illuminations. Reflected light is filtered, detected and amplified by three

individual photomultiplier tubes (PMTs). To achieve concurrent dual-mode reflectance/fluorescence imaging, the green laser was turned off so that only fluorescence signals in the green spectrum were recorded. Therefore, the standard green channel was converted into fluorescence mode. The standard blue and red channels were used for simultaneous reflectance imaging (**Figure 13** b).

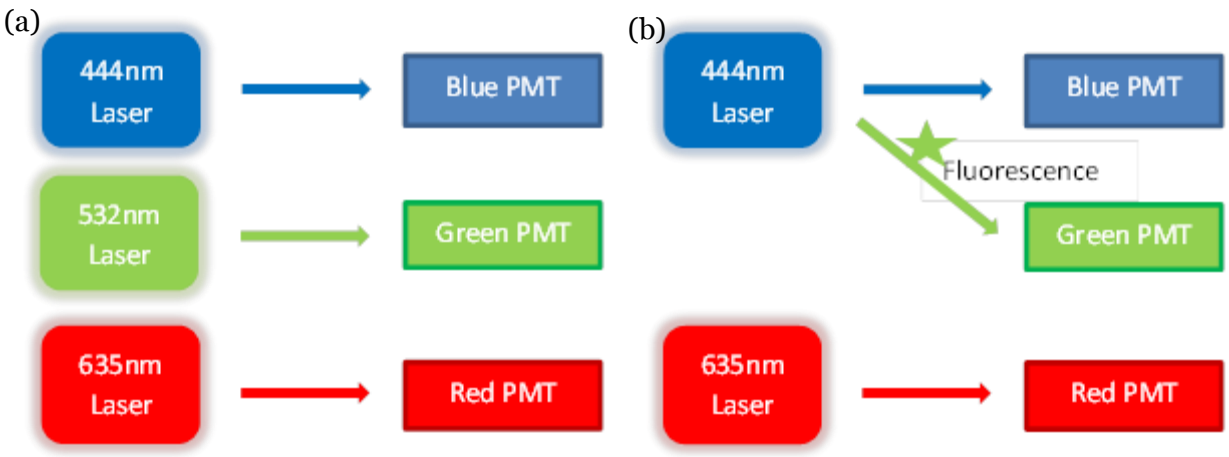

Figure 13 a. Standard SFE RGB imaging. b. SFE dual-mode imaging, with standard green laser inactive.

3.2.2 Algorithm and Software design

The mosaicking tool we developed registers successive video frames/images using optical flow. The overall algorithm is shown in **Figure 14** below.

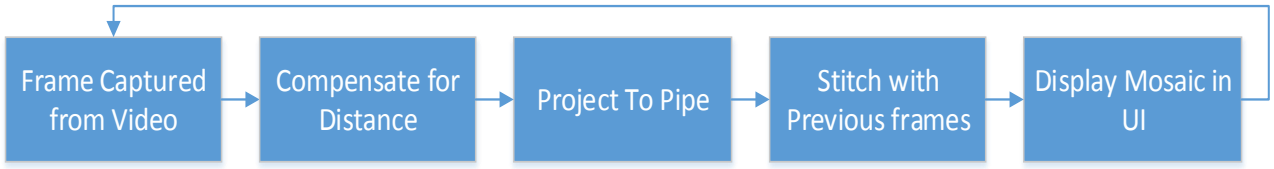

Figure 14 Software Design Flow Chart

The software operates by first capturing images or frames from the video stream, and then for each captured frame, applying a Distance Compensation algorithm. This algorithm employs an empirically optimized non-linear ratio-metric algorithm ($F / (R^{1.5})$) to compensate for the differences in relative distance and orientation between the fluorescent targets and the endoscope. Details concerning the algorithm can be found in [67].

After applying the distance compensation algorithm, we projected the image frame onto a 3D surface model. A virtual pipe or cylinder was used, as it generally represents the shape of an esophagus, and also because the surface map of a cylinder/pipe can be easily unwrapped and shown in 2D. The pipe projection is further explained in **Figure 15**, and the idea of pipe projection was adapted from previous publication [68].

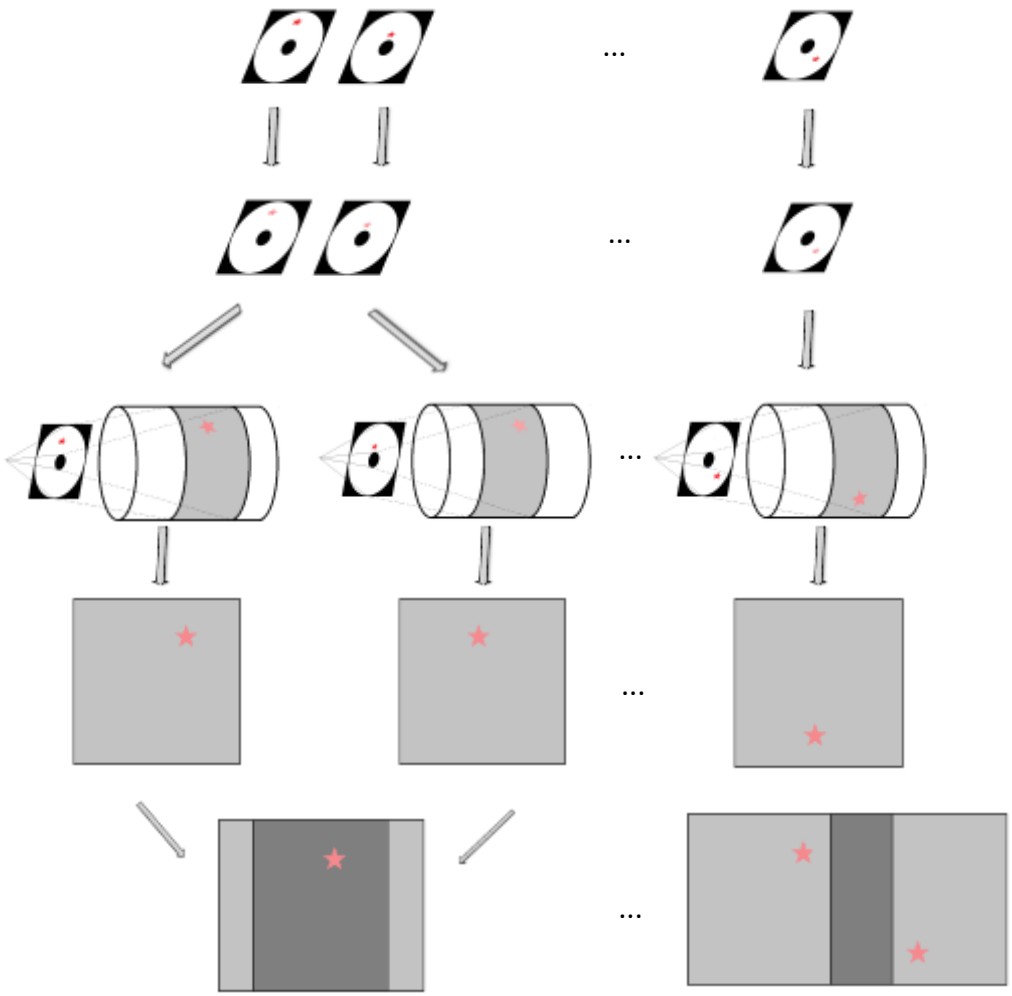

Figure 15 Pipe projection and stitching illustration. From top to bottom. Capture video frames - compensate for distance - project image onto pipe model - unwrap pipe to 2-D image - stitch together with previous frames. Final column on right shows result after multiple frames

Next the image is stitched together with previous frames. During this process, to improve the registration the algorithm leveraged a unique feature of the Scanning Fiber Endoscope (SFE) in which reflectance and fluorescence images are acquired simultaneously. First, we used successive reflectance images to calculate the required transformation between frames due to the camera

movement/motion. Next, this calculated transformation was applied to both the reflectance and fluorescence images to form a combined image with the previous frame. The software uses a combination of techniques in order to determine the best transformation to apply such as to minimize root-mean-square (RMS) error [59] [69].

To improve processing speed, an incremental, multi-resolution approach was applied during the stitching process. The original reflectance image was projected into an image that measured 700 by 1280 pixels. This was then decreased to 1/4 of its size (to 350 by 640) which lowered the resolution and decreased the time required to calculate the transformation between frames. An initial estimation of the transformation was achieved by the normalized cross-correlation method, listed below and details in [70] [71]. Then, an incremental sub-pixel alignment back on the high-resolution image was conducted using the Lucas-Kanade algorithm, listed below and details in [69] to reach the final high-accuracy registration. Finally, a dual-mode mosaic map of the esophagus was formed by stitching successive dual-mode images together based on the calculated transformation from the reflectance image.

Step1: Normalized Cross-correlation Algorithm [70] [71]
$$NCC(\mu,\nu) = \frac{\sum_i [I(x,y) - \bar{I}(\mu,\nu)]\,[T(x-\mu,)(y-\nu) - \bar{T}]}{\sqrt{\sum_i [T(x,y) - \bar{T}(\mu,\nu)]^2 \sum_i [T(x-\mu,)(y-\nu) - \bar{T}]^2}}$$
• NCC is the normalized cross-correlation • I is the image • $\bar{T}$ is the mean of the template • $\overline{T(\mu,\nu)}$ is the mean of $T(x,y)$ in the region under the template

Step 2 Sub-pixel estimates: Lucas-kanade algorithm (optical flow) [69]

$$\sum_x [I\big(W(x;p+\Delta p)\big) - T(x)]^2 \text{ [1]}$$

- the goal is to minimize the sum of squared error between the template T and image I, with a current estimate p and increment Δp:

$$p \leftarrow p + \Delta p$$

To linearize above equation [1], a first order Taylor expansion on $I\big(W(x;p+\Delta p)\big)$ is performed and resulted in:

$$\sum_x [I\big(W(x;p)\big) + \nabla I \frac{\partial W}{\partial p} \Delta p - T(x)]^2 \text{ [2]}$$

Minimizing equation [2] resulted in:

$$\Delta p = H^{-1} \sum_x [\nabla I \frac{\partial W}{\partial p}]^T [T(x) - I\big(W(x;p)\big)] \text{ [3]}$$

Where H is the Hessian matrix:

$$H = \sum_x [\nabla I \frac{\partial W}{\partial p}]^T \ [\nabla I \frac{\partial W}{\partial p}] \text{ [4]}$$

The software applies equation [3] and [4] to iteratively update the parameters p until it converges:

Iterate:

(1) Compute image I warped with W(x ; p) as $I\big(W(x;p)\big)$;

(2) Compute the error image $T(x) - I\big(W(x;p)\big)$;

(3) Compute the gradient ∇I with W(x ; p);

(4) Evaluate the Jacobian $\frac{\partial W}{\partial p}$ at (x ; p);

(5) Compute the steepest descent image $\nabla I \frac{\partial W}{\partial p}$;

(6) Compute the Hessian matrix in equation [4];

(7) Compute $\sum_x [\nabla I \frac{\partial W}{\partial p}]^T [T(x) - I\big(W(x;p)\big)]$

(8) Compute Δp based on equation [3];

(9) Update the parameters $p \leftarrow p + \Delta p$ until $||p||$ converges ($p < \epsilon$).

3.2.3 *In vitro* Barrett's Esophagus Phantom Imaging

A color-matched and fluorescence-labeled Barrett's esophagus phantom was developed in our lab for the evaluation of the stitching software [67]. This phantom was fabricated to match the structural dimension of a human esophagus. A paintable elastomeric material was selected and used for the phantom's three-dimensional shape so that it can mimic essential body movements. At the same time, realistic visual appearance and diffuse spectral reflectance properties of the tissue were simulated by a color matching methodology. A photostable dye-in-polymer technology was applied to represent biomarker probed "hot-spot" locations. The resultant phantom has been proven to be stable, repeatable, economical to fabricate, and has been successfully used in other applications such as image-based biomarker quantification [67].

In the present study, a 1.2mm SFE was centered in the esophagus phantom via an in-house designed apparatus, which mimics an endoscope's working channel for transporting the endoscope into the esophagus and maintaining its position along the centerline.

3.3 Results

3.3.1 Dual-mode SFE Imaging

The Barrett's esophagus (BE) phantom reflectance-fluorescence images were acquired from the SFE scan. Images were taken which simultaneously captured blue and red reflectance as well as green fluorescence. To represent the high-grade dysplasia and early cancer hot-spots, a total of 8 fluorescent hot-spots were distributed and attached to the lower esophagus area. Within these hot-spots, half had the same high concentration whereas the other half had the same low

concentration. Two frames acquired during the same scan were shown in **Figure 16** as examples of the SFE reflectance-fluorescence imaging. The purplish background is a combination of blue and red reflectance, while the green hot-spots were acquired from the fluorescence channel.

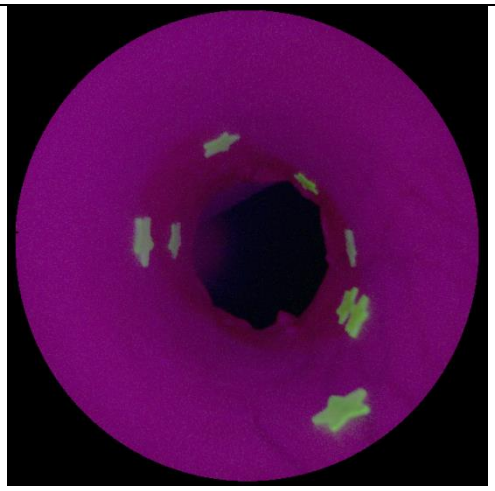

a. In the upper esophagus.

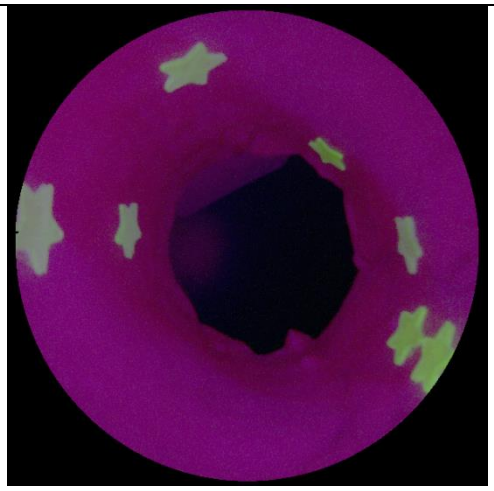

b. After being inserted several additional centimeters.

Figure 16 SFE-acquired image of our custom BE phantom

3.3.2 Mosaic of the lower esophagus

A mosaic of the BE phantom endoscopy was generated from the aforementioned stitching software. **Figure 17** shows the resultant unwrapped dual-mode image of the entire lower esophagus where Barrett's esophagus and fluorescent hot-spots were located. From the mosaic map, the painted BE area with sparse vessels appears well aligned and the distinctively shaped

fluorescent hot-spots are clearly visible. Overall, a panoramic view of the BE phantom was generated with a root-mean-square (RMS) error of 1.04.

Figure 17 The result of a mosiac map generated from the scan (~40 frames combined) shows a combined reflectance and fluorescent image of the scanned area. In this mosiac map, fluorescent targets show up as green and healthy esophagus as bright pink to the left of the map and Barrett's esophagus as darker pink to the right.

The effect of applying the quantitative fluorescence imaging – Distance Compensation (DC) algorithm is shown below (**Figure 18**), comparing the stitched mosaic with the distance compensation algorithm versus the mosaic without this distance correction. In the colormaps of the fluorescence mosaics, hot-spot intensities from the DC applied mosaic showed a clear grouping of intensities between targets of similar dye-in-polymer concentration. Whereas the

non-DC applied result showed a random pattern of hot-spots intensities that did not necessarily correlate to the dye-in-polymer concentration groupings.

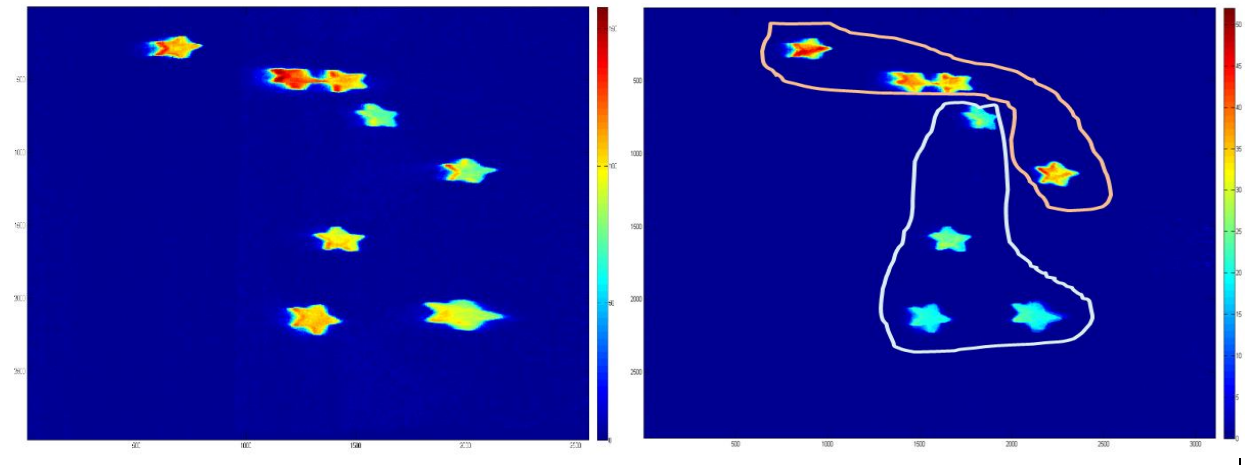

a. b.

Figure 18 Colormap representations of the fluorescence image in the resultant mosaic. **a.** Non DC applied, target intensities not match their dye-in-polymer concentrations. **b.** DC applied, target intensities match their dye-in-polymer concentrations

3.3.3 Mosaic on low signal-to-noise fluorescence

The performance of the mosaicking software was also tested on sets of reflectance-fluorescence images with low signal-to-noise (SNR). Using the same algorithm as previously discussed, registration was calculated from co-acquired high SNR reflectance images, and then applied to both reflectance and low SNR fluorescence images.

Images from the same BE phantom described above were acquired with electronic noise simulated in the fluorescence channel (See **Figure 19** left). Results comparing before and after stitching 30 successive frames of the same hot-spots area (**Figure 19** middle) showed that the stitching process reduced a great amount of background noise, and the hot-spots were

distinctively visible after scaled up targets intensities (**Figure 19** right). The root-mean-square (RMS) error (1.02) was not affected by the noise in the fluorescence channel as the algorithm only looked into the reflectance channels to solve for the registration.

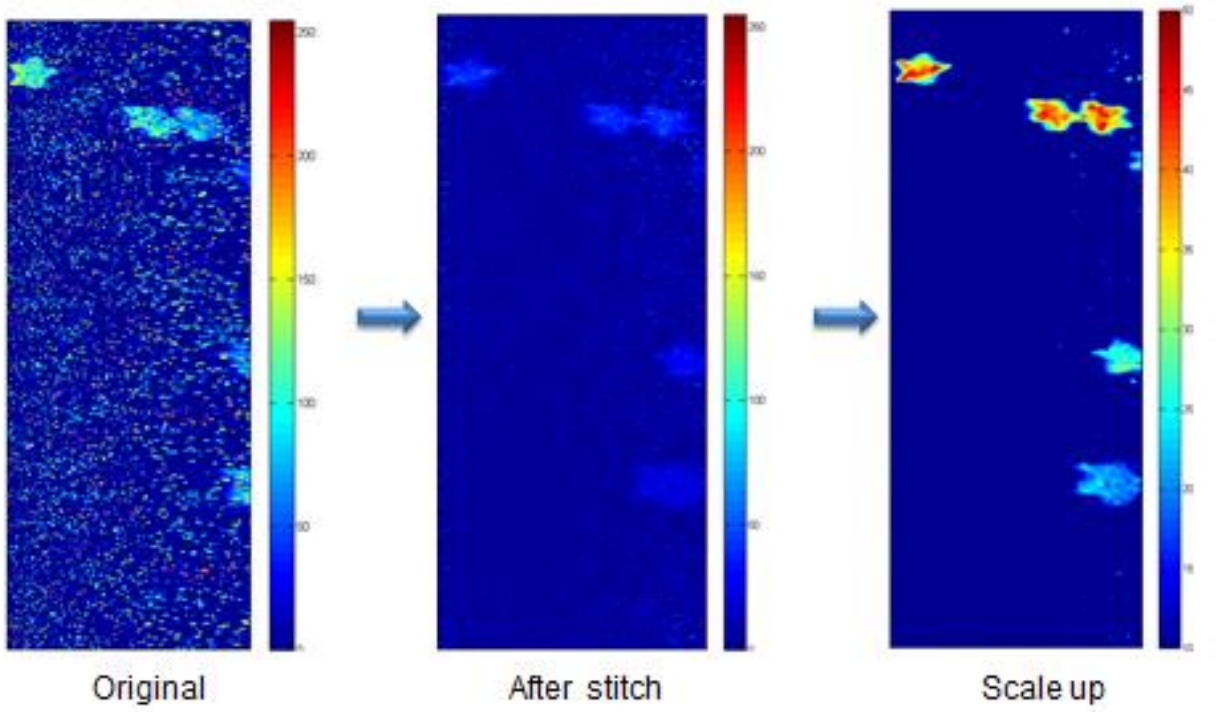

Figure 19 Electronic noise in the original fluorescence images was decreased after stitching, then targets intensities were scaled up to a hot-spots color map

Furthermore, in order to evaluate the ability of the software to enhance signals with both a high noise level and low signal intensity, the BE phantom images were also acquired which not only had background electronic noise in the fluorescence channel but also had low-intensity fluorescent targets (See **Figure 20** left). Results in **Figure 20** compared the same region of interest before and after applying the stitching algorithm. In the original fluorescence image colormap shown in **Figure 20**, the targets were barely distinguishable from the noise. However,

the stitching process averaged out the noise through successive frame overlap and averaging (**Figure 20** middle, right). It improved not only the ability for humans to distinguish these targets from the background but it also increases the applicability of various computer-aided analysis and algorithms (such as using the Weber ratio for target detection). This is despite the fact that the fluorescent channel itself did not have enough features to be successfully stitched.

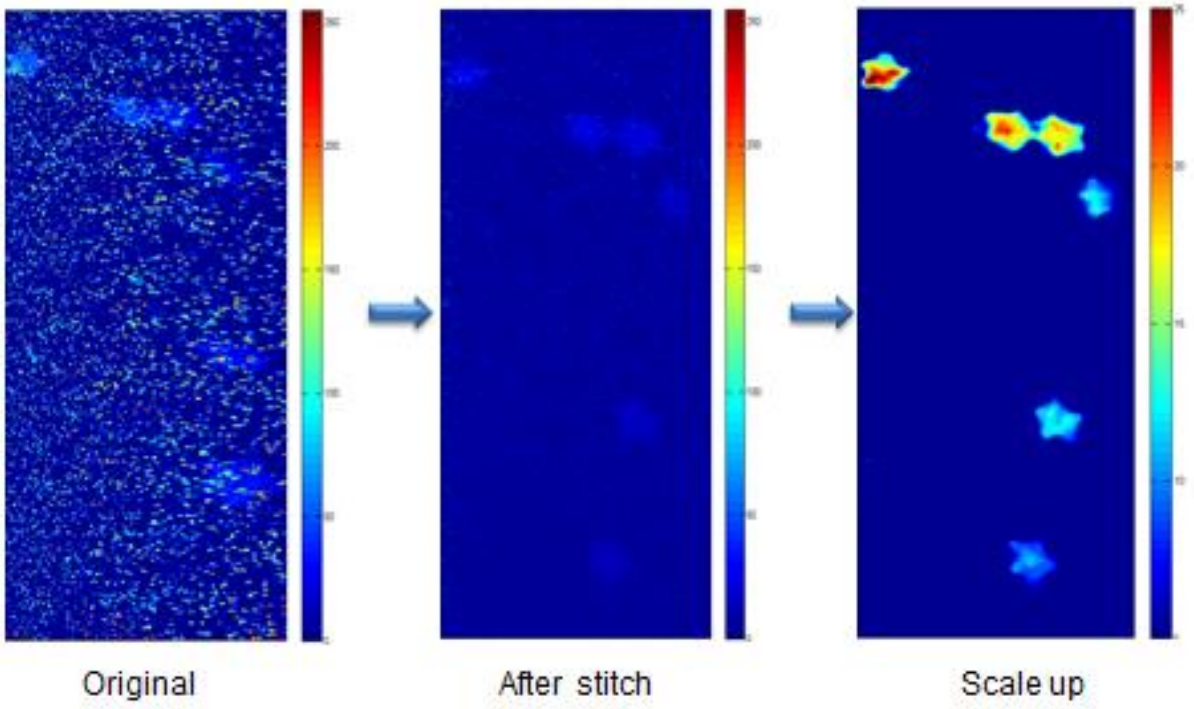

Figure 20 Electronic noise in the original fluorescence image (left) was decreased after stitching (middle), however, targets intensities were too low to be easily visible, after scaled up to a hot-spots color map (right), targets intensities were more visible

3.4 Discussion and Conclusion

The 1.2mm SFE with flexible scope demonstrated high resolution, wide field of view, concurrent reflectance and fluorescence imaging of the Barrett's esophagus phantom. In the present study, the standard red and blue SFE detection channels were used for reflectance images whereas the green channel was used for the fluorescence detection. However, additional lasers and detection channels can be added, to perform concurrent RGB white light reflectance and multi-spectral fluorescence imaging. Recently, multi-spectral fluorescence imaging using the SFE was demonstrated *in vivo*, but switching to reflectance imaging required manual switching [8]. By gathering both signals at the same time, it allows for the use of all channels of information in the analysis without having to register the spectra against each other, which can be challenging due to variations in the scene or in the scanning procedure (speed of movement etc.). Ultimately, it can lead to improved diagnostic accuracy.

The resultant mosaic encompassed a much wider view of the scene than that captured from a single endoscopic frame. The fluorescence hot-spots were visibly distinct from the background (**Figure 17**), with quantitative intensities correctly associated with the targets' concentrations (**Figure 18**b). The reflectance images were well aligned and the RMS error of 1.04 was in agreement with a good registration score.

The stitching software utilized a direct (pixel-based) alignment method [69], instead of feature based methods, to find the motion between two frames. This is because consistent features can be hard to find in the reflectance channel of esophagus, comparing to other parts of the body, such as in the bladder or colon. Meanwhile, using the concurrent reflectance images to solve for the motion is preferable to using the fluorescence channel, as that channel is prone to a low signal-to-noise ratio which significantly increases the error of the stitching. Additionally, by using a multi-resolution, incremental approach to calculating the transformations, the processing time was significantly reduced without sacrificing registration accuracy.

More importantly, the current study showed that this stitching algorithm was able to significantly enhance the fluorescent SNR, and provide targets in the stitched map with quantified fluorescence signals by effectively performing an averaging filter over the video without requiring the camera to remain stationary. The recorded mosaic can also be used for more extended review by the clinician without signal decreasing due to fluorescence photobleaching. And this mosaic map can be built into as part of the SFE's graphic user interface and possibly be used for future computer-aided diagnosis tools.

4 Mitigating Fluorescence Spectral Overlap in Wide-field Endoscopic Imaging

4.1 Introduction

It is now widely accepted that optically active fluorophores, conjugated to targeted disease probes, are effective for image-guided diagnosis and surgical procedures [72] [73] [74] [75] [76] [77] [78]. Fluorophore conjugates are routinely used to identify specific DNA components in flow cytometry systems, DNA microarrays, and in microscopic histology examinations (e.g. fluorescence in situ hybridization, FISH). Over the past two decades fluorophore optical probes have been evaluated for *in vivo* clinical imaging applications to identify pre or early stage cancerous conditions, such as neoplastic lesions in human oral tissue [79], dysplasia in colon [80], high grade dysplasia (HGD) in Barrett's Esophagus (BE) [14], as well as screening and early detection for breast cancer [81] , bladder cancer [76], and lung small cell carcinoma [82]. Meanwhile, *in vivo* molecular optical imaging has also been used in ovarian cancer surgery guidance [75], as well as for visualization and delineation of tumor margins [77] [83]. It has also been shown that optical contrast agents can aid in guiding diagnosis of difficult cancers such as ovarian cancer [84], acute leukemia and pediatric cancer [72].

Many tumors express multiple cell surface and proteomic markers. Therefore, simultaneous multi-fluorophore imaging of numerous molecular targets is important for cancer diagnosis and therapy [74] [79] [85] [86] [87] [88] [89]. Currently, multi-spectra fluorescence imaging techniques are employed in microscopic analysis *in vitro*, such as conventional immunohistology and fluorescence-assisted cell sorter. These microscopic imaging approaches are time-consuming, have a small field-of-view which means they are not applicable for *in vivo* cancer detection and localization. Therefore, multi-fluorophore molecular imaging techniques for clinical endoscopic imaging are needed.

As laser sources can help to reduce overlap in excitation, one of the remaining obstacles to full implementation of multi-fluorophore imaging is the spectral width of the emission spectra. Although quantum dot fluorophores have narrow bandwidths (FWHM ~ 25 nm), unresolved toxicity questions limit their application in human clinical studies [90]. A small number of organic fluorophores, for example fluorescein and ICG have been approved by the FDA. In addition, most organic fluorescent dyes tend to have an asymmetric spectral profile that typically extends from the peak emission to well over 100 nm in the long wavelength tail. Overlapping emission spectra are present among most common organic dyes, for example 7 - Diethylaminocoumarin - 3 - carboxylic acid (DEAC), Fluorescein isothiocyanate (FITC), Carboxytetramethylrhodamine (TAMARA) and Cyanine (Cy5.5), that have been developed for fluorescence labeling. Therefore, incorporating two or more fluorophore targeting agents may be problematic as a result of overlapping emission spectra. Confusion over the correct spectral intensities of multi-fluorophore labels could lead to misdiagnosis of overexpressed cell surface protein markers.

Although isolation filters can be used to separate the emission spectra, significant signal loss can occur. The fluorescence emission cross-talk problem is typically encountered in multi-color fluorescence microscopic imaging. In such diagnostic optical systems, sequential [91] [92] [93] [94] or synchronous [95] [96] excitation techniques can be used to separate overlapping emissions from each individual fluorophore. However, in a real time and wide-field image visualization system such as an endoscope, sequential image capture may introduce unacceptable image rendering lag times in a busy clinical work flow scenario. Therefore, we have evaluated three different options including concurrent and sequential excitation/emission image capture for distinguishing emissions from two spectrally intersecting fluorescent dye targets using a wide field scanning fiber endoscope (SFE).

The first real-time *in vivo* imaging of a multispectral target with the SFE was demonstrated with the identification of dysplastic "hot-spots" in a murine model of colorectal cancer [80]. It was also shown that topically administered fluorescent molecular probes combined with endoscopic imaging, can readily identify cancerous lesions [79] [80] [14] [97] [98]. In the diagnosis of HGD and early cancerous lesions in BE, multiple overexpressed cell surface targets, such as, epidermal growth-factor receptor (EGFR and ErbB2), hepatocyte growth factor receptor gene (MET), vascular endothelial growth factor receptor 2 (VEGFR2) have been reported [99] [100]. As a result, the coincident emission signature from multiple fluorescent-labeled probes is expected to provide a more sensitive and specific disease state diagnosis than a single molecular target for HGD and early cancer detection in BE

In a previous study, we developed a color-matched, fluorescence-labeled esophagus phantom for dual-mode fluorescence-reflectance imaging with a single fluorescent molecular probe [67]. Other applications for fluorescence molecular imaging were also demonstrated using the phantom, for example fluorescence distance compensation [67] as well as image stitching [101].

In the current study, a second fluorescent dye was added to the phantom to construct a two-dye fluorescence model that represents imaging with emission cross-talk. Three approaches: (1) image stitching, (2) concurrent imaging with Cross-talk Ratio Subtraction (CRS) algorithm, and (3) frame-sequential imaging were evaluated for the removal/reduction of fluorescence emission cross-talk in a wide-field multi-spectral fluorescence endoscopic system. For each approach, we describe the concept, outline the method of execution, and present evaluation test results. Finally, the strengths and limitations of each approach are compared and discussed. Each of the three proposed methodologies shows promise for wide-field multi-spectral fluorescence endoscopic imaging with mitigated dye emission cross-talk. Furthermore, they are also applicable to the reduction of autofluorescence and thus enhancement of target-to-background ratio during *in vivo* molecular imaging.

4.2 Materials and Methods

4.2.1 Phantom Model

4.2.1.1 Two-dye fluorescence targets fabrication and calibration

Fluorescent dye-in-polymer targets were fabricated to represent the molecular probe targeted tissue biomarker. Details of the dye-in-polymer fabrication process were described in a previous study [67]. Briefly, two dyes: chemical name Fluorol 555 (Exciton Inc., Dayton, Ohio) and Pyrromethene 597-8C9 (Exciton Inc., Dayton, Ohio) were dissolved in a clear polyurethane resin using a master-batch dilution protocol described in [67].

The Fluorol (FL) and Pyrromethene (PM) dyes were chosen as they are well characterized soluble and stable in polymer resins [102] [103] [104] [105] [106]. Moreover, their emission spectral features are close to Coumarin (DEAC), Fluorescein (FITC), 5-Carboxytetramethylrhodamine (5-TAMRA), Cyanine (Cy5.5), 5-Aminolevulinic Acid Hydrochloride (5-ALA) and Indocyanine Green (ICG) dyes, which will be used for the *in vivo* human subject studies. The FDA approved dyes were not selected for this study because they lack long-term photostability, while the currently selected FL and PM dyes have been used in dye laser research where photostability is required.

The liquid resin dye-in-polymer material was cured in a 2.5cm-diameter cylindrical mold and the solid material was then sliced into thin into disks using a Saw Microtome. The final fluorescence targets were die-cut into distinctive star shapes with an outside dimension of ~0.5cm. The molar concentration of the fluorescent targets was in the range of 1-100 μmol/L to match the molecular probe concentrations topically applied for *in vivo* human subject studies.

In the current study, 3 types of dye-in-polymer targets were fabricated: the FL-only, the PM-only, and the FL-PM mix. The FL-PM mix targets represented the spatial co-location of molecular probes at the biomarker hot-spots. The FL and PM dye-in-polymers' quantitative capability was then tested using a calibrated spectrophotometer following the same experimental setup as

previously described in [67]. A 442nm laser (Blue Sky Research, Milpitas, CA) was used as the excitation for the FL target and a 532nm laser (Blue Sky Research, Milpitas, CA) was used for the excitation of the PM target, and accordingly, a 450nm in-line long-pass filter (NT62-982, Edmund Optics Inc. Barrington, NJ) or a 532nm in-line rejection filter (NT63-346, Edmund Optics Inc., Barrington, NJ) was used individually for each excitation wavelength to attenuate excitation laser light. The fluorescence emission spectra of the two dye targets were plotted and overlaid to represent the dye cross-talk issue.

4.2.1.2 Barrett's esophagus phantom

In the current study, a color-matched Barrett's esophagus phantom was used. Design and fabrication details of this phantom were described in a previous publication [67]. The fluorescent dye-in-polymer targets were attached with transparent adhesive tape to the simulated Barrett's esophagus regions to resemble molecular probe labeled high-grade dysplasia and early cancerous hot-spots of the mucosal surface.

4.2.2 Imaging Platform

A 1.2 mm outer diameter (OD) scanning fiber endoscope (SFE) was used in the current study. The laser-based SFE technology was developed in our laboratory for the purpose of performing high-quality, wide field (FOV up to 100 degree) video imaging via an ultrathin and flexible endoscope [107]. Unlike a conventional passive imaging system that uses diffuse light illumination, the SFE incorporates low power blue (442nm), green (532nm) and red (635nm) laser illumination. The lasers can be collectively or selectively launched at the base station and sent to the distal end of the SFE scope via a single-mode optical fiber. The resulting laser beam is focused by a lens assembly, and scanned in a spiral pattern by a tube piezoelectric actuator across the field of view.

Reflected and fluorescence light are both collected by a concentric ring of high numeric aperture multimode optical fibers surrounding the central fiber scanner and lens assembly. The collected light is focused onto two dichroic beam splitters and then separated into three (Red, Green, and Blue respectively) detection channels. Prior to impinging on the photomultiplier tube (PMT) detection channel, the color separated light beam passes through a high optical density band-pass filter. The SFE system software then maps the synchronized PMT detection signals as points in the spiral scan pattern to the two dimensional pixel position of the RGB digital display. At a standard setting, the SFE outputs 500-line images at a frame rate of 30 Hz.

4.2.3 SFE imaging solutions for dye emission cross-talk

In the present study, the 442nm laser was used as excitation for the FL dye-in-polymer targets and the green detection channel was used to detect its fluorescence emission, whereas the 532nm laser was used for the excitation of the PM dye-in-polymer targets and the red detection channel was used to detect its fluorescence emission, as illustrated in **Figure 21**.

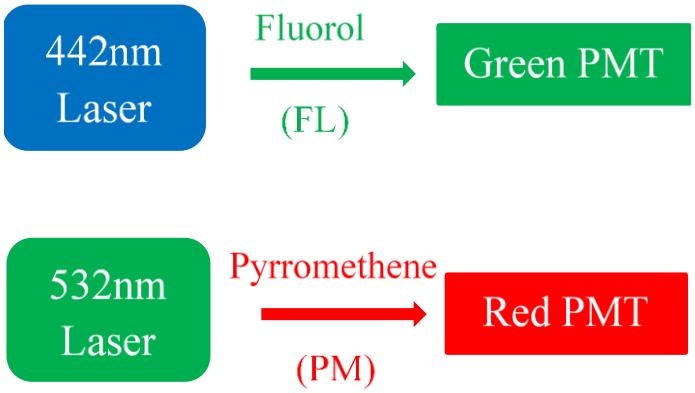

Figure 21 SFE excitation lasers and output channels for two-dye fluorescence imaging. The 442nm laser was used as excitation for the FL dye targets and the green detection channel was used to detect its fluorescence emission, whereas the 532nm laser was used for the excitation of the PM dye targets and the red detection channel was used to detect its fluorescence emission.

The SFE's ability to perform quantitative fluorescence imaging was tested and verified previously [29]. For quantitative two dye imaging, the automatic gain control in the SFE system was turned off. The gain and offset on the PMTs as well as the electronic digital display were also calibrated and maintained at a constant value. SFE images and video frames were captured and saved through the system software and analyzed off-line. In the current study, a color-matched Barrett's esophagus phantom was used. Three types of aforementioned fluorescence targets: FL dye only, PM dye only, and FL-PM mix were all placed in the phantom mucosal surface for the dual-fluorescence imaging.

To mitigate the fluorescence dye emission cross-talk, three approaches were implemented and evaluated:

4.2.3.1 Merging multispectral fluorescence scans using image stitching

4.2.3.1.1 Key concept:

In separate image capture scans, alternating once between excitation lasers, a continuous series of images were captured as the SFE scope was moved along the central axis of the phantom. All the fluorescent targets were distributed on the phantom surface but only a single fluorescent specie was excited in each scan. An image stitching algorithm [101] was applied to 40 to 50 video frames of each scan and generated a two dimensional (2D) anatomical map containing the fluorescent hot-spots. Finally, these individual 2D maps were spatially registered and combined using shared anatomical features. This wavelength separated image collection approach has minimal dye emission cross-talk, as the dyes are excited at separate wavelengths.

4.2.3.1.2 SFE dual-fluorescence imaging

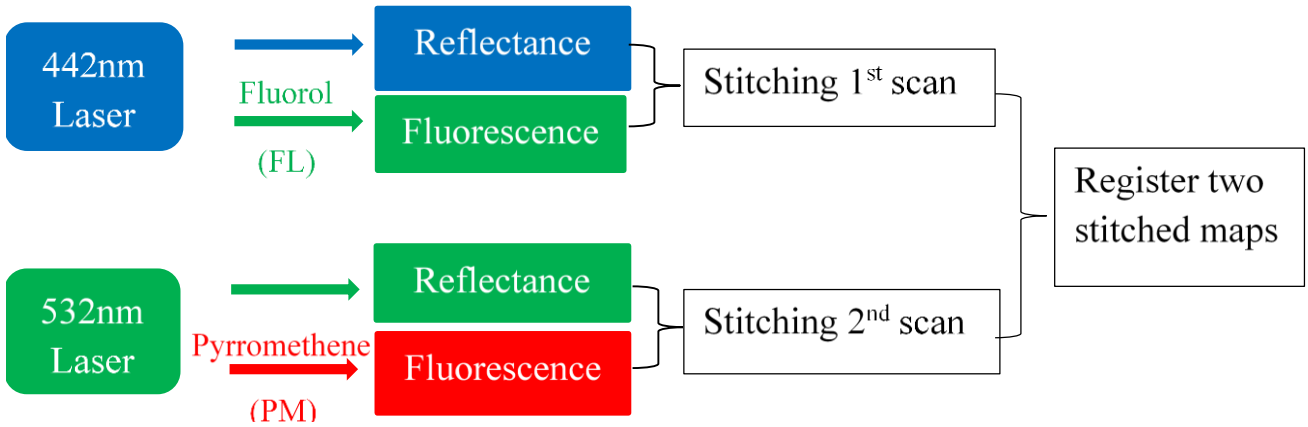

Figure 22 Flowchart for the concept of two-dye imaging using image stitching. In the 1st scan, concurrent FL target fluorescence and reflectance images were recorded, and then imported into the image stitching software to generate a 2D FL dye fluorescence hot-spot map was then generated. The software then spatially registered and merged the individual FL and PM map into a combined map with FL-only, PM-only and FL-PM mix targets

A simplified flowchart containing the key steps of the image stitching approach is shown in **Figure 22**. At first, FL target fluorescence and reflectance images were recorded. To concurrently obtain the fluorescence and reflectance images, the 442 nm laser was turned on as illumination source and the 532 nm and 635 nm lasers were disabled. The reflectance image was captured in the blue channel and the fluorescence was captured in the green channel.

Once the first scan was finished, the recorded images were imported into the image stitching software to generate a 2D unwrapped map of the lower esophagus with FL fluorescence hot-spots. The 2nd scan for the PM target followed the same procedure, except that in this case, the 532 laser was turned on as illumination source whereas the other two lasers were disabled. The reflectance image of the lower esophagus phantom and the targets were captured in the green channel and the PM fluorescence was captured in the red channel. A 2D unwrapped map of the lower esophagus with PM fluorescence hotspots was then generated. The 2D FL and PM fluorescence stitched maps were then spatially registered and merged into a map showing all three types of fluorescence targets: PM, FL and PM-FL mix.

4.2.3.1.3 Image stitching algorithm and software design

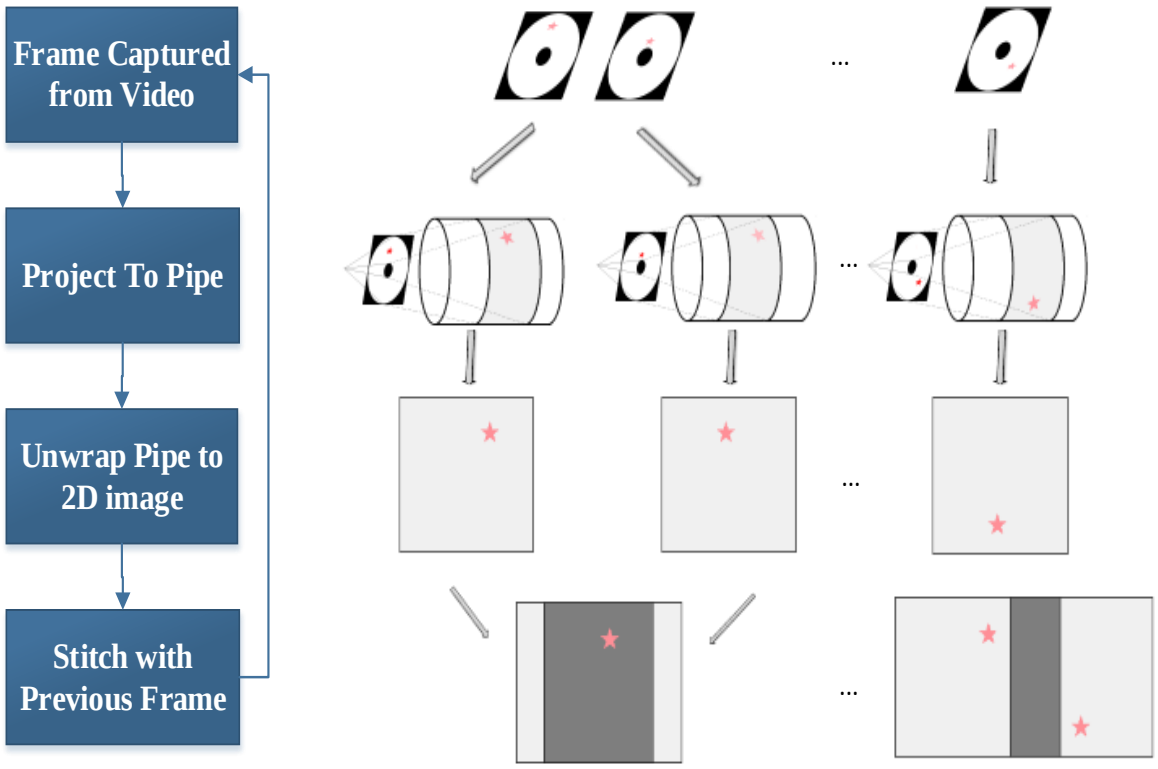

Figure 23 Left: A flowchart shows the pipeline of image stitching software. **Right:** Graphical illustration of the pipeline.

As described in the previous section, Image stitching is used to combine multiple frames from the endoscopic scan into a single 2-D map. This section will further describe the approach and process involved.

As illustrated in **Figure 23**, the software operates by first capturing images or frames from the video stream, and then the endoscopy image frame is projected onto a 3D surface model. A virtual pipe/cylinder surface model is used as it represents the general shape of an esophagus [68] [58].

After the pipe projection, the texturized surface map of the cylinder is unwrapped and shown in 2D. Next, the 2D unwrapped individual frame is stitched together with the previous frame. This process is achieved by leveraging the SFE's unique feature where reflectance and fluorescence images are acquired simultaneously. Reflectance images are used to calculate the required transformation between frames due to the camera motion. For this step, a normalized cross-correlation method is first applied to calculate the initial transformation and align the frames together at pixel level, then, optical flow (Lucase-Kanade) algorithm is used to reach a higher-accuracy image alignment at a sub-pixel level [59] [108] [69]. The calculated transformation is then applied to both current reflectance and fluorescence images to form a combined image with the previous frame. By stitching successive frames together, a dual-mode reflectance-fluorescence 2D mosaic map of the lower esophagus is then formed. The 2D mosaic map for individual fluorescence scan can then be registered together to form a final composite mosaic map with multi-spectral fluorescence hot-spots. The mosaicking software was originally created to assist biopsies and document findings during fluorescence endoscopy for HDG and early cancerous lesions in BE. This approach was also demonstrated enhanced signal-to-noise ratio (SNR) fluorescence imaging by using co-acquired high SNR reflectance imaging [101].

4.2.3.2 Concurrent multispectral fluorescence imaging

4.2.3.2.1 Key concept

In this approach all fluorescent species are illuminated concurrently with both lasers and have their emissions collected simultaneously. The dye emission cross-talk is mitigated by applying a FL Cross-talk Ratio Subtraction (CRS) algorithm:

CRS Algorithm*

$$Eq.(1) \qquad CR\_dye\_I = \frac{FL\_dye\_I\ in\ R}{FL\_dye\_I\ in\ G}$$

$$Eq.(2) \qquad Corrected\ R_I = Measured\ R_I - Measured\ G_I \times CR$$

** **CR**=Cross-talk Ratio; **R** = red detection channel; **G**= green detection channel; **I** = intensity*

At the step 1, a constant: FL dye Cross-talk Ratio (CR) is calculated from Equation (Eq.) 1 by experimentally imaging FL dye targets alone at various intensities and distances in the phantom. At step 2, concurrent laser wavelength excitation is enabled. The FL dye cross-talk signal (calculated as Measured G_I * CR in Eq. 2) is subtracted from the red detection channel, and the corrected PM dye red signal intensity is therefore obtained.

4.2.3.2.2 Concurrent SFE dual-fluorescence imaging

A series of SFE calibration experiments were performed with the dye-in-polymer materials. First, a test was carried out to verify that the laser excitation wavelengths exclusively excited one of the two dye targets, for example, 442 nm laser alone does not cause PM fluorescence emission, and the 532 nm laser alone does not cause FL fluorescence emission. Next, the linearity of the fluorescence detection channels (G and R) was tested by plotting the fluorescence images' pixel intensity versus the dye molar concentration of the targets as previously described [67]. Then, the aforementioned Cross-talk Ratio (CR) was calculated from images with 442 nm excitation only. The fluorescence intensity was obtained by selecting a target region in the resultant images and calculating an average intensity for all pixels enclosed in this target region. Also, the consistency

of the CR was tested by plotting it against the distance of the SFE to the fluorescence targets. This CR is then applied to the concurrent red detection channel based on Eq. 1, to subtract out the FL dye emission cross-talk. Concurrent images and videos are then acquired.

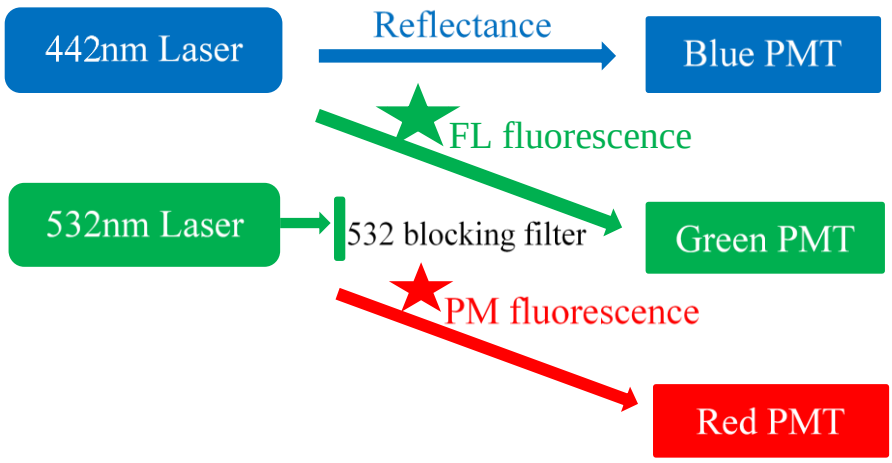

Figure 24 Dual-mode fluorescence-reflectance two-fluorophore imaging. The 632 nm laser is powered off. A band pass optical filter was positioned in front of the green detection PMT to block stray light from the 532 nm laser, selectively transmitting the FL dye fluorescence. Therefore, the green and red detection channels are configured for fluorescence imaging whereas the blue detection channel is for reflectance imaging.

The SFE setup is illustrated in **Figure 24**. The 442 nm and 532 nm lasers were turned on for the simultaneous illumination of FL and PM fluorescence targets respectively. The green detection channel was used to receive the FL emission signal whereas the red detection channel was for the PM emission. A short wave pass filter (SP01-532RU, Semrock, Rochester, NY) was used in the green detection channel to block the 532 nm excitation laser.

4.2.3.3 Sequential multispectral fluorescence imaging

4.2.3.3.1 Key concept

This method addresses the dye emission cross-talk problem through excitation and collection of one fluorescence species at a time. However, instead of using image stitching to post-process and composite the multiple fluorescence target images, this sequential imaging approach works by sequentially activating the excitation lasers in an interleaved pulsed mode as illustrated in **Figure 25** As a result, the fluorescence signals are individually acquired in an interleaved mode and then composed at near real time.

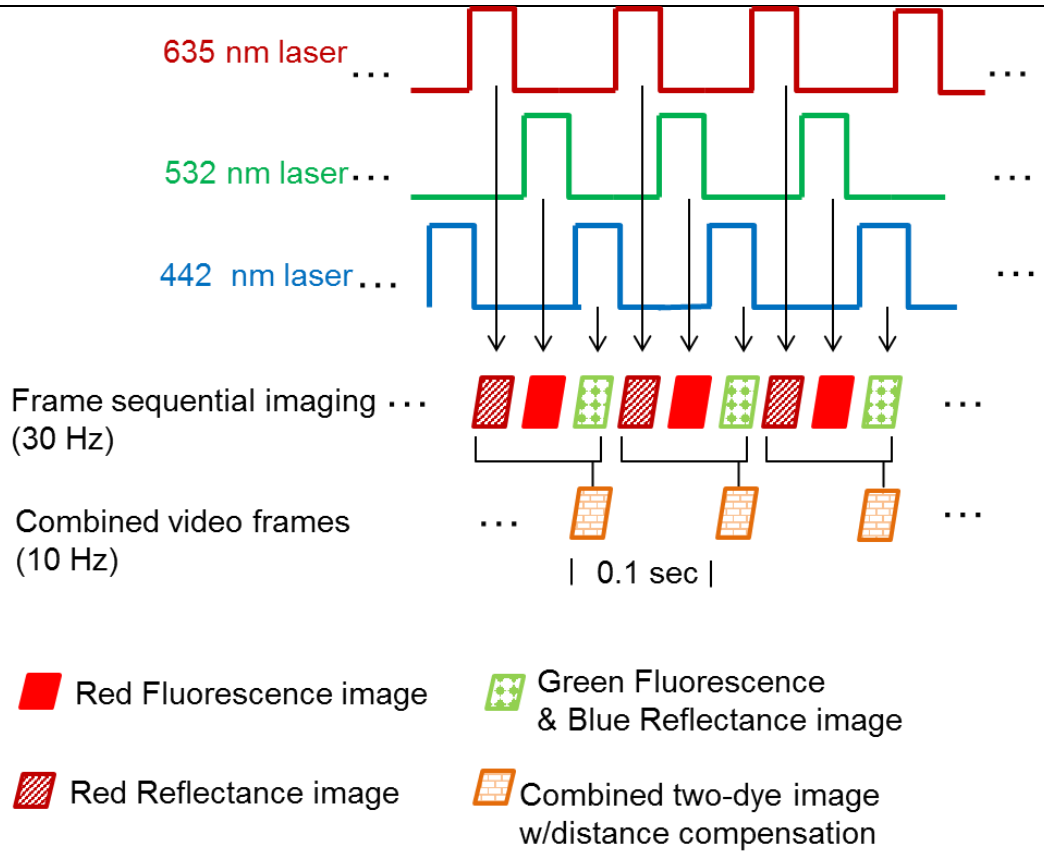

Figure 25 Graphic illustration of the frame sequential multispectral fluorescence imaging technique. Each of the red, green and blue lasers was turned on individually and sequentially. Meanwhile, red reflectance, PM red fluorescence, and FL green fluorescence were received in the detection channels sequentially at 10 (30/3) Hz. The red reflectance frames were acquired to enable the Distance Compensation (DC) algorithm for quantitative fluorescence imaging. When the DC algorithm is not needed for the application, only PM red and FL green fluorescence are acquired at 15 (30/2) Hz. In normal operation, red, green and blue reflectance are used for conventional "white light" color imaging

4.2.3.3.2 SFE dual-fluorescence imaging

A new SFE system feature was implemented to enable the excitation lasers to be sequentially modulated. A new SFE system feature was implemented to enable the excitation lasers to be sequentially activated, so that the red, green and blue lasers were turned on one at a time. In the detection channels, red reflectance, PM red fluorescence, and FL green fluorescence were received sequentially at 30 Hz (10 Hz for each). The red reflectance images were acquired to enable the application of the Distance Compensation algorithm [67]. This algorithms uses an empirically optimized non-linear ratiometric method to compensate for the difference in relative distance and orientation between the fluorescence targets and the distal end of the SFE probe. The composite rendering was formed from sequential red fluorescence, green fluorescence and blue reflectance images merged together into full RGB images.

4.3 Results

4.3.1 Characterization of fluorescence dye emission cross-talk

The FL dye-in-polymer targets produced an emission that peaked at 500nm under 442nm laser excitation and the PM dye-in-polymer targets produced an emission that peaked at 550nm under 532nm laser excitation (**Figure 26**). The observed emission spectra closely matched the published fluorescent dye profile [103] [104] [105] [106]. **Figure 26** shows that the emission spectra of the two dyes exhibits cross-talk, specifically, the long wavelength tail portion of the FL dye emission spectrum overlaps the PM dye emission from (~540nm) – (~700nm). The band pass ranges of the SFE green and red channels, which are situated at 500-540nm and 570-640nm respectively, are also plotted and are highlighted as solid green and red colors in **Figure 26**.

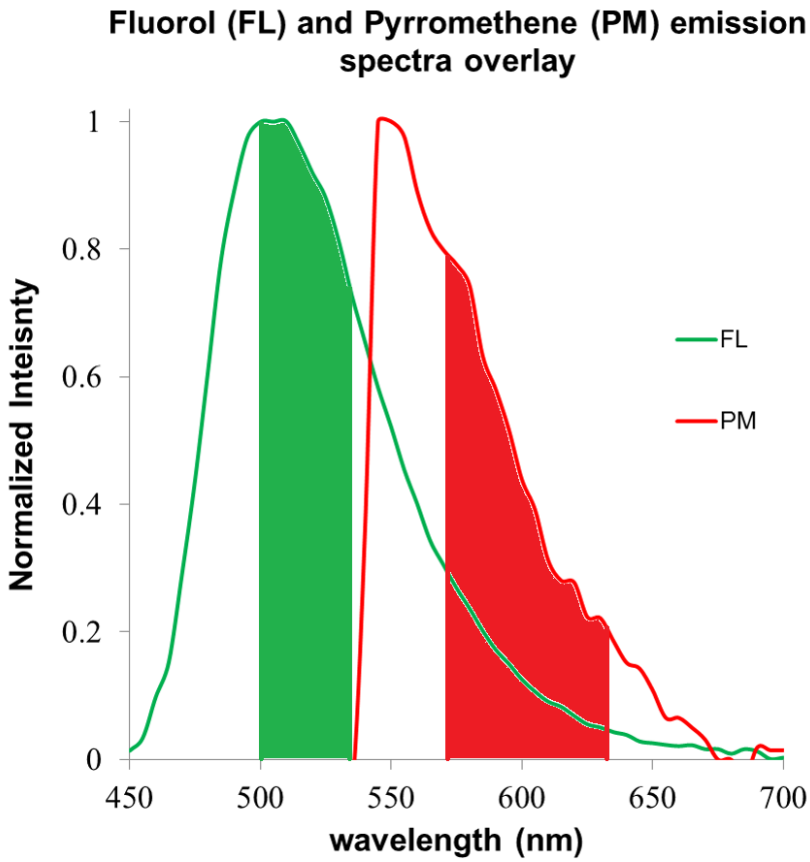

Figure 26 FL and PM dye-in-polymer fluorescence emission spectra superimposed over the SFE green and red channel detection ranges. The FL targets were excited with the 442nm laser and produced an emission (shown in green) that peaked at 500nm. The PM targets were excited with the 532nm laser and produced an emission (shown in red) that peaked at 550nm. The band pass ranges of the SFE green (500-540nm) and red (570-640nm) channels are also plotted and highlighted as solid green and red colors. The emission spectra of the two dyes exhibits cross-talk, specifically, the long wavelength tail portion of the FL dye emission spectrum overlaps the PM dye emission from (~540nm) – (~700nm).

4.3.2 SFE imaging solutions for dye emission cross-talk

4.3.2.1 Merging two-dye fluorescence hot-spots using image stitching

Two sets of SFE dual-mode reflectance-fluorescence images were collected as described in **Figure 22**. The first image consists of the FL dye target emission, the second consists of the PM dye emission. All the other experimental factors (laser power, gain and offset, etc.) were held constant during the image acquisition. The stitched and unwrapped 2D map for the FL imaging (**Figure 27** (a)) comprised the blue reflectance images shown as the background with the FL green fluorescent hot-spots. Meanwhile, the 2D stitched map for the PM imaging (**Figure 27** (b)) comprised the green reflectance image of the same background scene as in **Figure 27** (a), with the PM red fluorescent hot-spots. The red fluorescence appeared as an orange color in **Figure 27** (b). This was due to the overlap of the red PM targets' color with the green background reflectance.

The two separate stitched 2D maps were then combined and spatially registered using shared information from the blue and green reflectance channels. In the combined stitched map shown in **Figure 27** (c), only the FL fluorescence is shown in the green display channel and the PM fluorescence in the red display channel. The FL-PM two-dye targets are shown as orange. No dye cross-talk was observed.

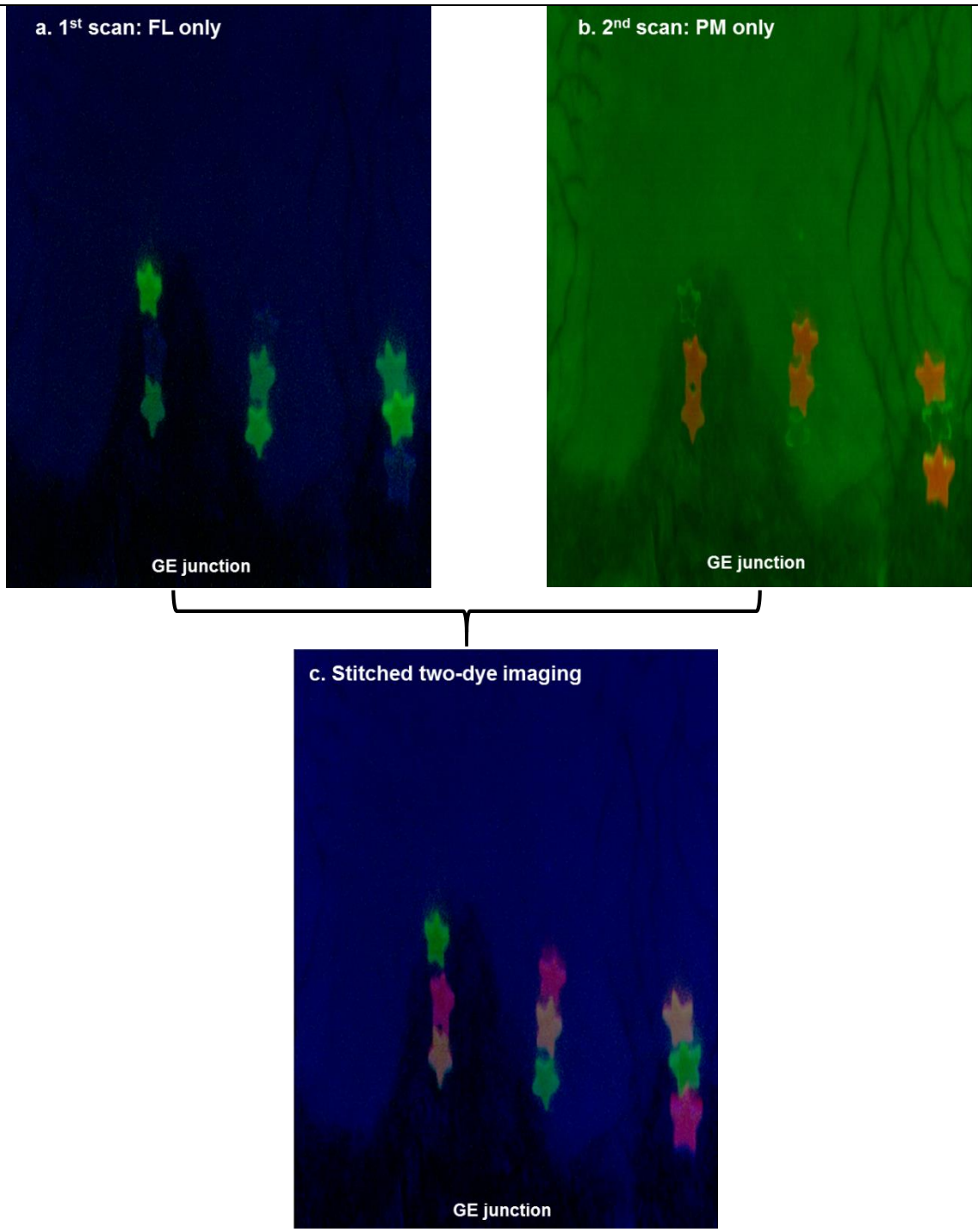

Figure 27 (a) The stitched and unwrapped 2D map for the FL imaging. It comprised the blue reflectance images shown as the background with the FL green fluorescent hot-spots. **(b)** The 2D

stitched map for the PM imaging. It is comprised of the green reflectance image in the background, with the PM red fluorescent hot-spots. **(c)** The combined stitched map shown. Only the FL fluorescence is shown in the green display channel and the PM fluorescence in the red display channel. The FL-PM two-dye targets are shown as orange

4.3.2.2 Concurrent multispectral fluorescence imaging

Experiments were conducted to verify that the 442nm laser exclusively excites FL emission while the 532nm laser exclusively excites PM emission. The results were in agreement with the previous publications on FL and PM dye absorption profiles [102] [103] [105] [106]. Therefore, cross-talk between the green and red SFE detection channels arises only from the overlapping fluorescence from the two dyes as illustrated in **Figure 26**. For the micromolar dye concentrations used in this study, dye-to-dye energy transfer was not observed.

A linearity test of the fluorescence output channels was conducted and the results are plotted in **Figure 28** (a), (b). The response of the SFE green and red detection channels were measured by imaging FL and PM targets containing precise dye concentrations. Linear relationships were measured for the dye-in-polymer concentrations as shown in **Figure 28**.

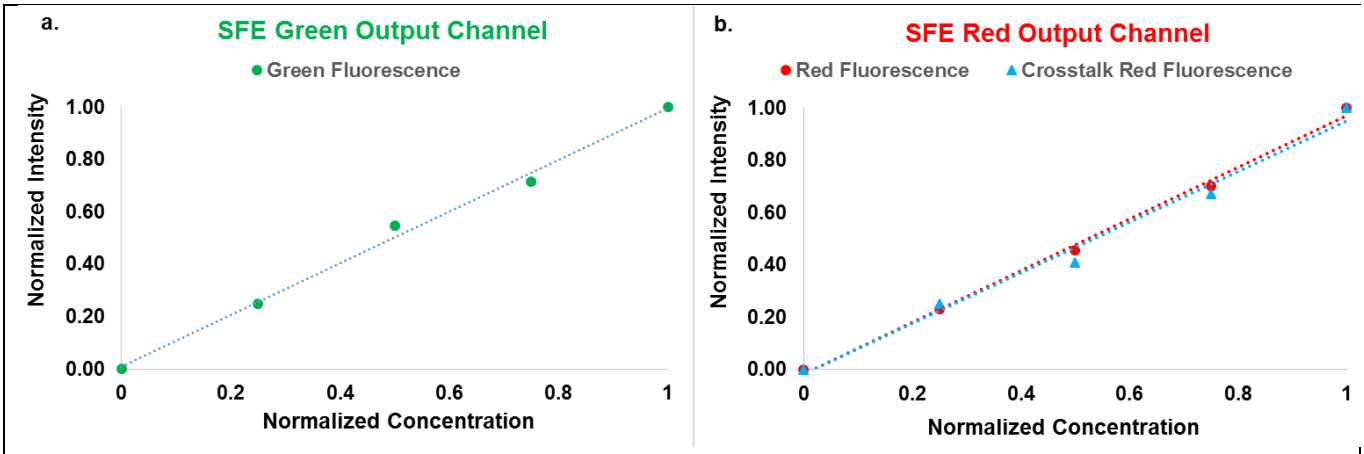

Figure 28 Fluorescence dye-in-polymer concentrations were plotted against the detected fluorescence signals in the SFE images. Specifically, (a) shows the dependence for the SFE green detection channel and (b) shows the dependence for the SFE red detection channel. The data shows that a linear relationship exists for both (a) and (b) cases.

By applying the Cross-talk Ratio Subtraction (CRS) algorithm presented in Eq. 1 and 2, the FL dye Cross-talk Ratio (CR) was calculated and concurrent SFE dual-fluorescence imaging with corrected PM dye signal from the red detection channel was obtained. This process is graphically illustrated in **Figure 29**.

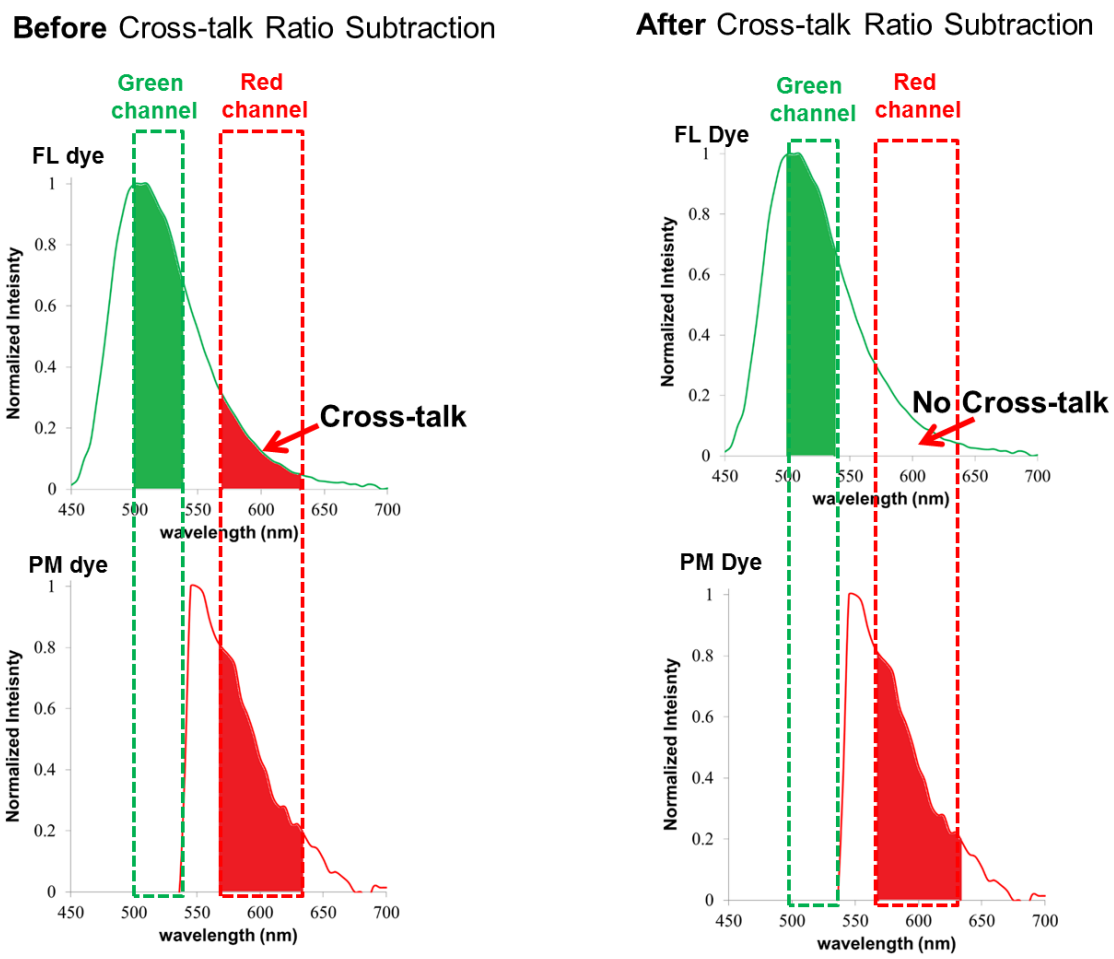

Figure 29 Graphic illustration of concurrent multi-spectral imaging before (left) and after (right) applying the Cross-talk Ratio Subtraction (CRS) method. **Left:** before the CRS algorithm, PM dye signal and a confounding FL dye cross-talk signal were detected in the concurrent Red channel. **Right:** after the CRS algorithm, the FL cross-talk was mitigated and only the true PM dye signal was detected in the Red channel.

The consistency of the CR was tested and the concurrent imaging with CRS algorithm was qualitatively and quantitatively demonstrated.

First, the consistency of the FL dye Cross-talk Ratio was tested by imaging the same FL target in the phantom over a range of distances between the SFE scope and the target. The CR was

calculated and plotted as a function of the distance. The results, as shown in **Figure 30**, demonstrated that the CR remained constant (0.225 ± 0.012) within the 15-40mm range and was relatively consistent (0.207 ± 0.025) across the 15-95mm distance range. Distances less than 15 mm were not included as the PMT detector was saturated, whereas at distances more than 95 mm, the signal intensity was too low to be measured.

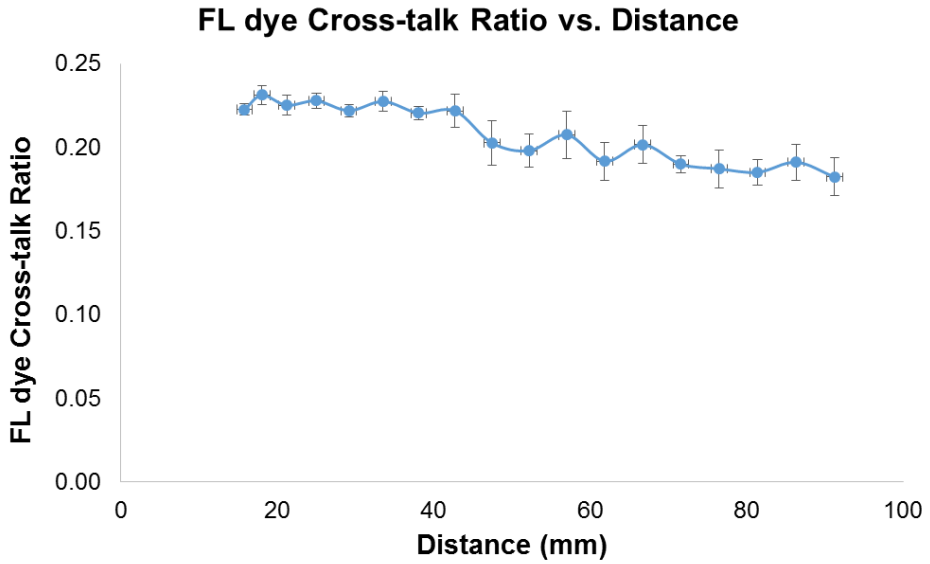

Figure 30 The FL Cross-talk Ratio was plotted as a function of the distance between the distal end of the SFE endoscope and the fluorescence target. The ratio remained constant (0.225 ± 0.012) over a distance range of 15-40mm and remained relatively consistent (0.207 ± 0.025) across a distance of 15-95mm.

During concurrent SFE dual-fluorescence imaging of FL and PM targets, before applying the FL Cross-talk Ratio Subtraction (CRS) algorithm, the FL-only targets exhibited erroneous fluorescence signal in the red channel (**Figure 31** (b)). Once the CRS algorithm was applied, the confounding FL red channel signal was strongly attenuated, and the erroneous FL image was removed (**Figure 31** (e)).

This cross-talk also acted as a confounder and interfered with the green FL dye fluorescence display, causing it to appear with a subtle yellow shade **Figure 31**(c) by the addition of red channel bias to the green channel. The FL-only targets were therefore misrepresented in the display as two-dye targets since they had fluorescence signals from both the green and red detection channels. After applying the CRS algorithm, the confounding FL red channel contribution was removed and the green FL targets appeared in the correct green color (**Figure 31** (f)). The concurrent two-dye target imaging after applied the CRS algorithm in **Figure 31**(f) showed correctly rendered green FL , red PM, and orange two-dye display images.

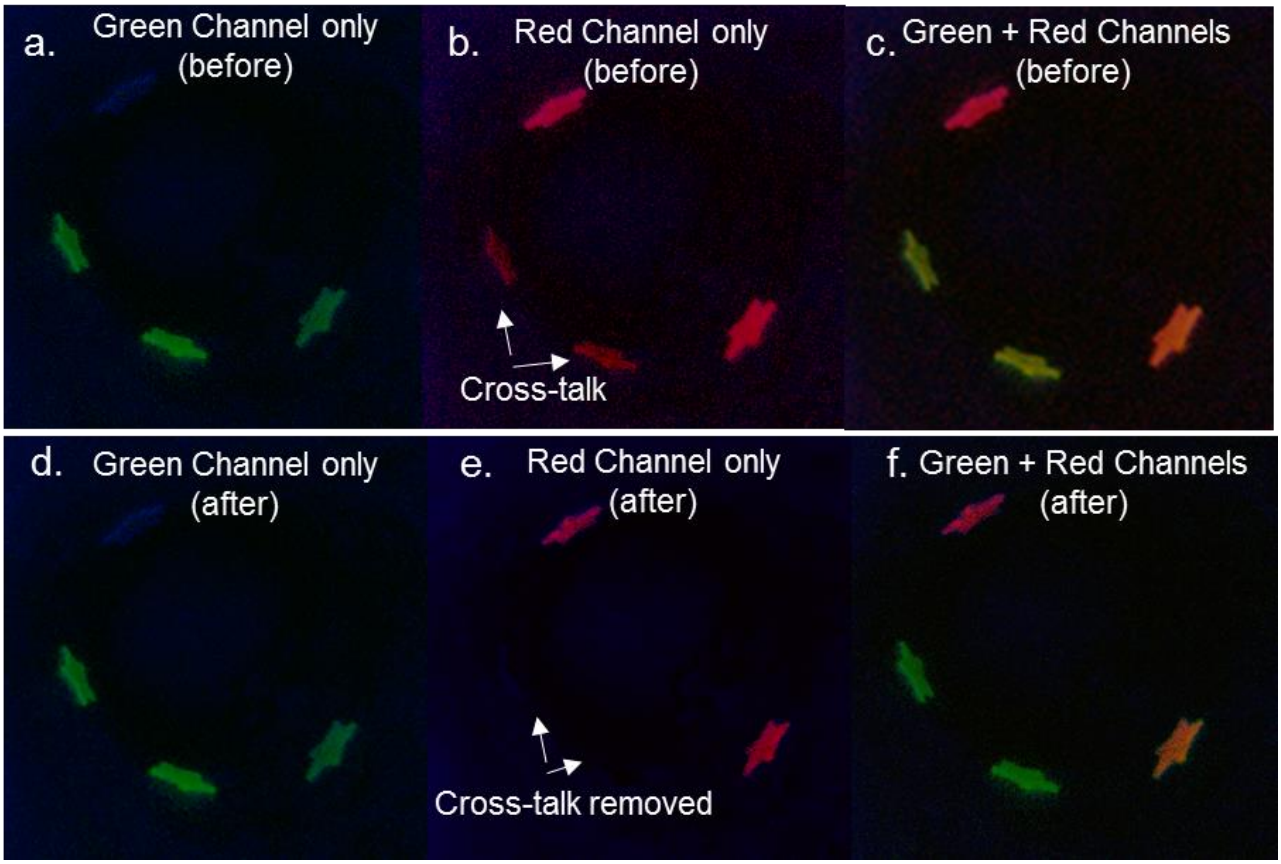

Figure 31 Concurrent multi-spectral fluorescence SFE imaging of the BE phantom at 30Hz frame rate. (a) - (c) Green, red, and combined display channels before applied CRS algorithm. (b) The FL-only targets exhibited erroneous fluorescence signal in the red channel. (c) Green FL appeared with a subtle yellow shade by the addition of red channel bias due to FL emission cross-talk with the red dye channel. (d) - (f) Green, red, and combined display channels after CRS algorithm was applied. (e) The confounding FL red channel signal was strongly attenuated after CRS. (f) The combined image after CRS showed correctly rendered green FL, red PM, and orange two-dye images. All images were single-frame raw video outputs from SFE imaging (80 degree field of view, 500-line resolution).

Furthermore, quantitative measurements of fluorescence intensity dependence on dye concentration were conducted and the results are shown in Fig. 12. In this series of experiments,

the PM dye with a range of concentrations (25, 50, 75 μmol/L respectively) were mixed with a constant concentration (100 μmol/L) of FL dye. A target with no dye-in-polymer was also used into obtain the system noise floor. The "true" PM signal was obtained by activating only the 532 nm laser and recording the red channel signal from the PM target. Initially, using concurrent laser excitation the red channel detector signal from the PM fluorescence was contaminated by the FL cross-talk signal (**Figure 32** (a)). Therefore, in **Figure 32** (a), before the CRS algorithm, the fluorescence signal from the red detector channel deviated from the true PM curve. However, after applying the CRS algorithm (**Figure 32** (b)), the red fluorescence signal closely matched the true PM fluorescence curve and the cross-talk signal was reduced by over 90%.

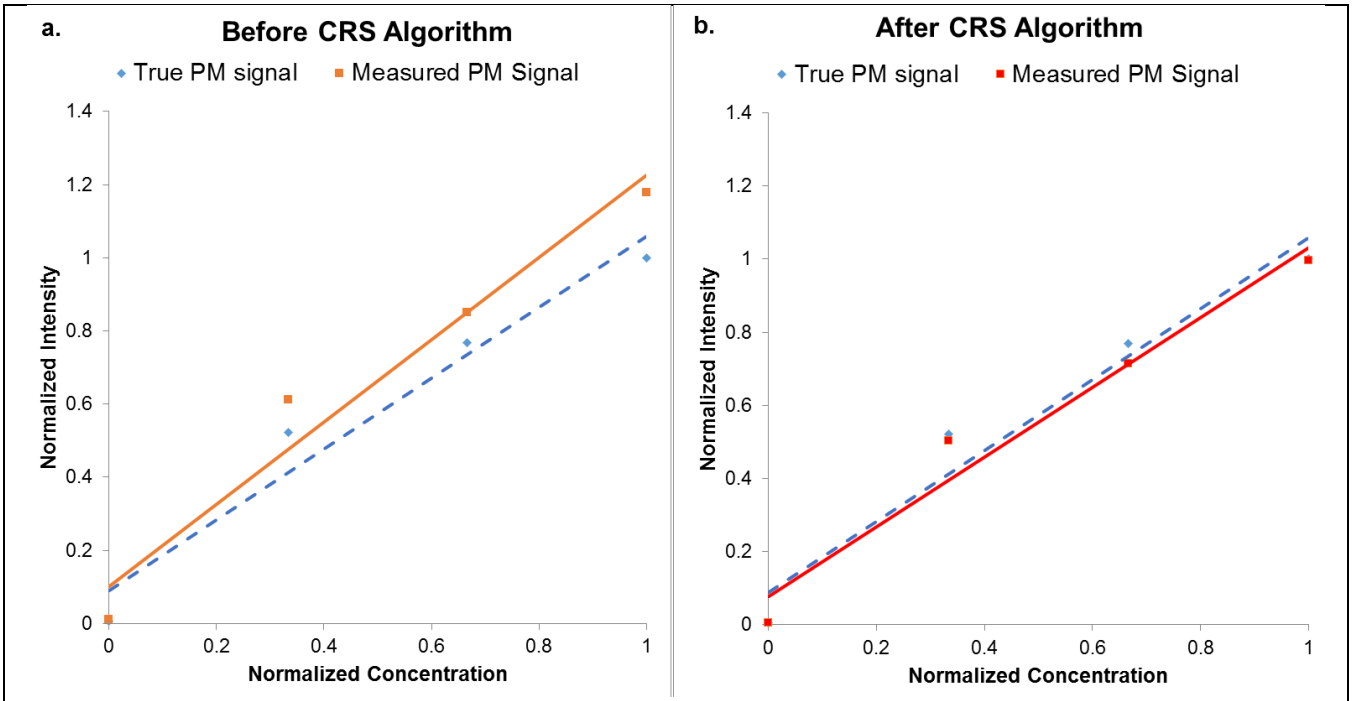

Figure 32 Comparison of the signal from the red output channel to the true PM targets signal during concurrent multispectral fluorescence imaging: **(a)** Before applying the CRS algorithm, the red fluorescence signal from the red detection channel (solid line) deviated from the true PM curve (dashed line). **(b)** After applying the CRS algorithm, the red fluorescence signal (solid line) closely matched the true PM fluorescence curve (dashed line).

4.3.2.3 Sequential multispectral fluorescence imaging

The sequential excitation of the R (635 nm), G (532 nm), B (442 nm) lasers was successfully implemented in the SFE system. As described in **Figure 25**, for the output, a red reflectance image, a (PM red fluorescence + green reflectance) image, and a (FL green fluorescence + blue reflectance) image were sequentially received at a 30 Hz frame rate, resulting in 10 Hz frame rate for the combined two-dye fluorescence imaging.

In Figure 13, the combined two-dye images contained fluorescence signals from the red and green detection channels with the reflectance signal from the blue detection channel. In concurrent laser

excitation (**Figure 33** (a)), the FL cross-talk signal in the red output channel was present. However, under sequential laser excitation imaging (**Figure 33** (c)) temporal separation of the excitation produces uncontaminated images of the PM and FL dye emissions. As presented earlier, it is known that the FL and PM dyes do not have overlapping blue (442nm) and green (532nm) excitation and therefore sequential excitation is sufficient to separate the overlapping dye emissions.

In the current study, the red reflectance image was also received at every cycle and can be used as an option for Distance Compensation: a pixel-by-pixel intensity computation using a non-linear ratio of the fluorescence and red channel reflectance ($F / (R^{1.5})$) [67].

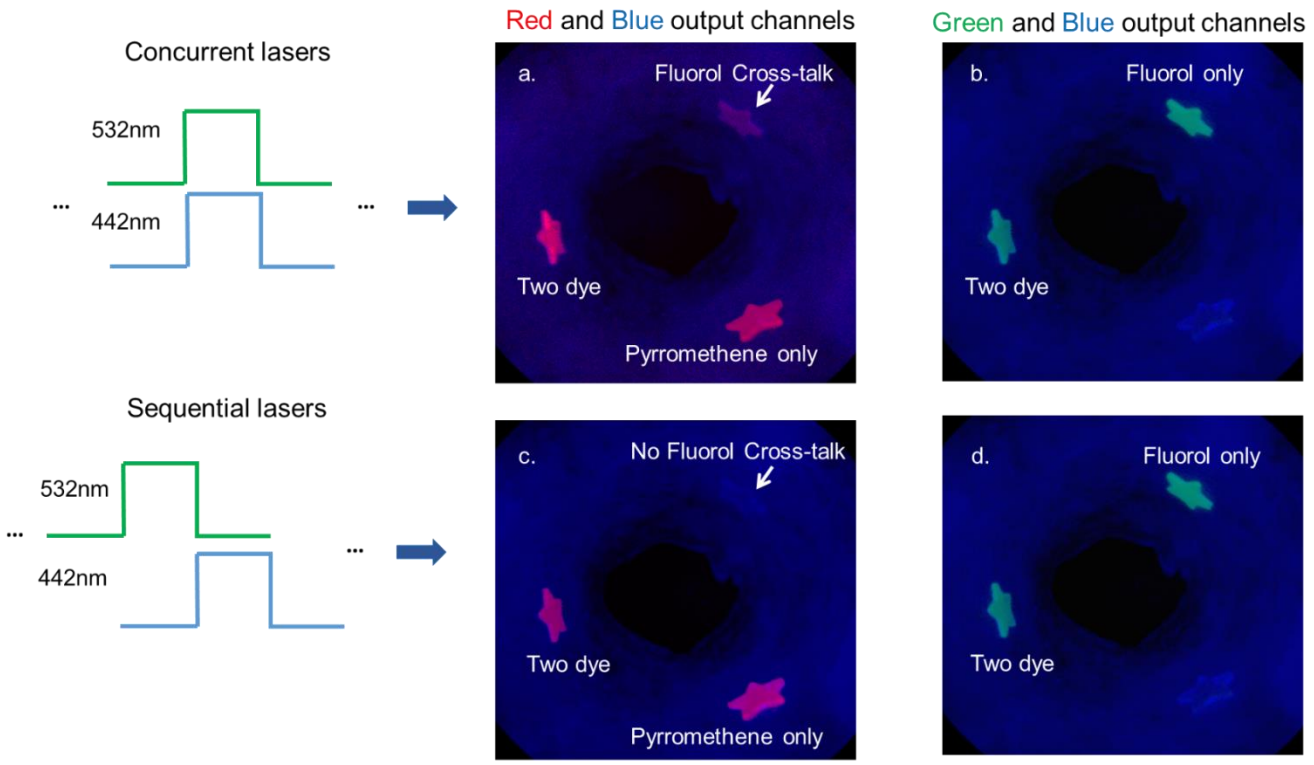

Figure 33 Concurrent laser excitation compared to sequential laser excitation results. In concurrent laser excitation, the FL cross-talk signal was observed in the red output channel in **(a)**, whereas in sequential laser excitation, only PM fluorescence signal was received in the red output channel and no FL cross-talk was observed **(c)**.

4.4 Discussion

Cross-talk is a confounding factor when two or more spectrally intersecting fluorescent dyes are used in endoscopic diagnostic imaging. Approaches to mitigate the fluorescence cross-talk were proposed and tested in this study using a 1.2 mm diameter wide field-of-view endoscope (SFE). The solutions evaluated in the current study were: (1) image stitching, (2) Cross-talk Ratio Subtraction (CRS) algorithm, and (3) frame-sequential imaging.

In **the first approach** of stitching to merge multiple fluorescence video frames into a panoramic image, cross-talk was avoided because each fluorescent target was illuminated with one laser

excitation wavelength and the corresponding emission was captured in the appropriate detection channel. The resultant mosaic map display of the lower esophagus (**Figure 29** (c)) showed distinguishable green FL-only, red PM-only, and orange two-dye targets with no emission cross-talk observed.

Meanwhile, the stitched multi-spectral fluorescence mosaic encompassed a much wider view of the observation area than that captured from a single endoscopic frame, and could be used for intraoperative navigation for hot-spots biopsy, or saved as the patient electronic medical record for longitudinal surveillance. Moreover, the mosaic map can also be used for extended review by the physicians without photobleaching decreasing the fluorescence signal. The current stitching software generates results within 1 minute with good spatial registration score [101], and its performance can be improved using higher processing speed.

However, there are drawbacks in implementing the stitching approach. Firstly, it does not offer true concurrent imaging and visualization of multi-spectral fluorescence targets, instead, it requires the running of multiple individual scans, which can be slow for clinical practice. This delay can also complicate the image stitching processing, where the stitching algorithm uses shared anatomical features from the reflectance images and assumes that these features remain static between different scans; however, in a typical *in vivo* setting, unpredictable motions, specular reflections from saline solutions or mucous, and other factors could cause feature shifts to appear in each scan, and therefore, a more robust algorithm for this approach would be needed and will need to be explored for *in vivo* implementation.

The second approach, concurrent imaging with Cross-talk Ratio Subtraction algorithm (CRS), performs simultaneous imaging where all fluorescence species are illuminated and their fluorescence emissions collected at the same time. In this case the cross-talk signal was successfully attenuated in real-time by applying the CRS algorithm (described in Equation 1, 2,

and **Figure 29**). The algorithm was applied to the SFE red detection channel during a pre-scan calibration. The FL dye Cross-talk Ratio (CR) remained consistent over a range of imaging distances (**Figure 32**). Specifically, the ratio remained constant (0.225 ± 0.012) within a distance of 15-40mm and kept relatively consistent (0.207 ± 0.025) across a distance of 15-95mm. For *in vivo* clinical practice in the luminal esophagus, a distance under 40 mm is a realistic working distance between the endoscope and region of interest under scrutiny by the clinician. The results also showed that the confounding FL dye cross-talk signal was strongly (>90%) reduced (**Figure 31**), and quantitative analysis showed that the fluorescence signal closely matched the "true" PM dye fluorescence intensity (**Figure 32**).

Compared to the image stitching approach, the concurrent imaging approach provides visualization of multi-spectral fluorescent targets/hot-spots simultaneously and in real-time. This concurrent method is beneficial for wide-field endoscopic imaging and image-guided biopsies. Viewing coincident emission signatures from multiple dyes will provide a more accurate molecular diagnosis than a single fluorescent marker [74] [100] [57] [109]. Moreover, the concurrent imaging approach is more robust and accurate than the image stitching approach for *in vivo* settings since the removal of dye cross-talk is not affected by unpredictable motion or specular reflections that complicate image indexing.

In the current study, the emission spectral overlap only happened in one detection channel for the two fluorophores that were used as demonstration. This demonstration showed a simple but effective example of the Crosstalk Ratio Subtraction Algorithm application. It can be extended to other cases in wide-field multispectral fluorescence endoscopic imaging where more than two cross talk channels are involved. Meanwhile, according to the emission spectral profiles of the molecular probes currently under development (shown below in **Figure 34**), this study has successfully simulated the dye emission crosstalk problem, and the solution was implemented in

a newly developed multispectral SFE system (details can be found in the next chapter) for real-time application in the upcoming BETRNet *in vivo* study at University of Michigan.

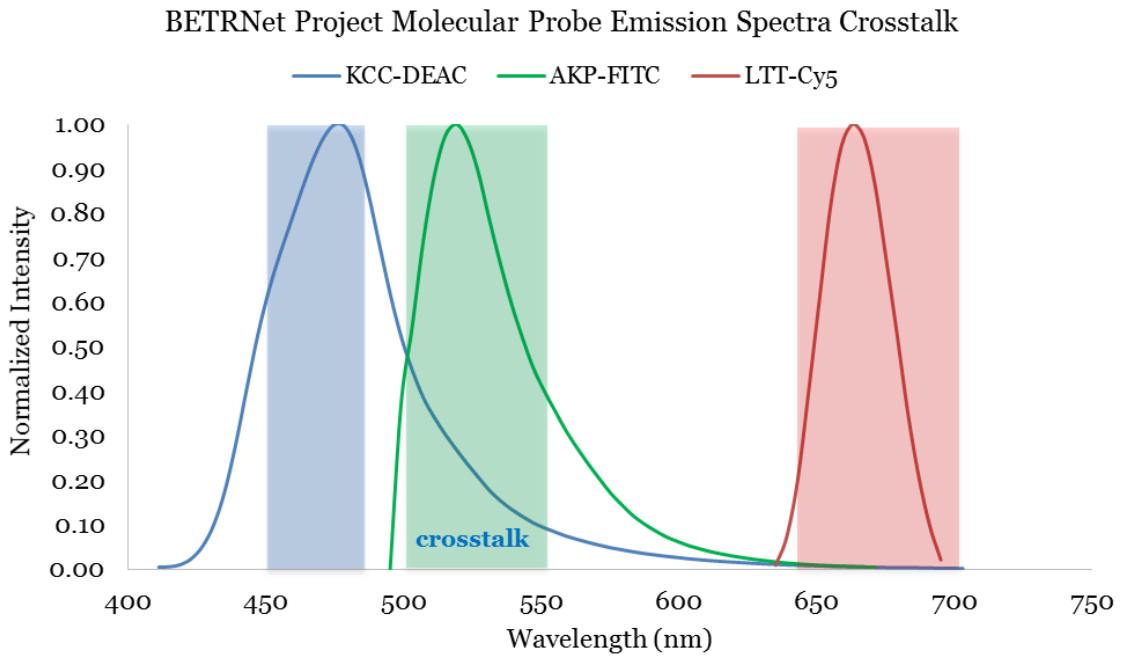

Figure 34 Normalized emission spectral profiles for 3 molecular probes to be used in the upcoming BETRNet project *in vivo* study. The 3 molecular probes are peptide-fluorophore conjugates which are designed to target molecular signatures, such as cell membrane proteins, that are specifically associated with high-grade dysplasia (HGD) in Barrett's esophagus. The goal for concurrent multiple probe targeting is to increase the sensitivity for diagnosis of HGD. This figure shows overlaid KCC-DEAC, AKP-FITC and LTT-Cy5 probe fluorescence emission, measured from a NanoDrop Fluorospectrometer (Thermo Scientific, Inc, MA, USA). Solid blue, green and red colored blocks show the emission bandpass on each fluorescence detection channel. As shown in the plot, that the emission of probe KCC-DEAC has crosstalk with probe ACP-FITC in the green fluorescence channel. This emission crosstalk situation is very similar to the FL and PM dyes' crosstalk demonstrated in the current study.

Furthermore, to guarantee the accuracy of quantitative fluorescence imaging, there are also restrictions on the scenario that this algorithm could be applied. The following section discusses the criteria for the application of CRS Algorithm in the scenarios listed below. The following discussion uses the Alexa Fluor dye family to highlight the criteria and limitations for the Cross Talk Ratio Subtraction Algorithm. Alexa Fluor is a family of fluorescent dyes that match the spectral profiles of the most commonly used fluorophores (Alexa Fluor 488: Fluorescein or FITC, Alexa Fluor 555: CY3, Alexa Fluor 647: Cy5, Alexa Fluor 680: Cy5.5, Alexa Fluor 750: Cy7). Alex Fluor dyes also have good photostability and quantum yield. Furthermore, the Alex Fluor dye family can be conjugated with antibody probes. Dye excitation-emission spectra sources are from Life Technologies, Inc. (Grand Island, NY, USA).

Criteria for the Concurrent Imaging with CRS Algorithm

Figure 35 Case 1: Multiple fluorophore emission spectral overlap, but the crosstalk in detection channels is only between two fluorophores (assuming overlap with intensity <5% is close to or lower than noise floor, and therefore does not account towards detected crosstalk signal) , which is similar to the two-dye crosstalk case demonstrated in the current study. CRS algorithm can be directly applied to detection channels to mitigate the crosstalk signal.

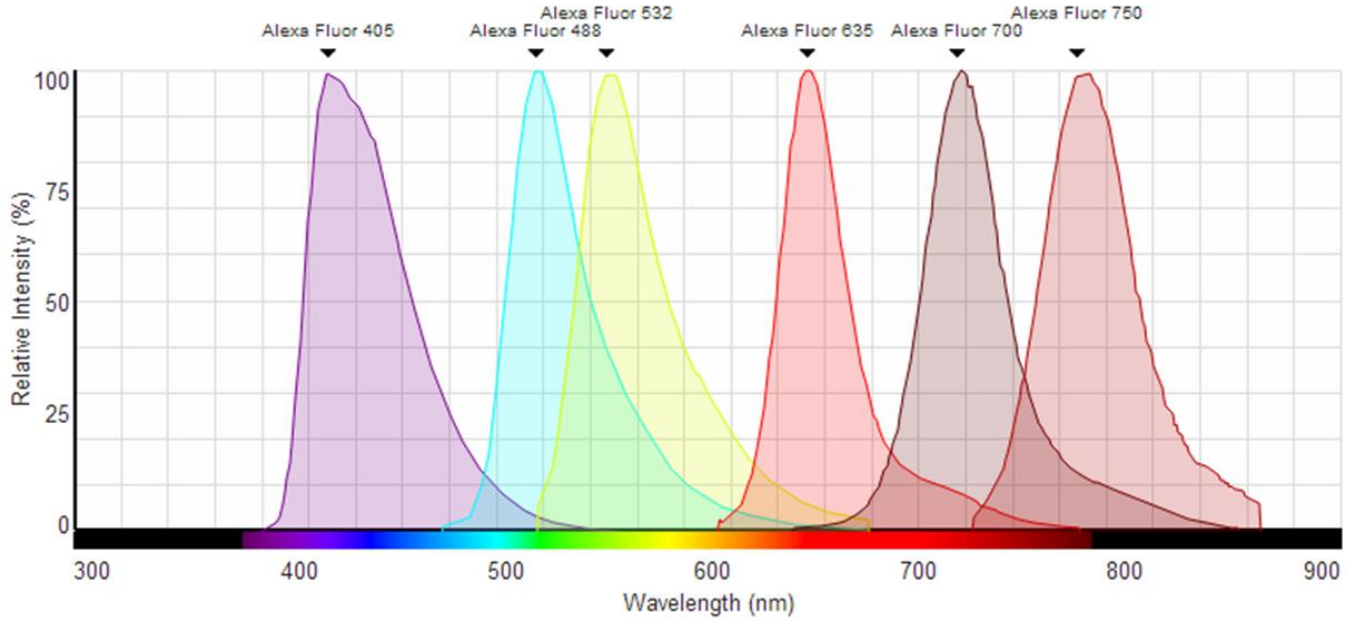

Figure 36 Case 2: Only 2 fluorophore detection channels crosstalk, but overlapped spectral area is over 80% of each individual spectral area. In this case, an extended formula of the CRS algorithm is listed below:

Intensity_Fluor568 = A * Intensity_DetectionChannel 1 + B * Intensity_DetectionChannel 2;

Intensity_Fluor594 = C * Intensity_DetectionChannel 1 + D * Intensity_DetectionChannel 2.

A, B, C, and D are pre-calibrated parameters/ratios.

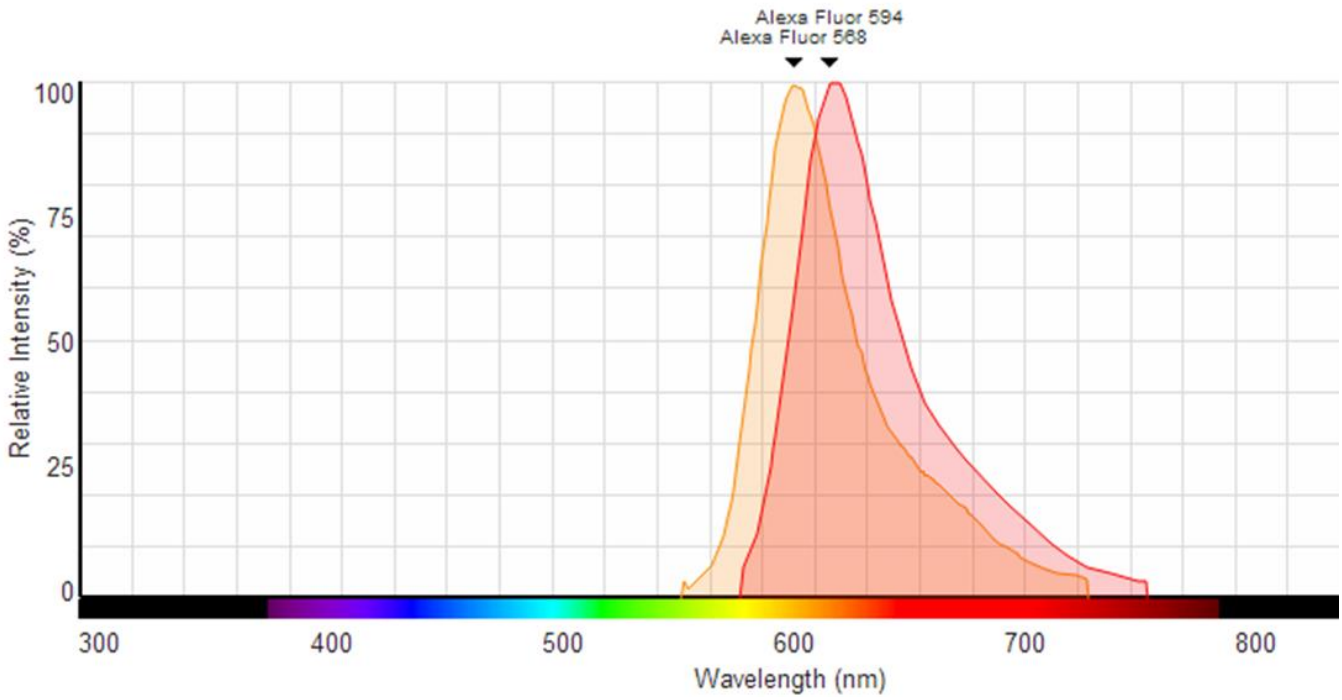

Figure 37 Case 3: Three fluorophore emission spectra crosstalk in one detection BUT the overlapped areas are not all above 80% of each individual emission spectral profile area:

Intensity_Fluor700 = Intensity_DetectionChannel 1 + A * Intensity_DetectionChannel 2 ;

Intensity_Fluor750 = B * Intensity_DetectionChannel 2 + C * Intensity_DetectionChannel 3 ;

Intensity_Fluor790 = D * Intensity_DetectionChannel 2 + E * Intensity_DetectionChannel 3.

A, B, C, D and E are pre-calibrated parameters/ratios.

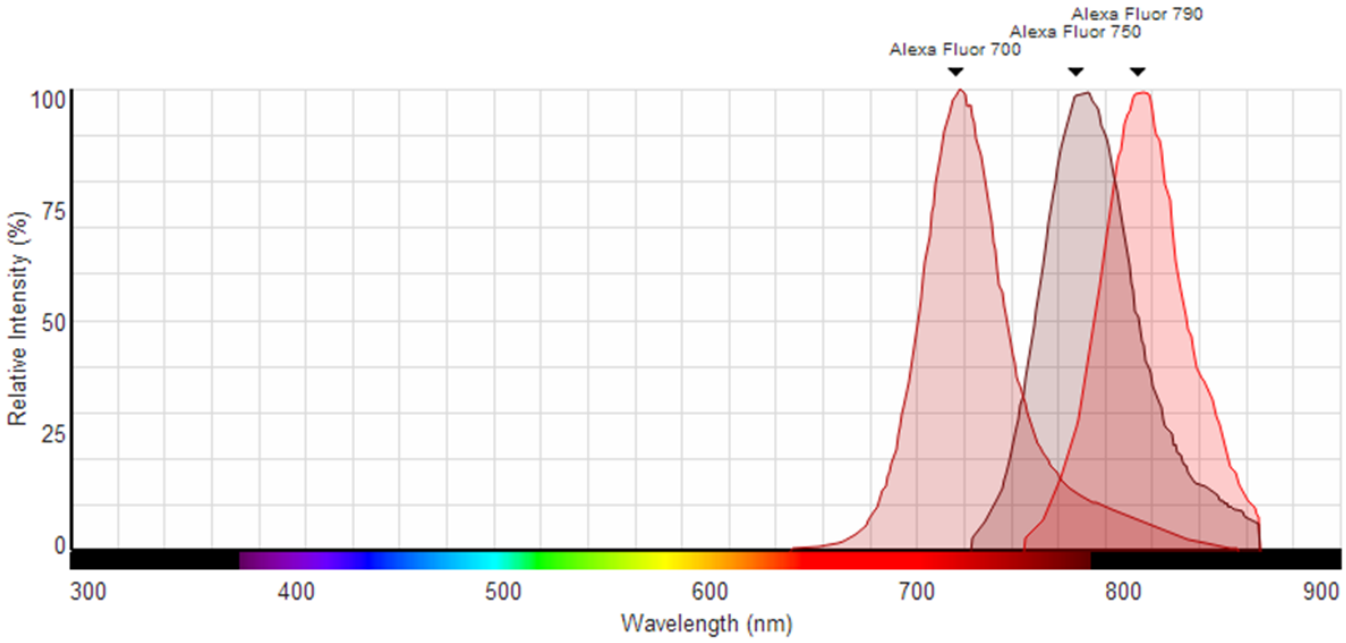

Figure 38 Case 4: More than 3 emission spectra crosstalk in one detection AND the overlapped areas are all over 80% of each individual emission spectral profile area – Difficult to implement Crosstalk Ratio Subtraction Algorithm in real time with high confidence for the accuracy of quantifiable fluorescence intensities, even though it's just for 3 detection channels. To solve problems similar to case 4, **the 3rd approach – Sequential Imaging** was proposed, and a Frame-sequential Imaging approach was implemented and demonstrated in the current SFE system.

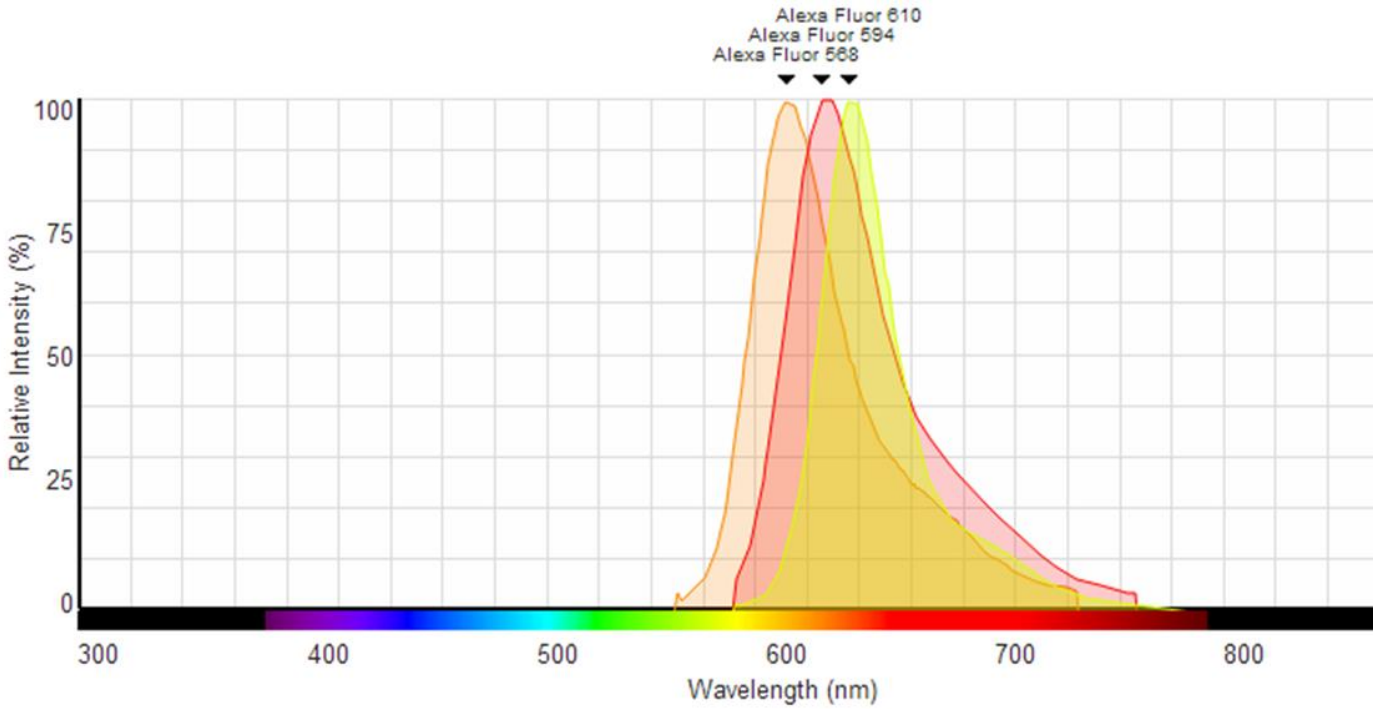

The third approach, frame-sequential imaging, was carried out by timed excitation and light collection from only one fluorophore species at a time. This temporal separation of laser illumination and light collection minimizes cross-talk (both for excitation and emission) in a manner similar to the image stitching approach; however, instead of collecting the emission signal separately and processing groups of image frames, the frame-sequential imaging method cycles through all of the laser excitation and dye emission combinations at 30Hz. Therefore, the relatively stationary position of organs and tissue during the fast frame rate imaging process

removes the need for image registration. Meanwhile, visualization of multi-spectral fluorescence hot-spots can be achieved by combining each cycle of image outputs: red PM dye fluorescence, green FL dye fluorescence and blue reflectance into combined RGB image frames which can be displayed in real-time during the endoscopy procedure.

In standard RGB operation, the SFE refresh rate is 30Hz since the image is a composite of all three concurrent colors. However, in the sequential imaging mode the SFE system runs at a 10Hz frame rate (or 15Hz if Distance Compensation algorithm is not applied) for each of the individual fluorescence and reflectance frames. Therefore, when the number of fluorophores increases, the frame rate for the sequential images must increase by a factor somewhat larger than the number of fluorophores in order to display a real time view that adapts to body and endoscope movements. Imaging with a low frame rate will be limited to viewing objects that undergo very slow motions, which may not be adequate for clinical endoscopy.

Pixel-sequential Imaging

When the number of overlapped fluorophore emissions in one detection channel increases to more than 3, and together with the spectral overlap exceeding 80% of the spectral area, the difficulty to perform accurate quantitative fluorescence molecular endoscopy using CRS algorithm increases. Meanwhile, with unpredictable body movements as well as unevenness and folding in certain anatomical regions, Image Stitching as a cross-talk mitigation approach might lose accuracy and reliability as well. Under these circumstances, sequential imaging at pixel rate will be a feasible and efficient solution to mitigate fluorescence crosstalk for molecular endoscopy at video-rate. In addition, sequential imaging not only mitigates crosstalk in fluorophore emission, but also reduces excitation crosstalk, by sequentially exciting and collecting each dye specie individually.

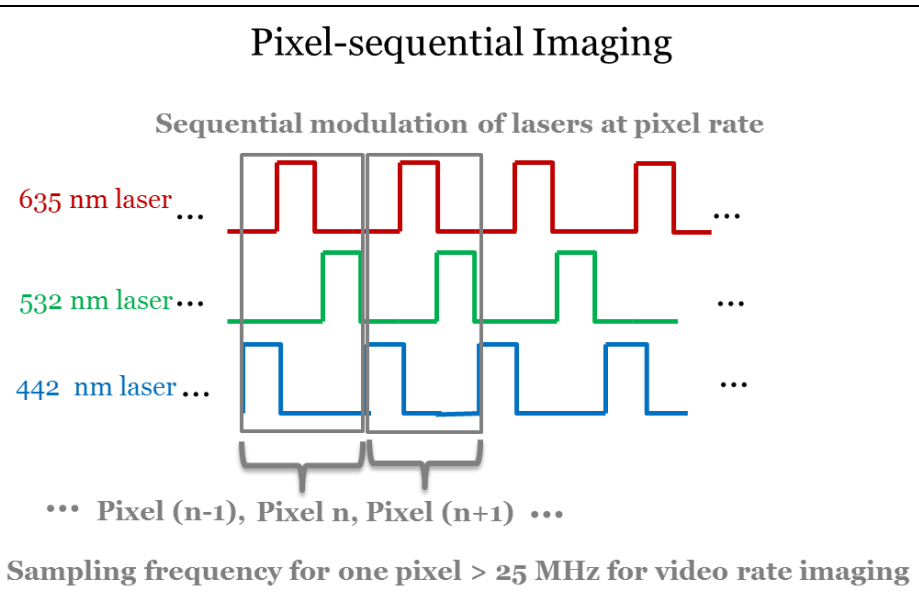

Figure 39 Pixel-sequential Imaging. Compared to Frame-sequential Imaging, which switches lasers on and off at video frame rate (e.g., 30 Hz), the pixel-sequential imaging requires modulation of lasers at pixel acquisition frequency. Standard wide-field high-resolution SFE system operates at a pixel sampling frequency of 25 MHz, therefore, for concurrent imaging of 3 fluorophores, 75 MHz modulation will be needed.

Sequential imaging at pixel rate, or Pixel-sequential Imaging, as illustrated in above **Figure 39**, using an example of 3 concurrent fluorophores, requires sequential excitation and detection of multiple cross talk fluorophores at or even above the sampling frequency applied to acquire each pixel within the image frame. This definition is similar to the Frame-sequential Imaging, except that the latter only requires sequential excitation and detection of multiple cross talk fluorophores at the standard frame rate refresh frequency (30Hz) to form each frame. The standard wide-field (>80 degree), high-resolution (<50 microns) and video rate (30Hz) SFE system uses an 11 kilohertz (kHz) scanner to generate real-time imaging at 250-lines (2000 points) per frame. The standard sampling rate to acquire data and generate images used by the SFE system is 25

Megahertz (MHz). Therefore, the electronic control for the laser diode is required to modulate individual laser on and off at a rate that's greater than the number of fluorophores multiplied by the 25 MHz imaging sampling frequency. For example, a number of 3 fluorophores will need a laser modulation frequency at above 75 MHz. When it comes to applications for concurrent imaging of >10 fluorophores, the requirement for the laser diode driver will need to be at almost gigahertz (GHz) frequency. This type of laser control electronics has been advanced thanks to the entertainment and display industry. For example, a highly integrated 250 MHz laser driver can be found off-the-shelf as part of a laser component for pico projectors (MAX3601, Laser Driver for Projectors, Maxim Integrated, Inc, San Jose, CA, US), and it supports high speed laser modulation for red, green and blue lasers for video imaging.

Meanwhile, at the detection end, since the acquisition happens in a timed and sequential fashion, one channel with one PMT detector might be sufficient to detect fluorescence emission at least at the visible range (R9880U series, Hamamatsu Inc., NJ, US). If the applications involve concurrent imaging of both visible and NIR fluorophores, a 2nd detection channel with a PMT that is optimized for high signal-to-noise ratio NIR detection might be needed. For example, a typical NIR dye – ICG's peak emission wavelength is 800-820 nm, which is out of the detection response range of the typical PMTs used in the SFE system (the R9880U series listed above). Therefore, a photodetector with longer wavelength response is needed. At the same time, as higher dark current usually occurs with longer wavelength spectral detection (e.g., in the same R9880U series, the red PMT has 10x dark current compared with the blue-green PMT), reducing the PMT temperature and thus decrease the electronic noise floor, is another good method to increase the SNR on the detector. For example, a longer wavelength response PMT (R9182-01, Hamamatsu Inc.) can be coupled with integral Peltier cooling, with a separate thermoelectric cooling controller (C12473, Hamamatsu Inc), which could reduce the dark current by 5-10x. This 2-detection-

channel design ultimately reduces the size and potentially the cost for the detection in the SFE system, especially compared with the standard design when the number of fluorophores increases.

Figure 40 The detection system for concurrent multispectral SFE imaging. **(a).** A 2-channel detection system for concurrent multispectral SFE imaging with Pixel-sequential Imaging to mitigate spectral crosstalk. One channel is dedicated to fluorescence emission detections in the blue-green range, using a PMT that has optimized SNR at visible range, the other channel is for emission in the red-NIR range, with a PMT optimized for long wavelength and Peltier cooling to further reduce dark current. **(b).** As comparison to (a), current detection system for the same fluorescence-reflectance imaging has two more detection channels.

(a)

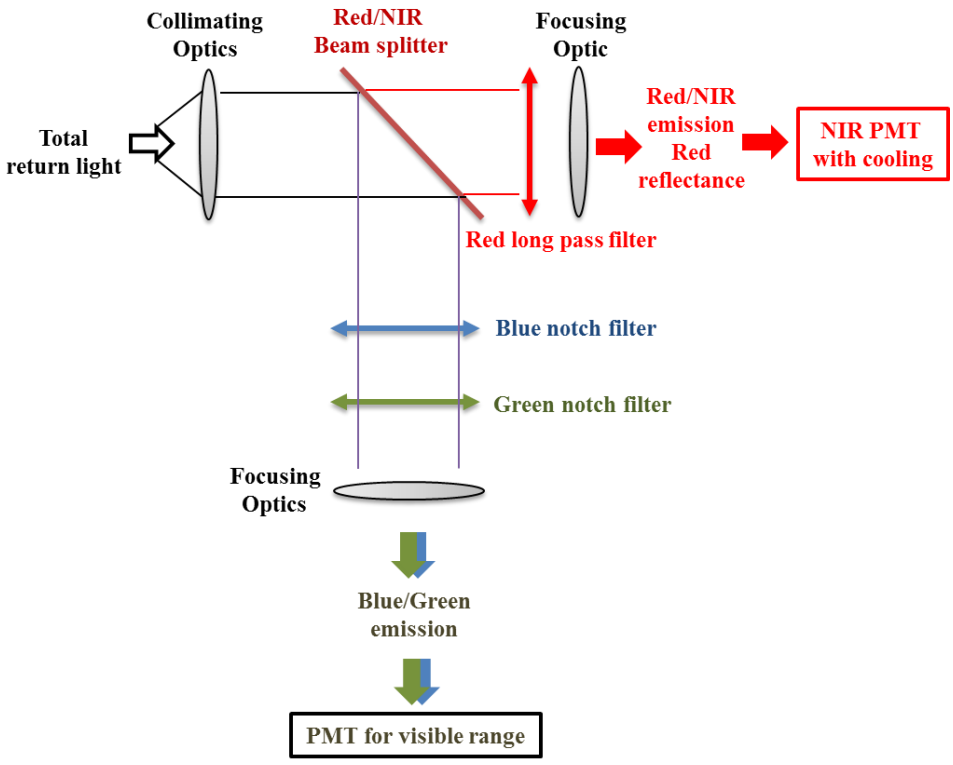

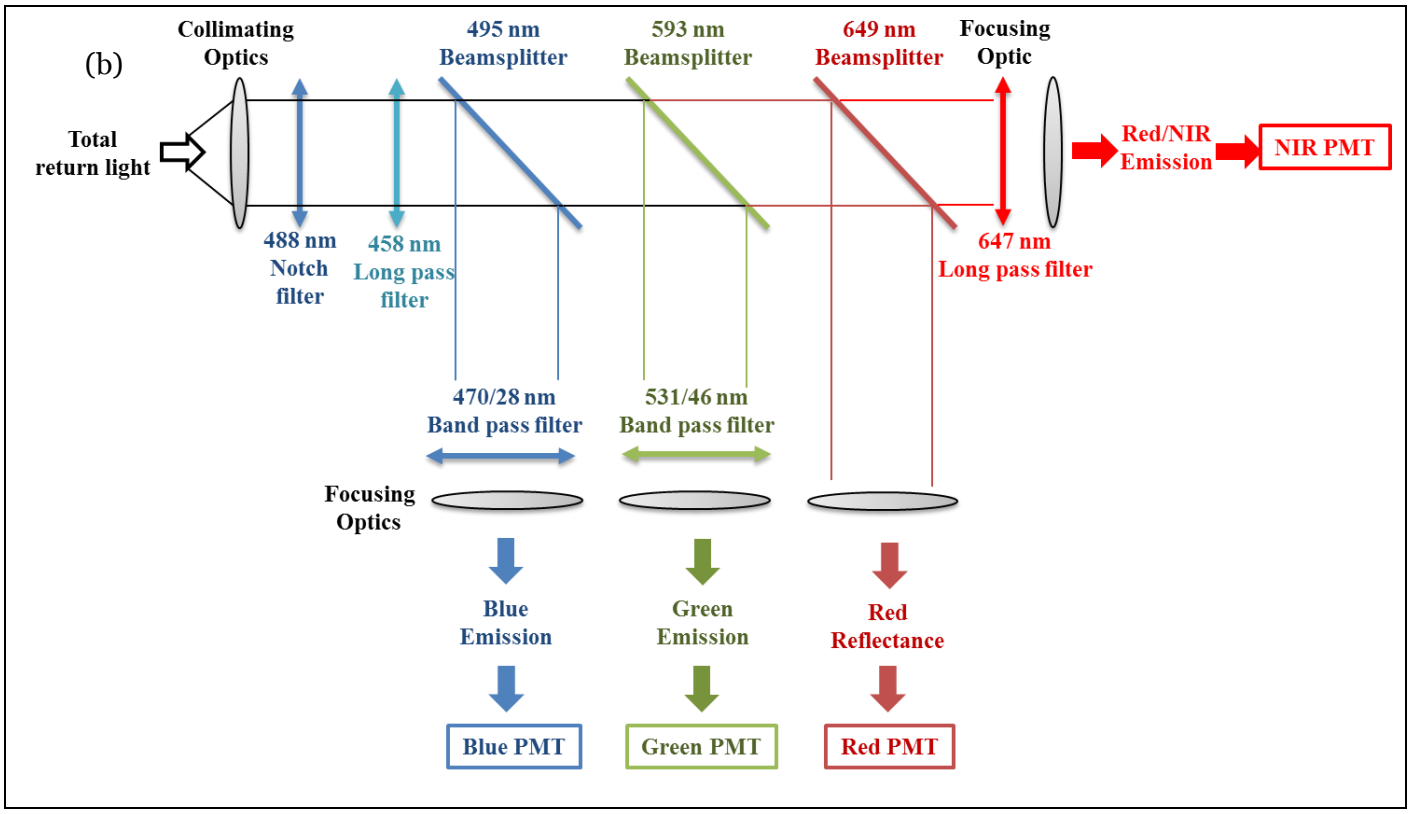

The summary of the three approaches proposed and demonstrated in the current study are listed in **Error! Reference source not found.4** below:

Table 4 Strengths and Limitations for the Three Separate Solutions

Solutions	Strengths	Limitations	Comments
(1) Image Stitching	a. Avoids dye cross-talk b. Can be used for extended review and less susceptible to fluorescence photo-bleaching c. Can be saved as patient record	a. Data processing intensive and slow. b. Algorithms may not be robust enough to compensate for unpredictable motion	Software and algorithm improvements are needed for real time implementation

		and other factors for *in vivo* imaging	
(2) Concurrent Imaging Using CRS Algorithm	a. Reduces dye cross-talk b. Real time c. Compatible with *in vivo* clinical scenario	a. Pre-scan calibration is needed and device settings must be maintained b. Confidence for accuracy reduces if >3 fluorophores crosstalk in one channel with > 80% spectral overlap	Implemented on the new multispectral SFE system for *in vivo* study
(3) Sequential Imaging	a. Avoids dye cross-talk b. No pre-scan calibration is required c. Near real-time for Frame-sequential imaging and real-time for Pixel-sequential imaging d. Compatible with *in vivo* scenario	Refresh rate must increase as a function of the number of fluorophores	Frame-sequential imaging implemented on the new multispectral SFE system for *in vivo* study, but hardware improvements needed for Pixel-Sequential imaging

In the future, using these crosstalk mitigation approaches discussed above, either in an independent or joint/hybrid approach, combined with the unique system design of SFE imaging platform technology, wide-field multi-spectral fluorescence-reflectance endoscopic imaging with ~10 or more fluorophore species will be implemented for customized applications. Given the wide variety of fluorophores available for life science and clinical applications (examples in **Table 5**),

this combination of hardware-design and software/algorithm approach allows the SFE system to meet the needs to accommodate for flexible choices of fluorophores with multiple wavelengths ranging from visible to NIR range, and the applications will no longer be "locked" with only a set of fluorophore combinations.

Table 5 Example fluorophores from visible to NIR range that can be selected for wide-field multispectral fluorescence SFE imaging with implementation of crosstalk mitigation algorithm. However, *the candidate fluorophores are not limited to the examples listed below*.	
Fluorescent dyes	FDA approved (as of April, 2014): Fluorescein, Methylene Blue, ICG Examples of other fluorophores used in life science and/or clinical studies: Alexa Fluor® Family: 350, 488, 546, 555, 568, 594, 647, 680 Pacific Blue™, Coumarin, BODIPY® FL, Pacific Green ™, Oregon Green®, Fluorescein isothiocyanate (FITC), Cy®3, Pacific Orange ™, Tetramethylrhodamine (TRITC), Rhodamine, Texas Red®, Cy®5, Cy®5.5, Chlorella, Chlorophyll a, Chlorophyll b, Zwitterionic (ZW)800-1, LI-COR® IRDYE® 800CW, etc.
DNA stains	DAPI, SYTOX® Green, SYTO® 9, TO-PRO®-3, Propidium Iodide, etc.
Qdot® probes	Qdot® 525, 565, 605, 655, 705, 800, etc.
Fluorescent protein labels	R-Phycoerythrin (R-PE), Allophycocyanin (APC)

Expressed fluorescent proteins	CFP, GFP (emGFP), mCherry, RFP (tagRFP), etc.

Concept on achieving high target-to-background ratio (T/B) through mitigation of the background autofluorescence

Achieving a high target-to-background ratio (T/B) is a driving factor in the clinical realization of optical molecular imaging [72]. For *in vivo* optical imaging using exogenous targeted contrast agents, the non-specific binding and material accumulation (pooling) of contrast agent [110] [111] and tissue autofluorescence (AF) can cause a significant decrease in the T/B. AF is the major contributor to the background signal in topical application of fluorescence probes to epithelial tissue since non-specific accumulation is minimized in this situation [78].

The proposed approaches can also reduce the background tissue autofluorescence signals that degrade T/B. It has been reported that tissue AF signals can mask exogenous molecular probe fluorescence, which can limit the *in vivo* T/B [72] [73]. In the esophagus, stromal collagen is believed to be primarily responsible for the AF signal especially when excited in the near-UV to blue spectral range [73] [112] [113] [114]. Therefore, collagen AF could be a major confounder for commonly used fluorophores such as Coumarin, DEAC, and fluorescein. Molecular imaging studies [97] of mouse colon cancer using a fluorescein conjugated peptide marker produced a T/B of only 2-3 as a result of AF [14] [97]. Reducing the AF background signal can increase this T/B ratio. Eliminating the AF background using chemical agents such as Sudan black has been reported in confocal laser scanning microscopy but not applicable for *in vivo* clinical endoscopy [115]. On the endoscopic imaging device, if a detection channel was designated for autofluorescence, the AF image could be subtracted out from the fluorescent marker channel

using either concurrent or frame sequential imaging methods. These improvements could lead to an enhanced target-to-background ratio.

To test this concept an AF feature was added to a color matched BE phantom (**Figure 41**). To test this concept an AF feature was added to a color matched BE phantom (Fig. 14). The autofluorescence background feature was added to the Barrett's esophagus (BE) phantom [52]. In summary, collagen fibers (Collagen Type I, Insoluble from Bovine &, Sigma-Aldrich, St. Louis, MO) were converted to powder through heating, drying, and mechanical processing. De-ionized water (ddH2O) was added and the resulting paste was evenly applied over the phantom subsurface to simulate the stromal collagen layer. After drying, a paint simulated healthy and BE mucousal layer was applied evenly over the collagen layer and allowed to dry.

Autofluorescence background subtraction was shown to enhance image contrast for tumor detection [116], and it is embedded software technology in the commercially available IVIS benchtop system [117]. An estimate of the proposed T/B signal improvement was obtained by subtracting the AF background in **Figure 41** and the theoretical T/B increased from 4 to ≥ 10. This enhancement elevates the performance of UV-blue excited fluorophores (e.g. fluorescein) to the level achieved with red and NIR dyes [86] [98] which are excited and fluoresce in spectral regions considered more immune from AF. Currently, there are only two NIR fluorescent dyes that are FDA approved for in human use. One is indocyanine green (ICG) [118] [119], and the other one is methylene blue (MB) [120] [121]. MB is commonly used as a stain with deep blue hue, but it is also a fluorophore with peak absorbance at 665 nm and peak emission at 687, however, MB has a very small stock shift (22 nm) and a low quantum yield (4.5% in water) [122], comparing to ICG, it is less popular to be used as a fluorophore to be conjugated with antibodies or peptides to form molecular probes. On the other hand, ICG has a hydrophobic, large heptamethine interior that is surrounded by a negatively charged surface shell [123]. This molecular arrangement will result in comparatively high nonspecific binding and may degrade the T/B advantage of ICG

especially in systemic applications [123] [124]. In contrary, this charge distribution pattern is not present in the FDA approved fluorescein dye that has a peak excitation wavelength at 488 nm [118]. Less nonspecific binding of fluorescein combined with mitigation of its AF signal makes this dye a more viable choice for molecular imaging. Gaining FDA approval for any new dye is a very costly and time consuming endeavor and to date no other fluorescent dyes have received clearance for use in routine human clinical procedures. Therefore, any measure that enhances the performance of existing FDA approved dyes has significant translational impact for molecular imaging technology.

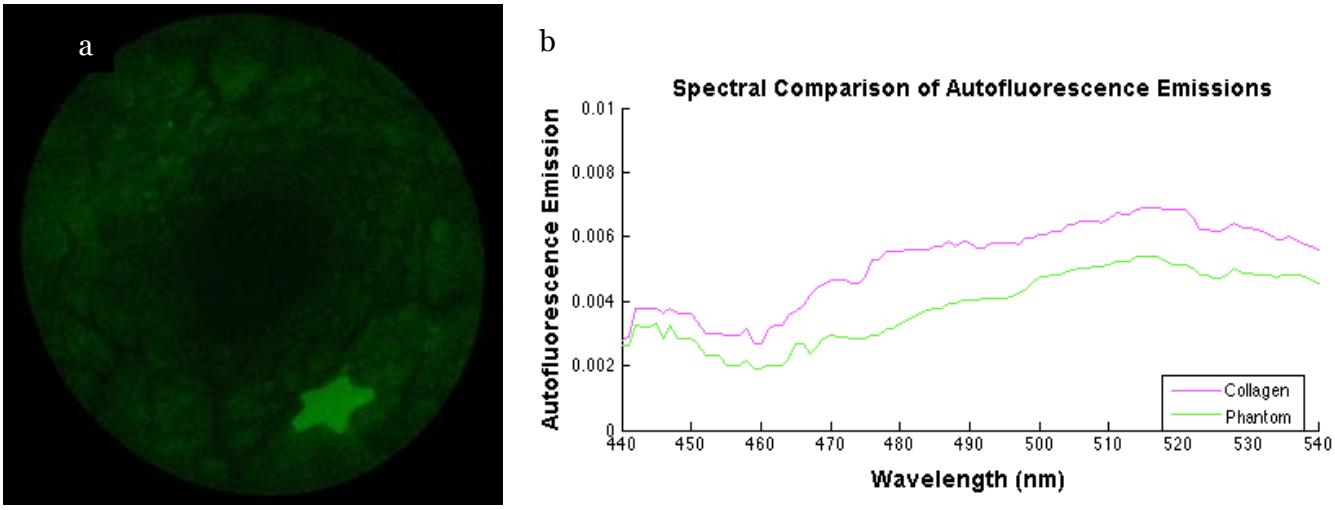

Figure 41 (a) Normalized fluorescence emissions captured by the SFE between 500-540nm after excitation at 442nm. The star shape is a FL-in-polymer dye target with a concentration of 1μM where as the background fluorescence is due to the embedded collagen AF. Image analysis shows the target to background signal ratio was 4:1. (b) Comparison of AF emissions shows that the phantom fluorescence emission is similar to that of pure collagen. Concerns that the excitation fiber exhibits autofluorescence was tested using a spectrometer (USB2000+, Ocean Optics, Inc). No autofluorescence signal was detected with the laser excitation power used in the current study.

Situations where cross-talk occurs for both dye excitation and emission, or cases with "extreme" cross-talk, where the two dyes' emissions completely intertwine, were not studied, as these situations can be avoided by selecting alternate dye labels. The probes which are likely to be used with the SFE for *in vivo* study in the near future are Coumarin (DEAC), Fluorescein, 5-TAMRA, CF-633, and Cy5.5 dyes [125]. These dyes exhibit moderate levels of intersection compatible with the three proposed spectral overlap solutions. For cases with extreme emission spectrum overlap, sophisticated algorithms such as linear-unmixing for laser scanning microscopy have been proposed and applied [85] [91] [126]. However, due to the additional data collection and processing time required, the linear-unmixing approach might not be suitable for real time wide-field fluorescence endoscopic imaging. In the current study, the image stitching approach and the frame-sequential imaging approach could be applied to solve cross-talk where the emission spectrum suffers from extreme overlap, by separately illuminating each fluorophore, receive and composite near real-time multi-spectral fluorescence imaging. Fluorescence life-time imaging is another feasible approach to delineate highly overlapped fluorescence. Recently fluorescence life-time imaging was applied to delineate fluorescent species [127], and detection of early cancer lesions [128]. Combining SFE imaging with time-resolved fluorescence spectroscopy was recently reported for biomedical assessment of the bile duct [129] and fluorescence life-time imaging holds potential for the delineation of overlapped multi-spectral fluorophores.

Studies using quantum dots (QDs) for multi-spectral fluorescence imaging have also been reported [130] [131]. Due to the uncertain toxicity and unknown side-effects, QDs are currently not FDA-approved and are less likely to be used in human trials than organic dyes. QDs have a symmetric and Gaussian-like emission spectral profile, and therefore less cross-talk than organic dyes [90]. However, in applications where multiple QDs are imaged simultaneously, emission cross-talk can still occur [132] [133], and the proposed solutions are applicable to spectral overlap of multi-spectral fluorescence nanoparticle imaging as well.

In conclusion, we proposed and evaluated three different approaches for the removal of fluorophore emission cross-talk in wide-field multi-fluorophore molecular imaging: Image stitching, Cross-talk Ratio Subtraction (CRS) algorithm, and frame-sequential imaging. To evaluate these solutions, an *in vitro* phantom with fluorophore emission cross-talk was constructed. The results showed that fluorophore emission cross-talk could be significantly reduced or successfully avoided. At present, the concurrent imaging method is viable for early stage cancer detection *in vivo* with the wide-field multi-fluorophore SFE imaging device with addition of an initialization step not unlike the white-balancing step for commercial endoscopes. Furthermore, a means to enhance fluorescence target-to-background ratio that is directly applicable to fluorescein (FDA-approved dye) by the reduction of autofluorescence background signal was demonstrated.

5 Target-to-Background Enhancement in Multispectral Endoscopy with Background Autofluorescence Mitigation for Quantitative Molecular Imaging

5.1 Introduction

Optical molecular endoscopic imaging with the administration of exogenous fluorophore probes has become an area of great interest in many clinical diagnostic and surgical applications [134] [135] [136] [73] [88] [137]. Numerous endoscopic applications for tracking exogenous targeted fluorescence are under investigation, such as detection and diagnosis of early cancerous lesions in Barrett's esophagus [138], navigation and demarcation of tumor margins during brain surgery [139] [83], and detection of early neoplasia in oral tissue [79], lung [82], bladder [140] and smaller GI ducts [98]. Moreover, translational studies for first-in-human application of fluorescence molecular targets have been demonstrated in colonic dysplasia detection as well as surgical guidance for ovarian cancer [61] [141]. Compared to other optical contrast imaging techniques such as narrow band imaging and autofluorescence imaging, fluorescence molecular imaging with exogenous probes improves specificity for the detection of diseased tissues by targeting specific molecular entities such as overexpressed cell surface proteins at the cellular level [134] [135]. Meanwhile, due to the heterogeneity of disease molecular profile across individual patients, diagnostic sensitivity is expected to increase with the application of multiple molecular specific targeting using a panel of fluorescence probes [80] [85].

Many cancers are treatable by ablation or resection if detected at a very early stage. The problem in conventional white-light imaging is the lack of disease specific optical signatures to localize and visualize the pre-cancerous lesion [13]. Detection is further hindered by the diffuse and patchy nature of the lesions, which are often composed of distributed clusters of cells [80] [142]. This leads to one of the major challenges for the clinical realization of fluorescence molecular imaging, which is the requirement for high detection sensitivity *in vivo* to locate suspect tissue areas [143]

[72]. The sensitivity required for identifying small and sparse early cancerous lesions in routine endoscopic surveillance, as well as delineation of residue malignant cancer cells during surgical operations, is critical in reducing tumor occurrence and increasing survival rate. Thus increasing contrast in real-time intraoperative imaging has become a critical factor in the design and quality assurance of a fluorescence molecular imaging approach for translation to clinical diagnosis and therapy.

Detection sensitivity of an exogenous fluorophore probe is limited by three major factors: first, the characteristics of the molecular probe, such as probe-tissue binding affinity, non-specific binding and diffusion coefficient, as well as characteristics of the fluorophore such as quantum efficiency, absorption coefficient, fluorescence wavelength and photodegradation (also known as photobleaching) rates [110] [123] [144] [145] [146]. Second, the device performance and its detection sensitivity must be designed for each molecular target [72]. Last, the tissue autofluorescence (AF) background that degrades image contrast must be addressed [143].

For sensitive and specific early cancer targeting in clinical applications, many fluorescent molecular probes are currently under development [136] [147] [148]. These molecular probes target biomarkers indicative of early disease stages using antibodies or peptides, and are conjugated with a fluorescent indicator dye or nanoparticle. One of the best fluorophores for this purpose is fluorescein. In many respects this dye is preferable to near-infrared (NIR) dyes under development due to its status as a US Food and Drug Administration (FDA) approved dye with high molar absorptivity, fluorescence quantum yield exceeding 90%, good water solubility, and overall lower price when compared to NIR dyes [145] [118]. Meanwhile, significantly increased photo-stability and pH-independent quantum yield of fluorescein derivatives have been reported in recent publications [149] [150]. Methylene blue and ICG are Red-NIR dyes that are FDA approved for clinical use and take advantage of deeper light penetration at red-NIR illumination of 650 nm and 760 nm, respectively [151]. However fluorescein dye is not widely used even for

surface imaging applications, largely because it suffers from a low target-to-background ratio (T/B) which is caused by a high degree of tissue background autofluorescence (AF) that overlaps the dye emission in the green spectral range.

It has been reported that the tissue AF often masks exogenous molecular probe fluorescence signal, and thus limits the actual detection T/B *in vivo* [141] [152] [153] [154] [155] [156]. Other than fluorescein, a targeting probe sensitive to cellular glucose metabolism, 2-(N-(7-nitrobenz-2-oxa-1,3-diazol-4-yl)amino)-2-deoxyglucose (2-NBDG), a fluorescent analog to 2-deoxy-2 ((18)F) fluoro-D-glucose (FDG) which is routinely used in positron emission tomography (PET) for molecular imaging, and has been shown as a promising candidate in optical molecular imaging translatable from bench to bed [79] [157]. However, 2-NBDG also suffers from a significant masking effect from the background AF in the green spectral region [158] [159].

Recently, efforts have been directed at the advancement of molecular imaging devices by improving the fluorescence detection sensitivity of the imaging device through evaluations based on *in vitro* imaging of low concentrations of the targeting probe [160] [161]. However, in *in vivo* clinical applications, tissue background AF signal can exceed the device's detection sensitivity measured from the *in vitro* method, which renders meaningless engineering efforts to increase a device's detection sensitivity limit. Therefore, any device will be limited to the AF background, unless an approach to mitigate the AF can be implemented on the device. Meanwhile, understanding the quantitative spectroscopic characteristics of the targeted tissue's AF background is essential to the success of a viable fluorescence molecular imaging device. In the current study, we developed an approach to mitigate the AF background problem and apply this improvement to a high-sensitivity, ultrathin and flexible multispectral fluorescence endoscopic device.

For two specific fluorescence-guided clinical applications: endoscopic early cancer detection in Barrett's esophagus, and surgical brain tumor demarcation and resection, *ex vivo* porcine esophagus and wild type murine brain tissue were used to study the levels of background tissue autofluorescence. The porcine esophagus was chosen because its morphology, histology and biochemistry are similar to that of humans and therefore represents a good model for the human esophagus tissue [162]. Likewise, the wild-type mouse (nu/nu) was used as the healthy control of a patient-derived tumor xenograft mouse model of brain tumors. AF signals from the two types of tissue were quantitatively compared *ex vivo* with a gold standard quantitative imaging device, and transferred into a physical standard based on the exogenous molecular probe fluorophore concentration, defined as the Autofluorescence Equivalent Concentration (AEC). The detection sensitivity of the multispectral fluorescence endoscope was then evaluated in visible and near-infrared spectra using both the AEC and low concentration low volume fluorophore dilutions. Furthermore, based on quantitative evaluation of target tissue AF, a real-time AF mitigation algorithm was implemented, which significantly increased the T/B for a fluorescein conjugated molecular probe and 2-NGDB in a wide-field fluorescence imaging endoscope by 44 to 56 fold. Together, nanomolar sensitivity combined with a T/B ratio over 80 was achieved with the newly developed multispectral ultra-thin and flexible scanning fiber endoscope, and demonstrated in an *in vitro* study using molecular targets of high grade dysplasia and esophageal adenocarcinoma on a tissue phantom.

5.2 Materials and Methods

5.2.1 Multispectral SFE system

The new multispectral SFE system was specifically designed and engineered for wide field, high-resolution and real-time fluorescence molecular imaging and navigation [163]. Compared to a conventional endoscopic passive imaging system using diffuse white light illumination, the

multispectral SFE incorporates 3 low power diode lasers: 448, 488, and 642 nm (FiberTec™, Blue Sky Research, Milpitas, CA, USA) that can be jointly or selectively launched at the base station and sent to the distal end of the SFE scope via a single mode optical fiber using a custom optical fiber combiner (Wave Division Multiplexer, or WDM, Oz Optics, Ottawa, Ontario, Canada). The resulting multi-laser beam is scanned in a spiral pattern by a piezoelectric transducer and focused onto the target surface by a lens assembly. Fluorescence, or diffuse reflected light is then collected by a concentric ring of high numerical aperture optical fibers which surround the single mode beam delivery fiber and lens assembly. The collected light is separated into four wavelength bands (Blue, Green, Red fluorescence and Red reflectance respectively) by three dichroic beam splitters. Unwanted laser light is rejected by passing each wavelength band through a high optical density band-pass, or long-pass filter positioned in front of a high gain photomultiplier tube (PMT). Custom designed software maps the synchronized detection signals as points in the spiral scan pattern of the single mode fiber which are then converted to the 2-dimensional pixel position on the RGB digital display – red, green, and blue for fluorescence images and grayscale for reflectance. The resulting images are in spatial registration since all of the excitation lasers sample the same target location simultaneously.

For high sensitivity fluorescence detection, a new 2.1-mm outer diameter (OD) scope was designed and fabricated for the multispectral SFE system (**Figure 42** (a)). The light collection portion of the scope consists of a concentric ring of 6 identical, 500 micron diameter multimode plastic optical fibers (Mitsubishi Rayon Co., LTD, Tokyo, Japan). Since the collection numerical aperture remained high (NA = 0.6), it is estimated that the 2.1-mm scope has 20x the collection efficiency of the 1.2-mm diameter SFE scope due to the larger (20x) collection area of the fibers. [107].

5.2.2 SFE fluorescence sensitivity measurement

Sensitivity of the SFE was defined as the minimum amount of fluorescence measureable by the system. More specifically the system sensitivity was determined by the lowest concentration of fluorescent dye molecules that can be imaged with an S/N value greater than 2:1 when imaged at video rates (30 Hz). For the sensitivity measurement, the gains and offsets on the PMTs and digital display were kept constant at optimized values. The wide-field imaging angle and distance were also kept constant to guarantee reproducibility of the measurement.

Two fluorescent dyes for *in vivo* application, sodium fluorescein and cyanine (Cy5.5) were chosen for the sensitivity measurements. Dilutions of sodium fluorescein (Sigma-Aldrich, St. Louis, MO, USA) and Cy5.5 NHS ester (Lumiprobe, Florida, USA) were prepared in double distilled water (ddH2O) solutions. For making the dilutions of Cy5.5 NHS ester, the dye was first dissolved in DMSO as recommended by the manufacturer, and then serial dilutions were made using ddH2O. Dilutions covered the range from micromolar (μmol/L) to nanomolar (nmol/L) for both dyes, and were kept at pH7.

During the measurement, the SFE 488 nm laser was turned on for detection of sodium fluorescein in the Green channel, whereas the SFE 642 nm laser was turned on for the detection of Cy5.5 in the Red/NIR channel. All measurement were performed by imaging a 50μl dye droplet dispensed onto a diffuse, non-fluorescent and flat Teflon surface, with the SFE 2.1-mm scope pointing down perpendicularly to the Teflon surface at a 20-mm distance (**Figure 42** (b)). Imaging performance at video-rates (30Hz) was then evaluated.

As described earlier, high optical density (OD) filters (Semrock, Inc, Rochester, NY, USA) were employed to block light from the excitation laser sources at the PMT detectors. To verify that the background light from the excitation lasers was more than 10x below the measured fluorescence signals, images were recorded without any dyes placed on the non-fluorescent Teflon surface.

Figure 42. (a) The end-face of the new 2.1-mm SFE scope with six, 500 micron optical fibers held in a brass ring surrounding the distal lens for the scanned illumination. **(b)** Experimental setup for the fluorescence sensitivity measurement.

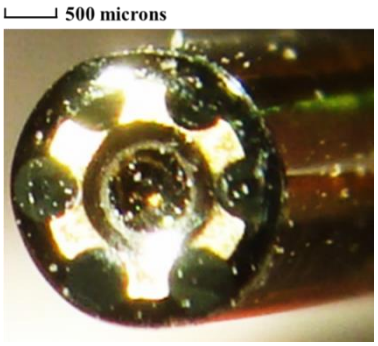

(a)

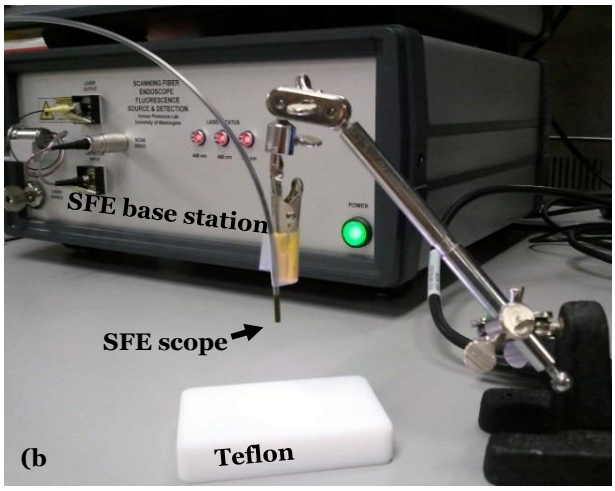

(b

5.2.3 Autofluorescence Equivalent Concentration (AEC) Measurement

The AEC was measured using the IVIS Spectrum Pre-clinical *In Vivo* Imaging System (PerkinElmer, Waltham, MA, USA). Two types of healthy *ex vivo* tissue samples: lower porcine esophagus epithelium and murine brain, were imaged respectively, with sodium fluorescein and Cy5.5 reference dye solutions placed alongside. The liquid dye solution reference was poured into the flat bottom of an off-the-shelf black phenolic screw-cap (16198-911 VWR, Visalia, CA, USA) to a depth of 5 mm.

All animal tissues were prepared under the protocols of the Institute of Animal Care and Use Committee-approval or Standard Operating Procedure for porcine tissue from abattoirs by the University of Washington.

Brains were freshly harvested from a group (n=5) of wild-type nude (nu/nu) mice (same sex, age and weight). Meanwhile, porcine esophagus tissue of the same age and weight group (n=5) were obtained from a certified abattoir. The lower 1/3 of esophagus was cut open and placed flat on a

glass surface (chamber slide, Fisher Scientific, Hampton, NH) with the epithelium layer facing up for imaging.

To get a full assessment of the autofluorescence excitation-emission profile of the tissues, a wide range of excitation (430 nm-745 nm) and emission (500 nm-840 nm) filter combinations were employed with the IVIS Spectrum (Perkin-Elmer, Norwalk, CT) fluorescence imaging system. During the imaging process, system settings such as exposure time, f-number, and field-of-view were kept constant. The IVIS quantitative unit of the fluorescence emission intensity is defined as photons per second per centimeter squared per steradian ($p/s/cm^2/sr$). Quantitative fluorescence emission intensities were analyzed off-line on the recorded images, and averaged across the same tissue type group.

5.2.4 Orthotopic Mouse Brain Tumor Models

Orthotopic xenograft models were created by implanting $1x10^5$ tumor cells in suspension through a 1mm bur hole in the right parietal bone above the cerebellum approximately 2mm posterior to the bregma and 3mm beneath the dura. This study used pediatric patient derived medulloblastoma model MED-211FH. Tumor cells came from donor mice bearing symptomatic intracranial tumors and were transplanted directly into male and female NSG mice. Tumors were allowed to grow until mice presented with clinical symptoms of tumor burden such as head tilt and cranial bulge, 35 days for the MED-211FH model. At first onset of clinical tumor burden, mice were given 100ul intravenous tail-vein injections of 20uM chlorotoxin conjugated to Cy5.5 (Tumor Paint™, Blaze Biosciences, Seattle, WA, USA) and imaged in the near-infrared spectrum as previously described [139]. Brains were harvested after euthanasia via CO_2 inhalations, imaged, and then fixed in 10% neutral buffered formalin. All mice were maintained in accordance with

the NIH Guide for the Care and Use of Experimental Animals with approval from the Fred Hutchinson Cancer Research Center Institutional Animal Care and Use Committee (IR#1457).

5.2.5 Multispectral molecular Imaging of *ex vivo* mice brain

The SFE fluorescence molecular imaging was performed on the *ex vivo* mice brain within 1 hour after they were harvested. Images of the same brain using the IVIS Spectrum system immediately after harvesting were used as a reference. Images of the bulk fluorescently-labeled tumor margin from both imaging systems were compared. To guarantee a fair comparison of molecular probe distribution, experimental settings, such as the excitation and emission wavelength on both imaging systems, as well as imaging angle and exposure time, were kept as closely matched as possible. Three types of control brains: wild-type mice alone, wild-type mice with Tumor Paint™ injection, and MED-211FH mice with no injection were also imaged. After the imaging were performed, brains were fixed in 10% neutral buffered formalin, then, tissue blocks were embedded in paraffin, cut into 4-um sections, and stained with hematoxylin and eosin (H&E) using standard methods. Slides were scanned on an Aperio ScanScope AT (Leica Biosystems Buffalo Grove, IL).

5.2.6 BE tissue phantom model

Details of the biological phantom design and development can be found in [164]. Briefly, bovine collagen (Sigma Aldrich, St. Louis, MO, USA) was digested using collagenase (Life Technologies, Carlsbad, CA, USA) and reconstituted into a solid gel to serve as the AF background. Rat tail collagen gels (Life Technologies, Carlsbad, CA, USA) were seeded with CP-D (American Type Culture Collection, Manassas, VA, USA), a HGD Barrett's Esophagus cell line. Cultures were fixed in methanol. Overexpression of EGFR, ERBB2, and C-MET were identified through indirect immunofluorescence (IF) staining. The IF staining was performed using goat Alexa Fluor 488

(Life Technologies, Carlsbad, CA, USA) conjugated antibodies to target anti-ERBB2, anti-EGFR and anti-C-MET. The seeded gels were laid upon the solid collagen background for imaging.

5.2.7 Multispectral molecular endoscopic imaging with AF mitigation

Multispectral SFE imaging of the BE tissue phantom was performed with an AF mitigation algorithm running in real-time, to achieve a high target-to-background ratio (T/B) as well as to eliminate bleed-through specular reflections. A graphical illustration of the algorithm is shown in **Figure 43**. Since higher laser powers were desired for the *in vitro* testing, the multispectral fluorescence was excited using a Coherent OBIS Galaxy system with FP lasers [165] at 445, 488, and 642 nm which proved to be plug-and-play simplicity across the spectrum with the single-mode optical fiber coupling to the SFE [166]. The implementation employs simultaneous excitation by two closely spaced laser wavelengths: 488 nm as the targeting beam and 445 nm as the AF reference beam. Fluorescence in the Blue channel is dedicated to the AF emission, whereas the Green channel contains a mixture of fluorescein and AF background emission. Based on the AF signal from the concurrent Blue channel and a pre-calibrated ratio, the AF component in the Green channel background AF is subtracted in real-time within the SFE operating system software. As a result, an increase in fluorescein T/B is achieved.

Figure 43. Graphical illustration of the real-time AF mitigation algorithm on the multispectral SFE system for fluorescein fluorescence imaging.

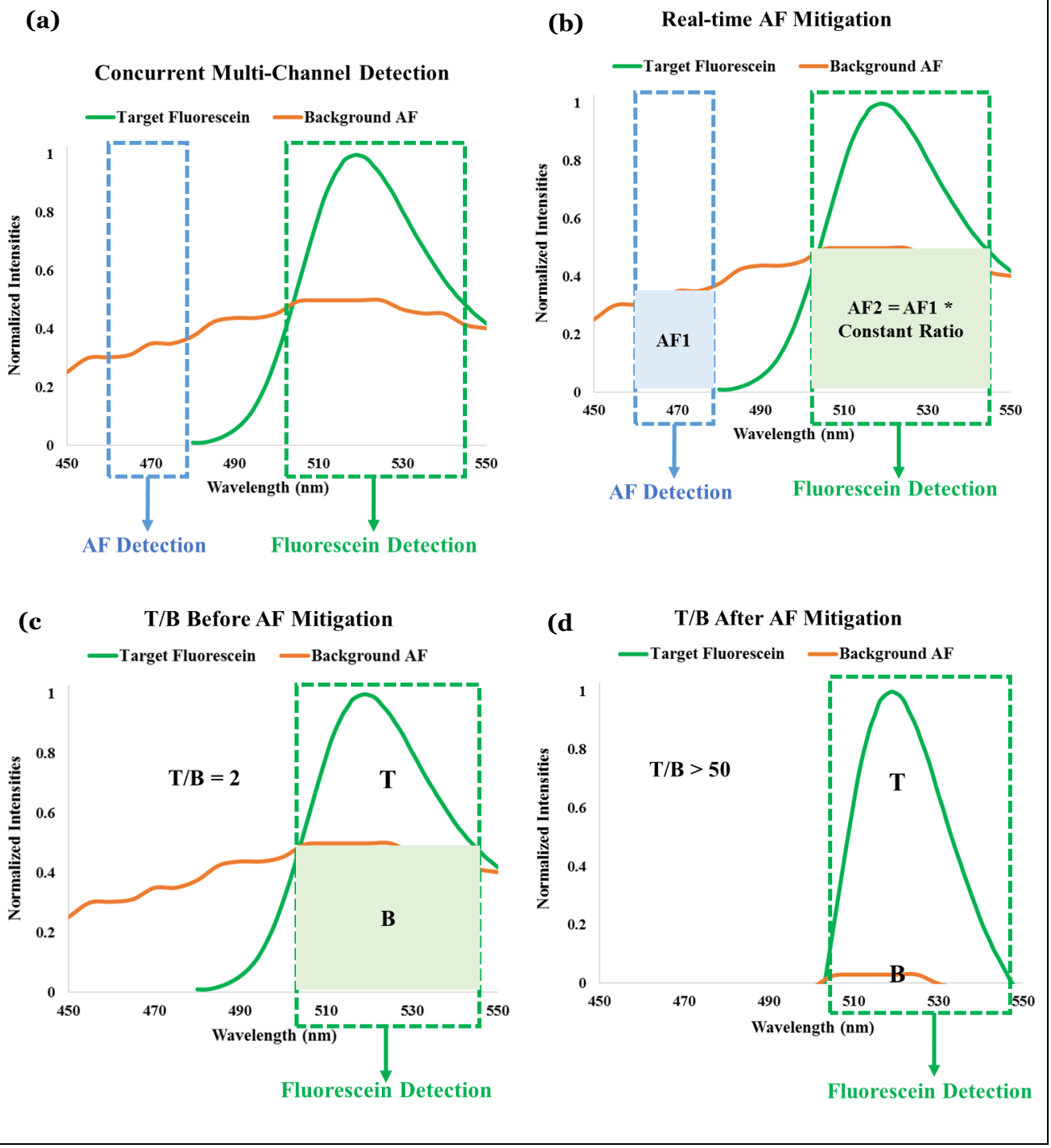

5.3 Results

5.3.1 Multispectral Scanning Fiber Endoscope (SFE) system

The new multispectral SFE (shown in **Figure 44** (a), (b) and (c)) was custom-fabricated for the purpose of fluorescence molecular endoscopy. Under standard operating conditions, the video imaging system has a 30 Hz refresh rate, with an 80 degree field-of-view, 50 microns image resolution and a depth-of-focus from 2 to 50mm. Three fluorescence channels and one reflectance channel are simultaneously processed to create spatially co-registered blue, green, red fluorescence and a grayscale reflectance background images. All of the images are inherently coincident by virtue of the simultaneous laser scanning and light collection design of the SFE. Concurrent, wide-filed and high-resolution imaging was demonstrated on all channels for the multispectral SFE, with an intraoperative navigation feature derived from the gray scale reflectance background. The system also operates with quantitative fluorescence imaging to guide biopsies based on a previously published Distance Compensation algorithm [67].

Figure 44. Real-time, high-sensitive and concurrent multispectral fluorescence Scanning Fiber Endoscope (SFE) system with a 2.1-mm endoscope. (a). System in operation. (b). Ultrathin endoscope. (c). Concurrent multi-channel fluorescence separation and detections.

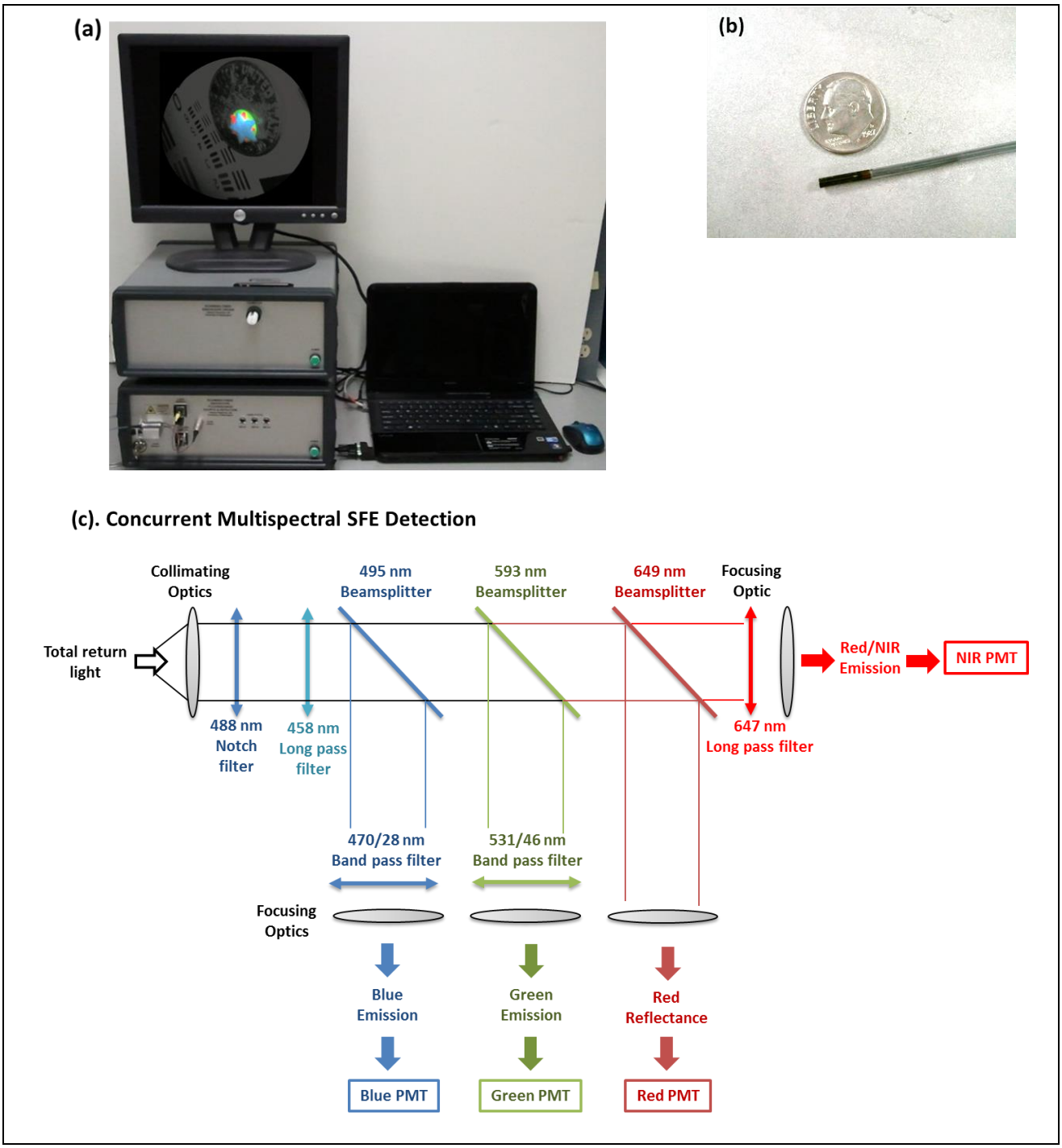

5.3.2 Imaging Device Detection Sensitivity

The detection sensitivity of the SFE was evaluated on a series of low-volume (50uL) and low-concentration (nanomolar to micromolar) fluorophore dilutions. In the current study, sodium

fluorescein and Cy5.5 dyes were chosen for the sensitivity test, since they were to be used in the following *ex vivo* or *in vitro* image applications. The SFE output powers were less than 3 mW for each channel and maintained constant for the experiments.

The multispectral SFE detection sensitivity limit was 5 nanomolar for the sodium fluorescein dye and 10 nanomolar for the Cy5.5 dye at video rates with a signal-noise-ratio (SNR) of 2:1. The SFE detection channels' linearity was previously demonstrated over the 0 – 100 micromolar range [167], the same method was also used here, by plotting the dye concentration versus image intensity relationship to confirm the detection channel linearity over the 0 – 100 nanomolar range (**Figure 45**).

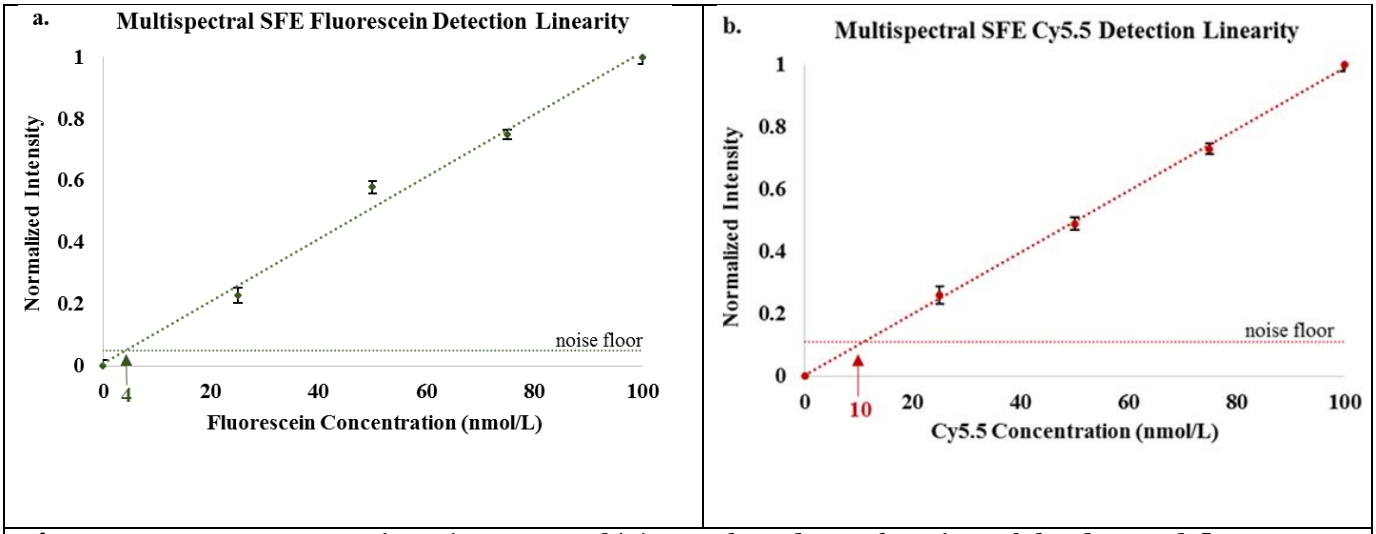

Figure 45. Dye concentrations (0-100 nmol/L) are plotted as a function of the detected fluorescence signals in the SFE images. Each data point was an average of n=5, and the error bars represent the variability in the fluorescence signal intensity measurement. The linearity of the sodium fluorescein fluorescence in the SFE's Green channel is presented in **(a)**, whereas in **(b)** the linearity of the Cy5.5 fluorescence in the SFE's Red detection channel is shown.

5.3.3 Autofluorescence Equivalent Concentration (AEC) – the brain and the esophagus

The AEC was determined in a side-by-side comparison of the fluorescence intensity from a sodium fluorescein or Cy5.5 dye standard with the intensity from the fresh *ex vivo* brain and esophagus tissue sample. Quantitative fluorescence imaging was performed with the IVIS Spectrum system and the recorded images were analyzed off-line. To avoid photodegradation, all the samples were kept in a dark container before moving into the IVIS's sample chamber, and the images were taken within 10 seconds after the samples were exposed to room light. No dye loss from the IVIS imaging light exposure (exposure time: 1 second) was observed.

For defining the AEC of sodium fluorescein dye in the esophagus epithelium and brain tissue, the IVIS bandpass excitation filter at 460/(±15) nm was chosen as a close match to the SFE's 488 (fluorescein) excitation laser, and the IVIS 520/(±10) nm bandpass fluorescence detection filter was selected as the corresponding emssion wavelength. Likewise, the AEC of Cy5.5 dye was defined by imaging the same esophgeal and brain tissue under the IVIS excitation filter at 640/(±15) nm corresponding to the SFE's 642 nm excitation laser, and the IVIS emission filter at 700/(±10) nm was used to collect the fluorescence signal.

As shown in **Figure 46**, at 460/(±15) nm excitation, the 10 nanomlar (nM) concentration of fluorescein was found to be equivalent to the esophagus epithelium tissue group in fluorescence/AF emission intensity (**Figure 46**, a), whereas the AF emission intensity from the brain tissue group was 5x lower compared to the same sodium fluorescein sample (**Figure 46**, b). Therefore, at 460/(±15) nm excitation the sodium fluorescein AEC in porcine esophagus was 10 nM and 2 nM for mice brain. Meanwhile, at 640/(±15) nm excitation, the AF from the esophagus was 5x lower compared to the emission from a 10 nM Cy5.5 dye, and the brain AF signal was 1/5 the emission signal from the same Cy5.5 dye standard. Therefore, at 640/(±15) nm

excitation the AEC for porcine esophagus epithelium tissue was 2 nM for Cy5.5, and 1 nM for mice brain tissue .

Figure 46. Autofluorescence Equivalent Concentration (AEC) evaluation using the IVIS spectrum. (a) and **(b).** Side-by-side quantitative fluorescence intensity comparison of 10 nM fluorescein sodium solution, healthy porcine esophagus tissue and wild mice brain under the IVIS spectrum imaging. Excitation filter 460/(±15) nm was used, and emission was gathered by the 520/(±10) nm filter. **(c)** and **(d).** Side-by-side comparison with the exact same *ex vivo* tissue samples, and 10 nM Cy5.5 solution under the IVIS. In this case, 640/(±15) nm was used for the excitation and 700/(±10) for the emission. Settings on the IVIS spectrum (e.g., exposure time, f-number, and field-of-view, etc.) were kept constant. The quantitative unit of the fluorescence emission intensity is defined as photons per second per centimeter squared per steradian (p/s/cm2/sr). Since this is an absolute quantification unit, quantified fluorescence intensities can be compared using the same absoute quantification unit.

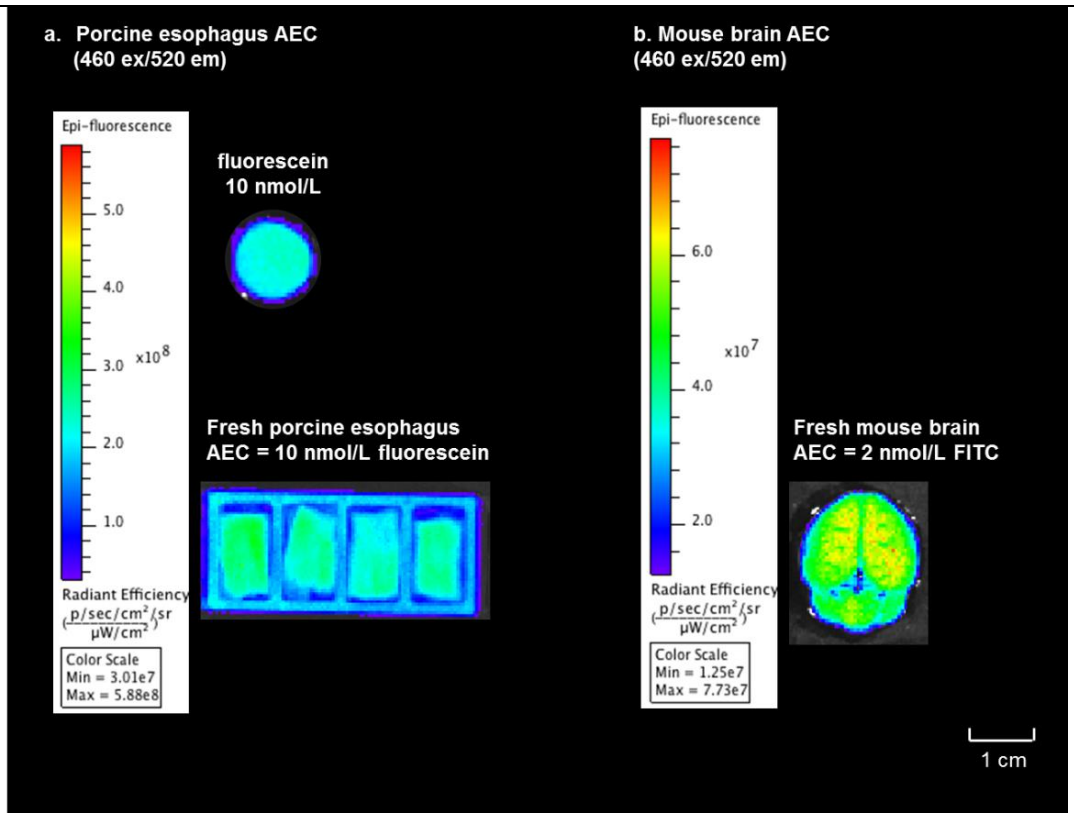
a. Porcine esophagus AEC
(460 ex/520 em)
Epi-fluorescence
5.0
4.0
3.0
x10^8
2.0
1.0
Radiant Efficiency
(p/sec/cm²/sr)/(μW/cm²)
Color Scale
Min = 3.01e7
Max = 5.88e8
fluorescein
10 nmol/L
Fresh porcine esophagus
AEC = 10 nmol/L fluorescein
b. Mouse brain AEC
(460 ex/520 em)
Epi-fluorescence
6.0
x10^7
4.0
2.0
Radiant Efficiency
(p/sec/cm²/sr)/(μW/cm²)
Color Scale
Min = 1.25e7
Max = 7.73e7
Fresh mouse brain
AEC = 2 nmol/L FITC
1 cm

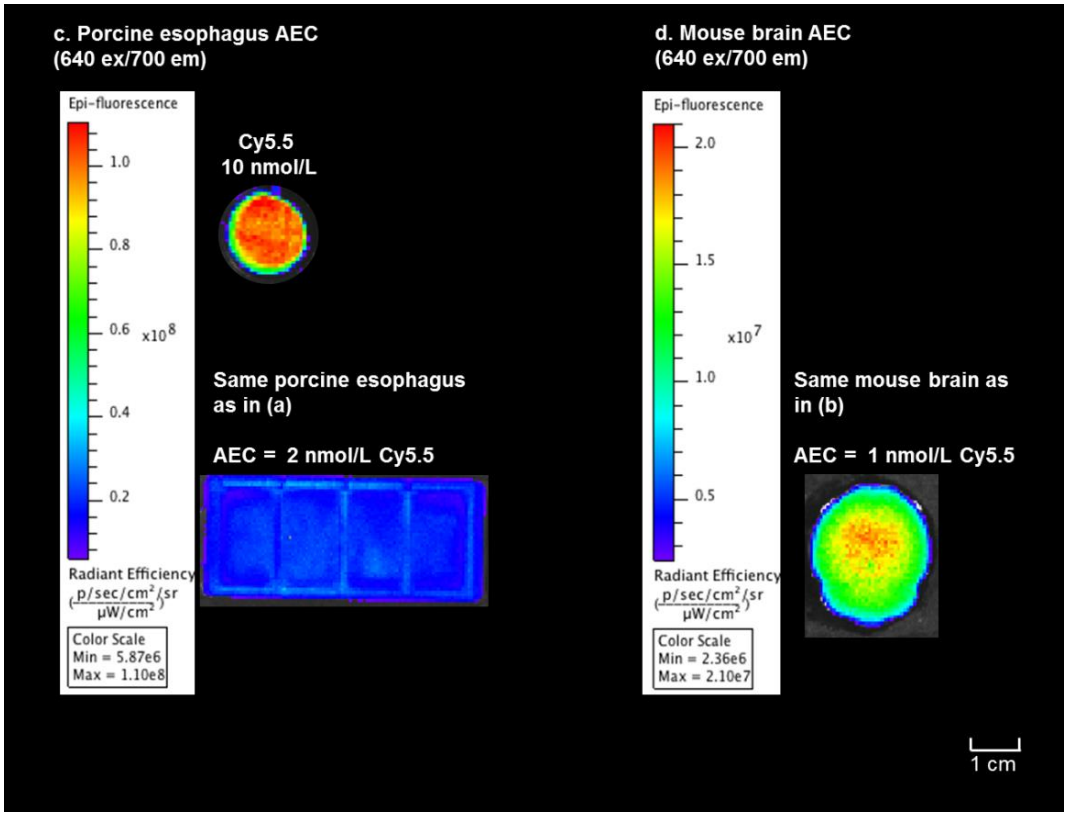
c. Porcine esophagus AEC
(640 ex/700 em)
Epi-fluorescence
1.0
0.8
0.6
x10^8
0.4
0.2
Radiant Efficiency
(p/sec/cm²/sr)/(μW/cm²)
Color Scale
Min = 5.87e6
Max = 1.10e8
Cy5.5
10 nmol/L
Same porcine esophagus
as in (a)
AEC = 2 nmol/L Cy5.5
d. Mouse brain AEC
(640 ex/700 em)
Epi-fluorescence
2.0
1.5
x10^7
1.0
0.5
Radiant Efficiency
(p/sec/cm²/sr)/(μW/cm²)
Color Scale
Min = 2.36e6
Max = 2.10e7
Same mouse brain as
in (b)
AEC = 1 nmol/L Cy5.5
1 cm

5.3.4 Quantitative Autofluorescence (AF) Analysis of *ex vivo* esophagus and brain

For quantitative understanding and comparison of the AF emission pattern across the visible to infrared spectrum, tissue autofluorescence of the esophagus and brain tissue were captured separately with all of the available IVIS Spectrum's excitation-emission filter combinations. The relative AF amplitudes for porcine esophagus epithelium and mouse brain, respectively, are plotted in **Figure 47** (a) and (b) under excitation from 430 to 675 nm and emission across a range of 500-820 nm. As shown in the graphs, the AF emission intensity for both tissue types peaked at around 500-520 nm, with maximum excitation at the shorter wavelengths (430-465 nm). For a fixed excitation, the AF emission signal declined when moving from short to longer wavelength, and reduced by 10x when moving beyond 800 nm. Meanwhile, the AF emission also decreased when the excitation wavelength shifted from 430 to longer wavelength. However, even with the intensity decline, the AF emission signal remained detectable (>10% peak intensity) in the 600 – 800 nm range from both tissue types.

Figure 47. Quantitative AF analysis of esophagus epithelium and brain tissue under a wide range of excitations from 430 nm to 675 nm.

(a).

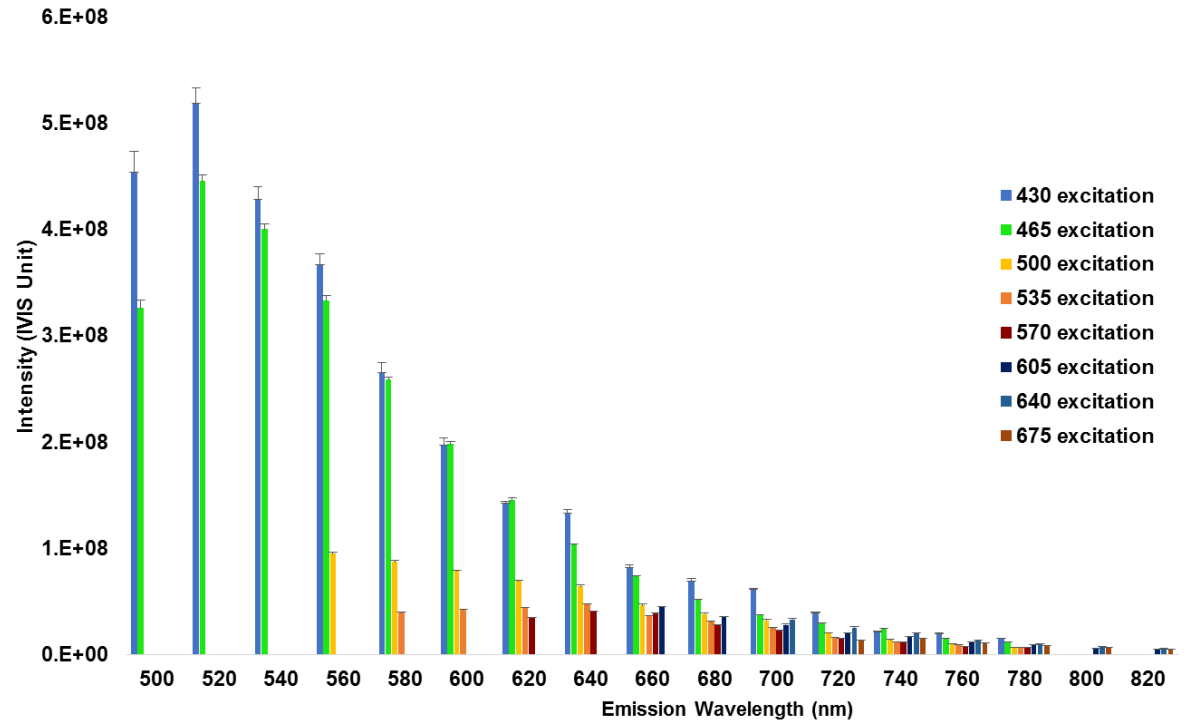
Quantitative AF Intensities under Visible - NIR Excitations in Esophagus Epithelium
6.E+08
5.E+08
4.E+08
3.E+08
2.E+08
1.E+08
0.E+00
Intensity (IVIS Unit)
500 520 540 560 580 600 620 640 660 680 700 720 740 760 780 800 820
Emission Wavelength (nm)
430 excitation
465 excitation
500 excitation
535 excitation
570 excitation
605 excitation
640 excitation
675 excitation

(b).

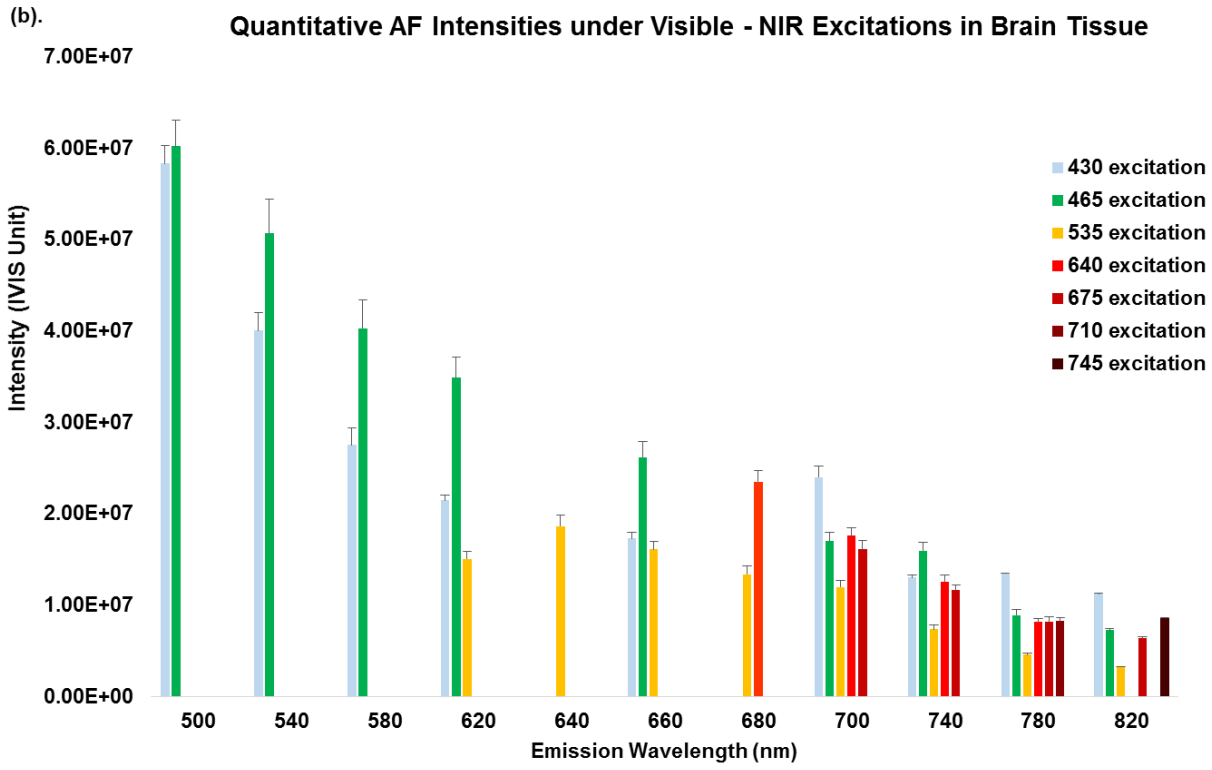
Quantitative AF Intensities under Visible - NIR Excitations in Brain Tissue
7.00E+07
6.00E+07
5.00E+07
4.00E+07
3.00E+07
2.00E+07
1.00E+07
0.00E+00
Intensity (IVIS Unit)
500 540 580 620 640 660 680 700 740 780 820
Emission Wavelength (nm)
430 excitation
465 excitation
535 excitation
640 excitation
675 excitation
710 excitation
745 excitation

Figure 48 represents the AF emission spectral profiles from the esophagus (**Figure 48**(a)) and the brain (**Figure 48**(b)) for different excitation wavelengths. Each excitation spectral profile was derived from the IVIS AF signal intensities with a scaling factor. This factor is the ratio of the maximum AF intensity measured at 430 nm divided by the maximum AF intensity of the particular excitation data series being plotted. The scaling factors are also shown on the graph alongside the assigned spectral profiles.

Figure 48. Autofluorescence Excitation and Emission Spectral Characteristics of porcine esophagus and murine brain tissue.

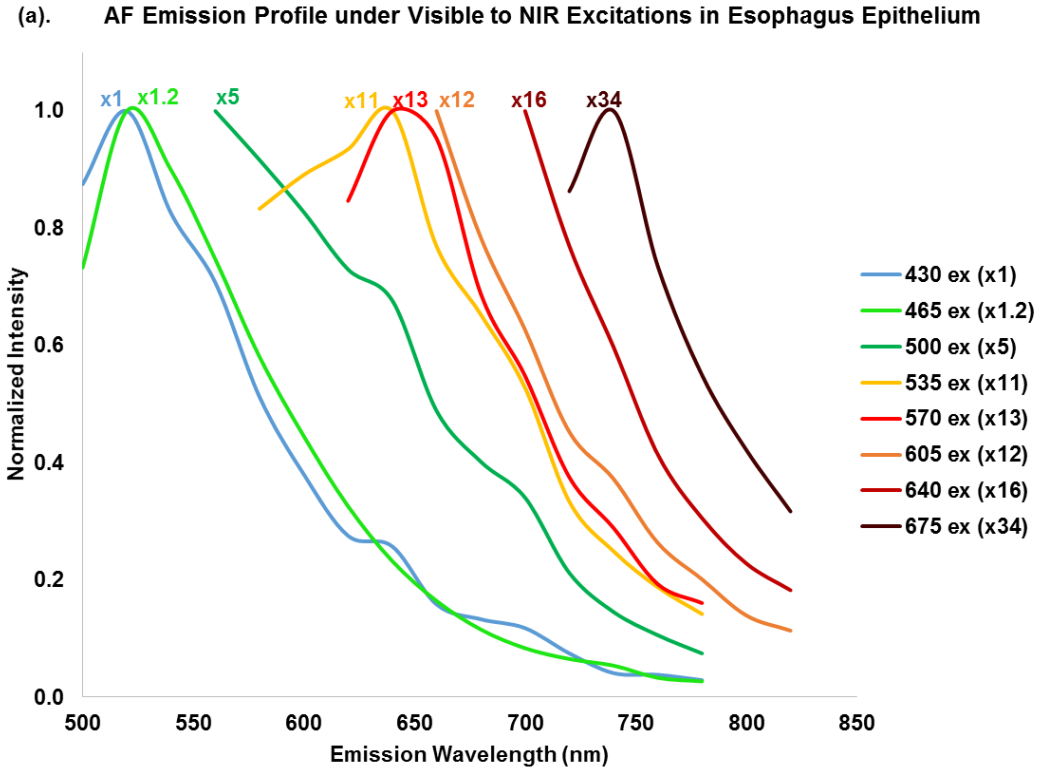

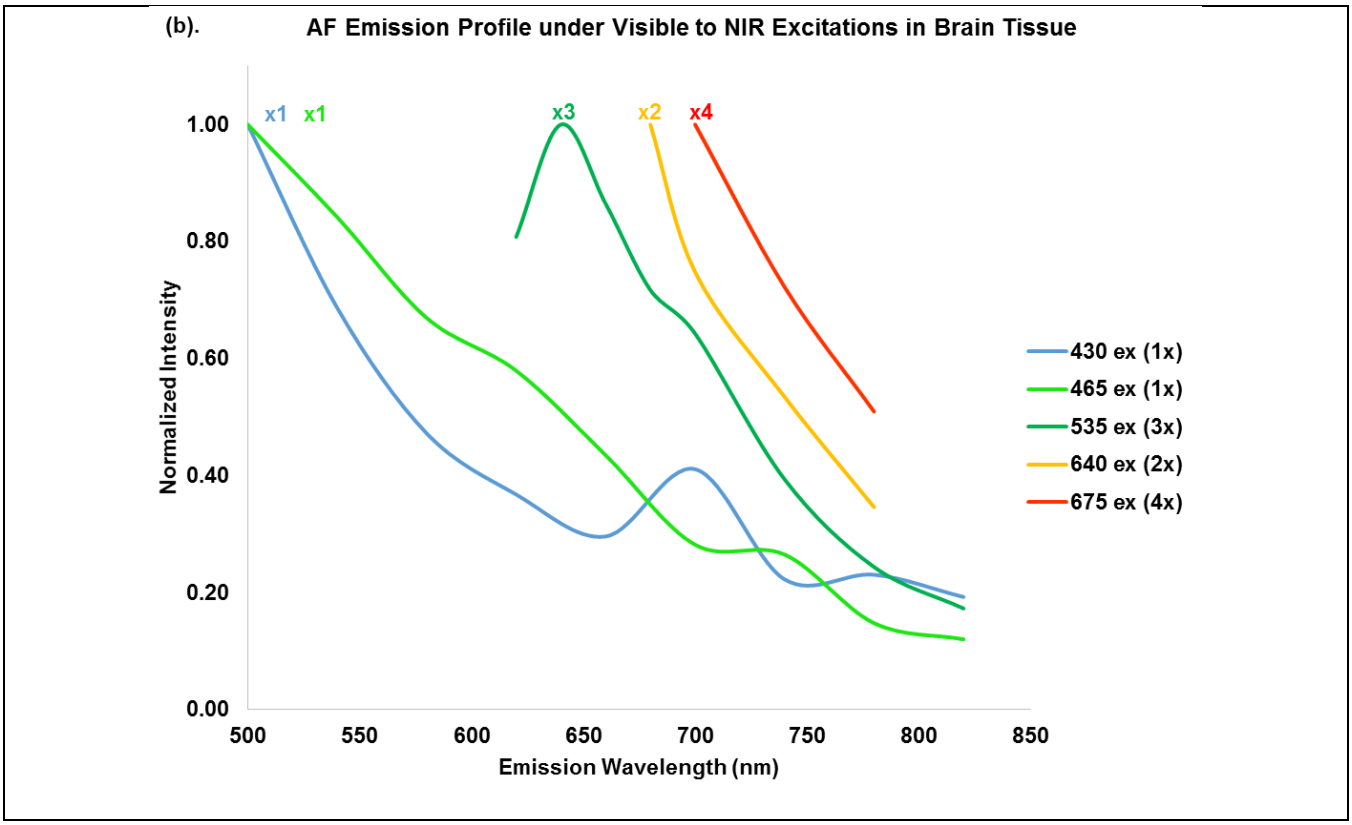

A red-shift phenomenon was observed in all of the normalized AF spectral profiles plotted in **Figure 48**. Specifically, each emission profile/shape remained nearly the same, whereas the peak spectral wavelength was red-shifted from 500 to 750 nm as the excitation wavelength changed from 430 to 675 nm. Interestingly, both tissue types exhibited similar emission profiles and peak spectral intensities under 430 nm and 465 nm excitation.

The scaling factors indicated that the emission intensity decreased as the excitation wavelength changed from the visible to NIR, but AF signal was still detectable in the NIR range. For the esophagus epithelium tissue, the AF signal dropped by a factor of 5x at 500 nm excitation compared to the peak excitation at 430 nm, and continued to decrease by a factor of 10x at 550 nm excitation, and eventually by 34x at 675 nm excitation. However, the AF decline for the brain tissue was much slower, with only a 4x decrease at 675 nm excitation compared to the peak excitation at 430 nm.

5.3.5 Molecular imaging of brain tumor detection

Highly sensitive SFE molecular imaging was demonstrated on *ex vivo* mice brain tissue with xenograft human-derived tumor. Details regarding the Tumor Paint™ molecular imaging probe can be found in previous publications [139]. Eight hours following tail vein injection of 0.1 mL 20 micromolar CTX: Cy5.5 conjugate, a side-by-side comparison between IVIS and SFE quantitative molecular imaging was conducted.

As shown in **Figure 49**(a) (b), there was no observation of specific Tumor Paint (TP) accumulation using the IVIS and SFE imaging systems for the wild-type mice with TP injection. On the other hand, in **Figure 49**(c), for the xenograft tumor mice with TP injection, a mass accumulation of the molecular target was observed, and the resultant tumor margin was confirmed from the IVIS, SFE, and H&E images on all the tumor mice brains. Images from different devices (IVIS and SFE), or different methodology (imaging or H&E pathology stain) consistently indicated that this type of tumor xenograft demonstrated a diffuse pattern and is located beneath the tissue surface. Isolated red spots in the SFE images correspond to specular reflections from the tissue surface.

Quantitative image analysis showed that the target-to-background ratio (T/B) for SFE real-time imaging was on average 2.3, whereas the T/B for IVIS was about 2.1. Images from the wild type mice without TP injection suggested that the background signal was mostly contributed by tissue autofluorescence.

Figure 49. Tumor paint (CTX:Cy5.5) imaging of mouse xenograft tumor.

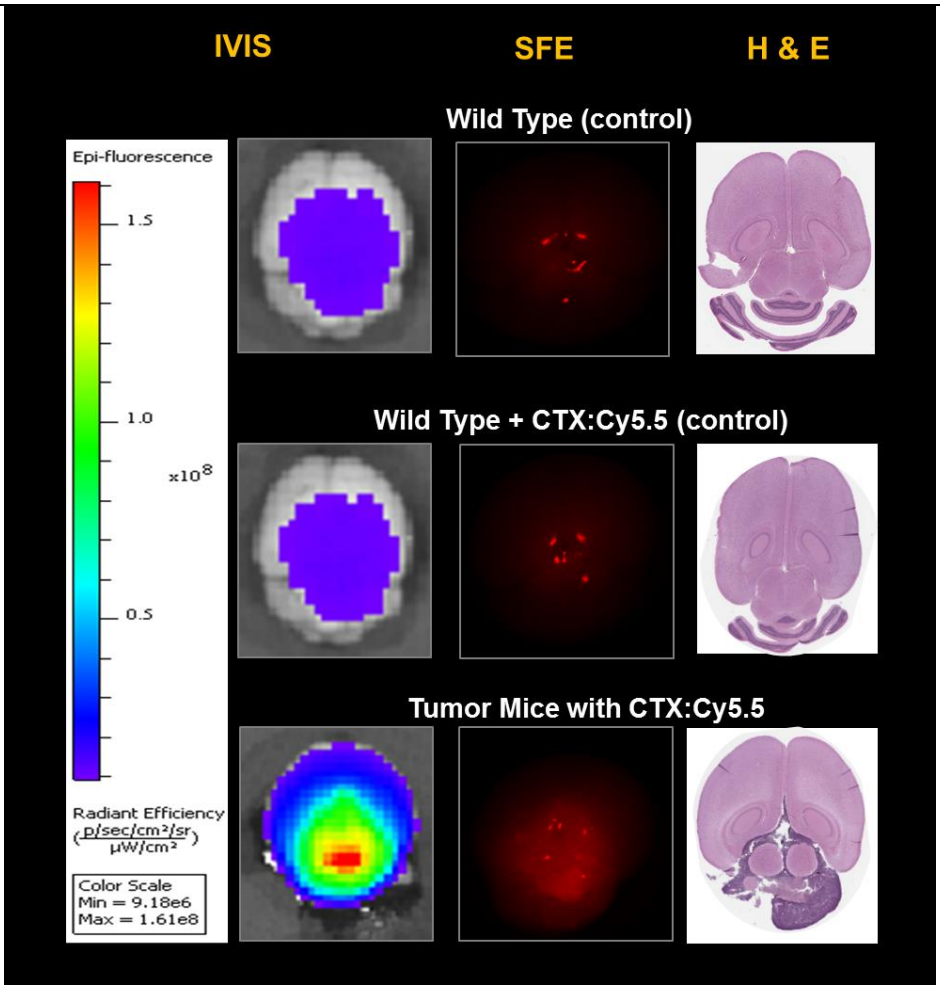

5.3.6 Real-time AF and specular reflection mitigation on a tissue phantom

A real-time AF mitigation algorithm was implemented in the software operating system of the multispectral SFE. To demonstrate the performance of the algorithm, a tissue phantom was designed and constructed to simulate the 3-dimensional anatomical structure of the gastrointestinal tract. Specifically, the tissue phantom featured a mucosal Barrett's esophagus (BE) with monolayer high-grade dysplasia (HGD) and Esophageal Adenocarcinoma (EAC) cell, as well as a submucosal collagen matrix which is known to be a major contributor to the background AF signal [168]. FITC conjugated molecular probes targeting cancer specific proteomic biomarkers

(EGFR, HER2, and CypA) were applied to the phantom, as well as metabolic molecular probe 2-NBDG, respectively, to demonstrate the AF and specular reflection mitigation algorithm.

As described previously, 445 nm and 488 nm laser beams were launched simultaneously into the SFE scanning fiber as excitation light sources each producing 7 mW outputs on the tissue. The 445 nm excitation served as the reference beam to excite the tissue AF, whereas the 488 nm excitation targeted the fluorescein molecular markers. Traditionally, in the target detection channel, the fluorescence signal would contain unavoidable AF background signal which reduces the T/B. However, with the algorithm running in real-time, AF excited via the 445 nm excitation and received in the SFE Blue detection channel is proportional to the quantity of background AF signal in the concurrent target fluorescein/Green channel. Therefore, AF mitigation can be achieved by subtracting the background AF signal in the Green channel by a pre-determined factor of the concurrent AF signal in the Blue channel. The algorithm runs automatically on a pixel-by-pixel basis at high resolution (50 microns), and at real-time video rates (30 Hz).

Furthermore, an additional benefit of the AF mitigation algorithm was realized with multiple fluorescence imaging channels. Specular bleed-through artifacts in the fluorescein/Green channel were also subtracted based on the signals from the AF/Blue channel, at the same pixel location, as all the detection channels of the SFE system are spatially co-registered.

The results shown in **Figure 50**(b) demonstrated the significant improvement of T/B and elimination of specular reflection after applying the AF mitigation algorithm. Specifically, the T/B ratio increased from 2.1 to 117.7 – a 56 fold improvement, and the specular reflection from **Figure 50**(a) was removed, resulting in a clean and clear delineation of the targeted disease region. The same algorithm also was applied to a lumen-shaped tissue phantom with AF background and a 2-NBDG target (**Figure 51**). Significant T/B 44-fold enhancement from 2.1 to 88.0 was also observed.

Figure 50. Real-time AF and specular reflection mitigation on a flat tissue phantom with molecular specific labeling using fluorescein isocyanine conjugated probes.

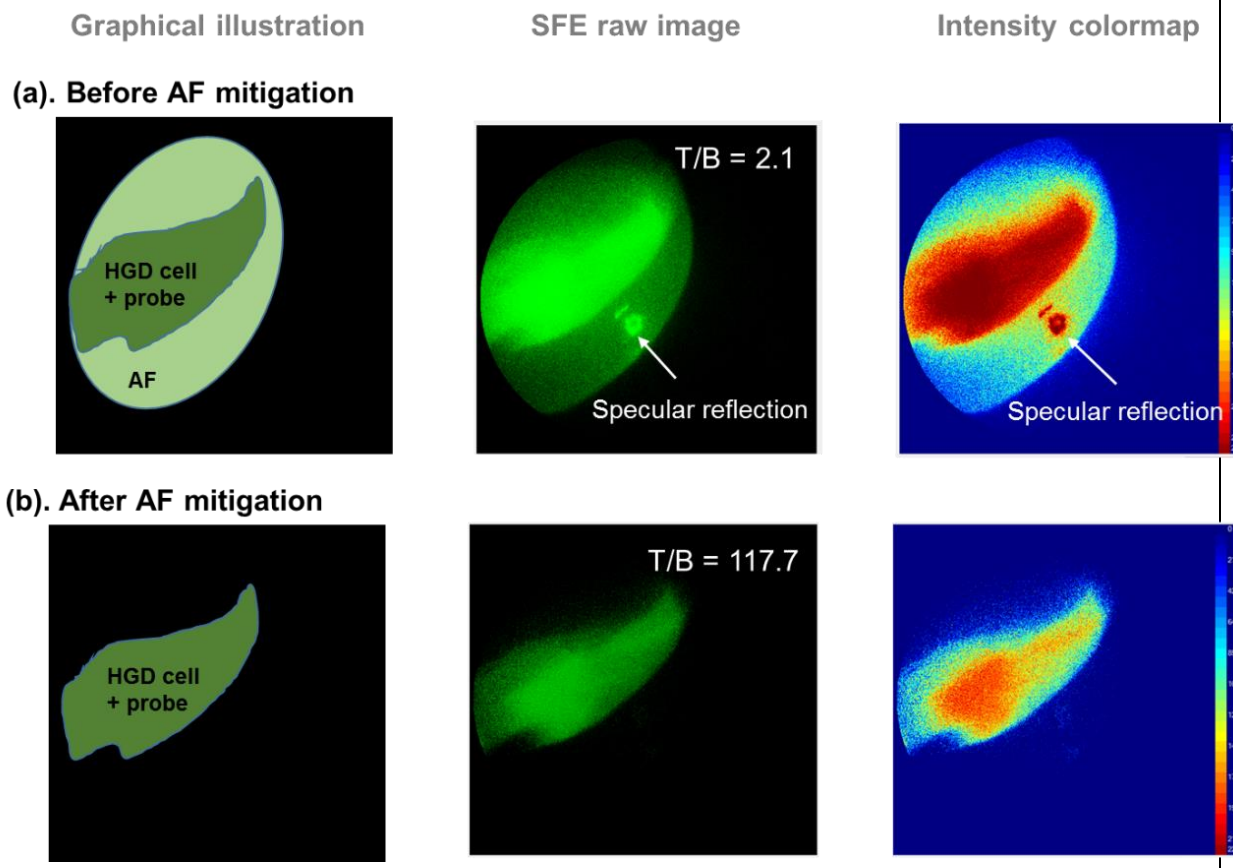

Figure 51. Real-time AF mitigation on a lumen-shaped tissue phantom with a 2-NBDG target.

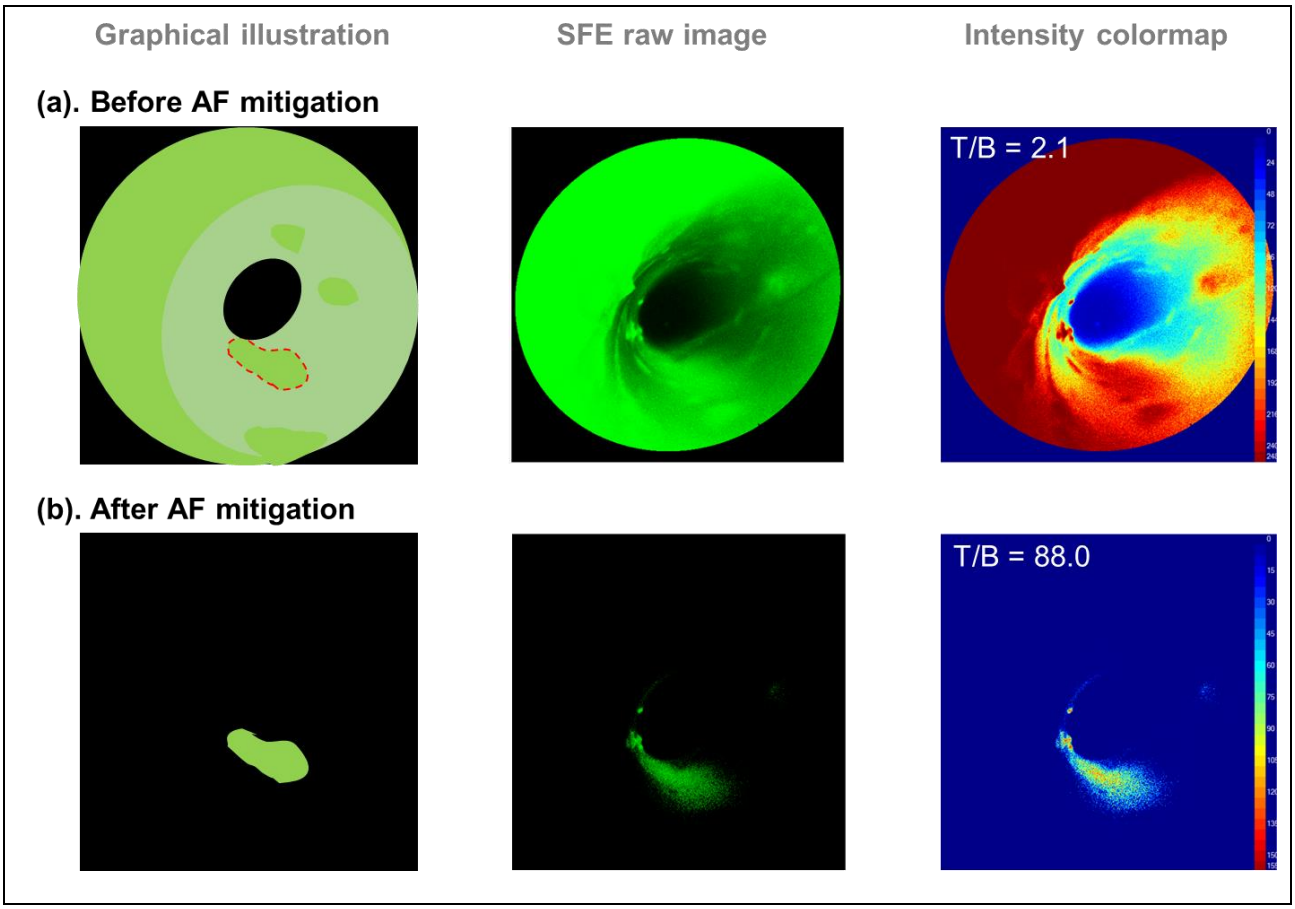

5.4 Discussion

High sensitivity at nanomolar fluorophore levels is needed for a viable fluorescence molecular endoscopic imaging device to detect disease associated cellular biomarkers and guide interventions. Apart from achieving a high signal-to-noise ratio (SNR) as an electronic device, the success of a clinically-viable molecular diagnostic imaging system also depends on the *in vivo* image contrast ratio (T/B). However, low T/B (≤3) is often reported and caused by a combination of confounding factors including the abundant tissue background autofluorescence (AF) [139] [98] [61] [141] [80] [155] [156]. Sometimes, the background AF signal can be as high as the target signal.

It blocks out diagnostic information, and reduces the net sensitivity of the molecular probe imaging.

It is a general concern that tissue AF is a major limiting factor for achieving high contrast ratio in exogenous fluorophore probe imaging. Although quantitative dilutions of the target fluorophore are routinely used for evaluating an imaging device's detection capability, the quantitative signal strength of the background AF and its amplitude compared to the target signal are often unaddressed. The omission of this AF interference impedes the evaluation of the imaging device's *in vivo* detection capability. In the present study, we established the AEC as an additional requirement for fluorescence molecular imaging device evaluation, and performed the AEC measurement of targeted tissues with references to a quantitative fluorescence *in vivo* imaging instrument – the IVIS Spectrum. The AEC method enables researchers to prepare portable calibration standards without the need for complex radiometric measurement systems

We propose and demonstrate herein a two-step method for evaluating a fluorescence molecular imaging device's detection sensitivity. The evaluation method is based on two major factors: **(1)** determine the signal-to-noise ratio (SNR) of the device itself *in vitro* using low concentrations of fluorophore dye probes, and **(2)** evaluate the actual target-to-background ratio (T/B) in the presence of tissue background autofluorescence (AF). Here, the AF signal is quantitatively assessed and transferred into the AEC of standardized fluorophore solutions. The fluorophore reference concentrations are determined in a side-by-side comparison with the quantitative tissue AF signal. The fluorophore concentration that quantitatively matches the AF background (**Figure 46**) is then selected as the portable AEC standard. .

The quantitative AF measured from healthy esophagus and brain tissue also revealed the heterogeneity of AF signals among different animal species and tissue/organ types. For instance, as shown in **Figure 52** (a), under blue (460±15 nm) excitation, the AF emission from the

esophagus is significantly higher than that of the brain; on the other hand, under NIR (640±15 nm) excitation, the difference between the background AF signals was much less significant (**Figure 52** (b)). Also represented in the scaling factors in **Figure 48** (a), from blue to NIR excitations, the decline of peak esophagus AF signal is much faster than the decline of peak brain AF. This quantitative assessment led to the estimate of background AF's presence in brain tissue even using red/NIR dyes. In fact, background AF was recognized in molecular endoscopic imaging of the xenograft mice tumor model using the Cy5.5 TP probe (**Figure 49**, wild-type control mice, 640±15 nm excitation). This result concurred with previous publications that background AF signals were present and detectable even beyond the visible spectrum [77].

Figure 52. AF comparison the esophagus versus the brain (at 460 nm excitation and 640 nm excitation).

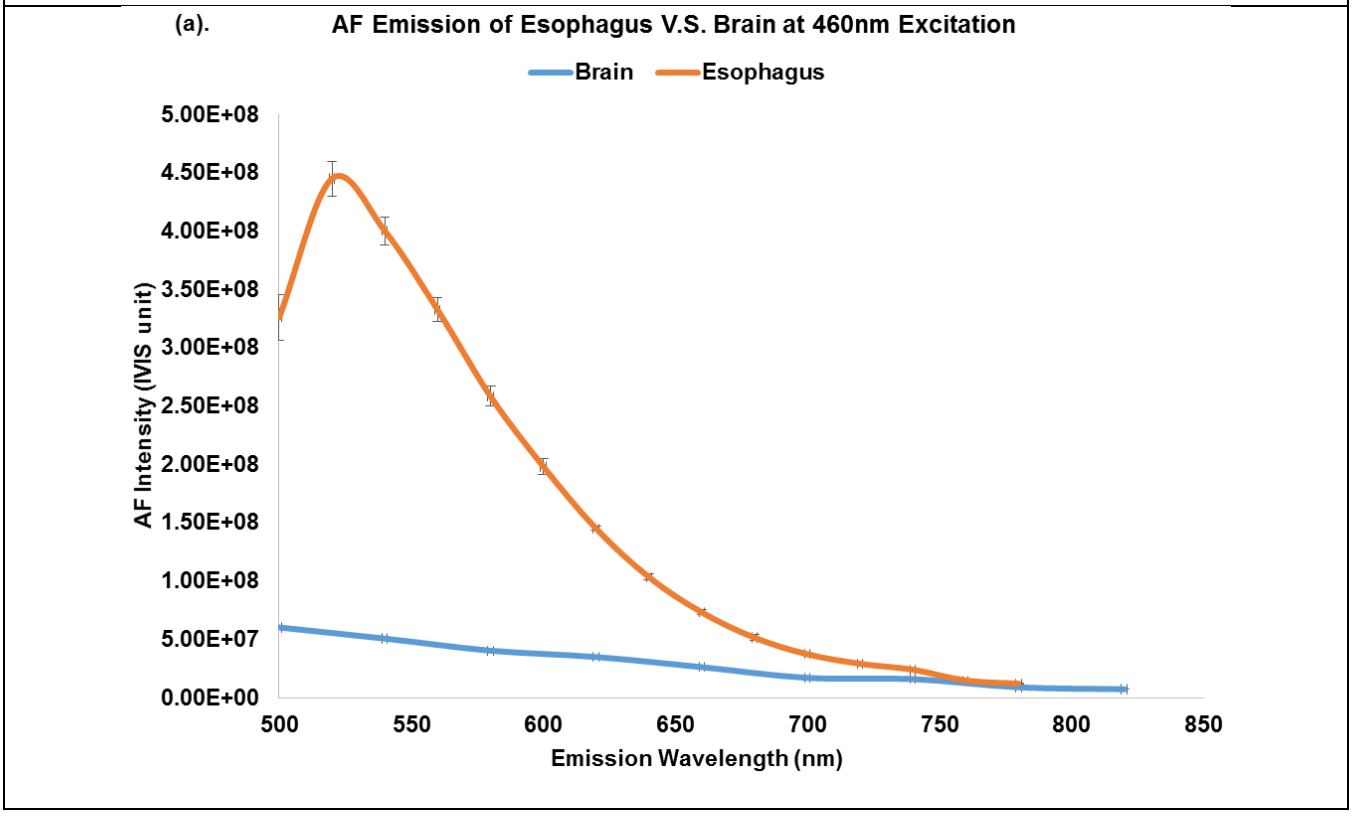

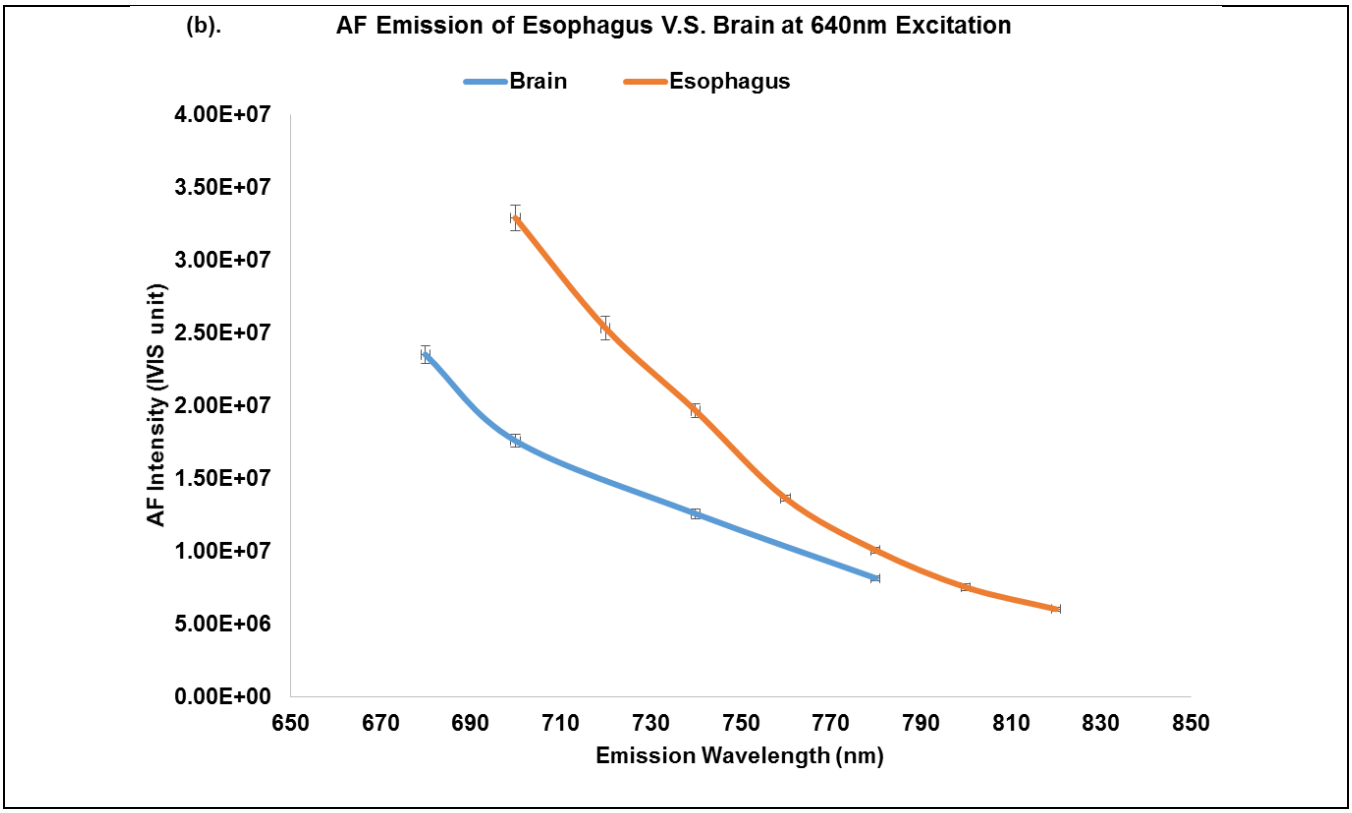

Any molecular imaging devices' contrast ratio will be limited to the AF background, unless the device can mitigate the "unwanted" AF signal. To achieve a high *in vivo* imaging T/B ratio, we implemented a real-time AF mitigation algorithm in the operating system software of the multispectral SFE, and demonstrated a T/B exceeding 80 using two different phantoms. This represents more than a 40-fold increase from a T/B of 2.1 without AF mitigation in the visible spectrum. These real-time imaging results were obtained with a tissue phantom featuring a collagen submucosal background and molecular targeting of mucosal early cancerous cells with 488 nm excitation.

In addition, the AF mitigation algorithm can also serve as a simultaneous specular reflection elimination algorithm. We demonstrated the elimination of false positive imaging artifacts caused by tissue specular reflections. Specular reflections are unavoidable when viewing glossy tissue surfaces such as the lung, oral and GI mucosa, blood vessels, bladder, and etc., even with well-

selected high optical density (OD=10) laser rejection filters. The bleed through signal creates false positive information, and leads to less specific results in molecular target identification. Compared with other approaches to mitigate bleed-through specular reflections, such as installing polarization filters, or constantly moving the angle of the endoscope to adjust light incident angles, the current approach is more convenient, economical and practical for clinical applications.

AF mitigation algorithms have also been reported and implemented in single frame camera imaging system [154] [169], and a T/B improvement of 23-fold was reported in [154]. However, real-time AF mitigation on an endoscopic device has not been previously reported. The principle of the current AF mitigation algorithm works by simultaneously launching a reference excitation laser together with the fluorophore excitation laser, and obtaining the respective emission signals in concurrent but separate detection channels (**Figure 44**). Mitigation of the background AF signal is realized by subtracting the target signal (fluorescein + AF2) from the reference signal (AF1) multiplied with a pre-calibrated ratio (CR), at a pixel by pixel resolution.

The basis for this type of AF mitigation is the assumption that the AF emission spectral profiles were nearly identical for both 448 nm and the 488 nm excitation. In the present study, we validated this assumption and showed that for both esophagus and brain, the AF emission profiles from the two separate excitation sources (430±15 nm and 460±15 nm) were nearly identical and even their emission intensities were very similar (**Figure 53**). Further assessment also showed that the AF emission spectra profiles from blue to NIR were nearly identical for both of the tissue types studied, indicating that the AF mitigation algorithm can be used for not only two close-by channels (e.g., the 448 and 488 nm excitation and corresponding fluorescence detection channels in **Figure 43**), but also a variety of other channels, with the appropriate pre-calibrated ratio.

Figure 53. AF mitigation rationale and emission profile consistency under two different excitation lasers

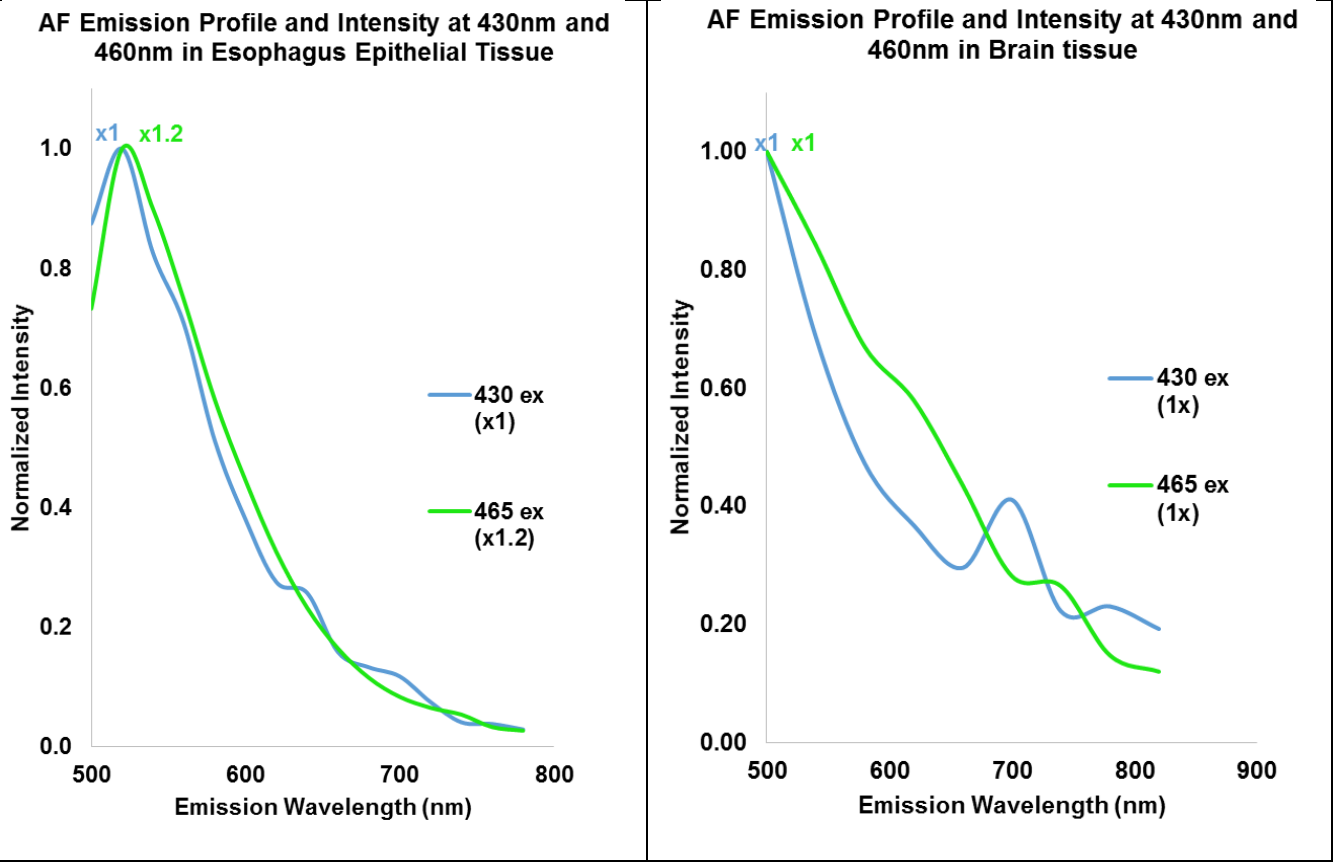

Furthermore, the current study demonstrated many clinically viable features for the newly developed multispectral scanning fiber endoscope applied to fluorescence molecular imaging. First of all, the endoscope's small size and flexibility with high resolution and high detection sensitivity will allow for many applications including the fluorescence molecular diagnostics in small ducts and tissue cavities, such as the peripheral lung, bile duct, and vascular system. Meanwhile, transnasal or keyhole brain surgeries may be realized with the SFE in the near future. Secondly, concurrent laser excitation with separate detection channels can allow for customized designs for a variety of fluorophore conjugate probe combinations. Finally, high T/B quantitative

fluorescence imaging with real-time AF and specular reflection mitigation will serve to increase the sensitivity and specificity of molecular imaging systems. Having an artifact-free, high-contrast multimodal image opens the door to new medical application, such as applying machine vision on an endoscopic device for computer assisted diagnosis at the point of care performed by non-experts and automating tedious therapeutic procedures guided by experts.

The motivation to develop the current real-time AF and specular reflection mitigation algorithm was for surface tissue imaging of topically applied molecular probes, in order to red-flag and guide biopsy of early cancerous lesions [72] [147] [170] [171]. In addition, quantitative assessment of the background AF as well as the mitigation algorithm can also be extended to apply to more sub-surface tissue imaging during fluorescence guided surgery [139] [141] [147]. During sub-surface tissue imaging, other confounding factors such as scattering and hemoglobin absorption will be considered. However, applications using two adjacent excitation laser wavelengths, such as 448 nm and 488 nm demonstrated in this study, may be robust enough to allow for both surface and sub-surface tissue imaging since their scattering and hemoglobin absorption profiles are quite similar to each other [172].

The excitation and emission features for sodium fluorescein and 2-NBDG used in this study lie within the visible range, where the background autofluorescence is comparatively higher than in the NIR range. An easy approach to avoid background AF would be to simply use dyes that emit at NIR wavelengths. However, concerns about non-specific binding exhibited by many NIR dyes, such as indocyanine green (ICG) and most cyanine dyes have been addressed [123] [147]. Because these dyes are not neutrally charged, they are susceptible to forming non-specific bonds which increase the fluorescence background and thus reduce the T/B ratio [110] [173]. Moreover, recent studies have also shown that, even for applications of conjugated NIR molecular probes, background autofluorescence still remains a major limiting factor to achieving a high contrast ratio [155] [156]. Therefore, in addition to the advancement of NIR fluorescent dyes [123] [173],

approaches for background AF mitigation are still in need for improved T/B imaging in NIR molecular probe imaging.

In the meantime, the inherent benefits of fluorescein based molecular probes can now be realized thanks to the real-time AF mitigation algorithm combined with a multi-channel laser-based flexible endoscope. In addition to over 90% quantum yield, good water solubility, high molar absorptivity, neutral charge and thus low non-specific binding to tissue, the FDA approved and low cost fluorescein dye also possesses the advantages of overlapping the widely used 488 nm excitation laser and sensitive visible wavelength photodetectors. Fluorescein derivatives are easily conjugated to antibodies and peptides for molecular specific labeling. Significantly improved T/B through AF mitigation enhances the utility of fluorescein-based molecular probes.

Photodegradation of fluorescein was not observed during the multispectral scanning fiber endoscope imaging. Since fluorescein is widely reported to undergo rapid photodegradation [146], we performed a quantitative estimate of fluorescein destruction under the laser illumination levels employed in the SFE. We then compared the fluorescein photodegradation rate under the illumination conditions used in a confocal microscope [144] (**Table 6**). For a 1 mw laser operating at 488 nm the fluorescein degradation time constant in a confocal microscope is about 240 microseconds since the laser intensity is much higher than that of the SFE. In contrast to the confocal microscope (spot radius = 0.25μm), the large spot radius of the SFE (25μm) leads to a much longer (4160x) photodegradation time constant (about 1 second). Combined with the SFE's short average dwell time of the laser spot on the target (40ns, or 0.04μs at 25 megahertz sampling rate [107]) yields a very low rate of fluorescein degradation. Therefore, as observed experimentally the scanning fiber design of the wide-field SFE leads to insignificant photodegradation of fluorescein. This allows more quantitative high-contrast fluorescence imaging to be maintained for the entire fluorescence-guided endoscopic intervention.

Table 6. Quantitative Estimate of Fluorescein Photodegradation Comparison of Confocal Microscope [144] and SFE		
	Confocal microscope	***SFE***
σ = Fluorescein Absorption Cross-Section	3.06 x 10^{-16} cm^2/molecule	3.06 x 10^{-16} cm^2/molecule
Laser (at 488 nm, 1mW) intensity	1.25 x 10^{24} photons $s^{-1}cm^{-2}$, spot radius 0.25 μm	1.25 x 10^{20} photons $s^{-1}cm^{-2}$, spot radius 25 um
K_a = Rate of Photon Absorption	3.8 x 10^8 s^{-1}	3.8 x 10^4 s^{-1}
Q_B = Photobleaching Quantum Efficiency	3 x 10^{-5}	3 x 10^{-5}
K_f = Rate of Fluorescence Emission (Reciprocal of Radiative Lifetime)	2.2 x 10^8 s^{-1}	2.2 x 10^8 s^{-1}
K_B = Rate of Photobleaching = $Q_B K_f K_a / (K_f + K_a)$	4.2 x 10^3 s^{-1}	1.15 s^{-1}
Fluorescein degradation time constant	**240 μs**	**0.9 s**
Laser spot dwell time (average)	**1-10 μs**	**0.04 μs**

In conclusion, we developed and demonstrated a novel approach to evaluate the fluorescence detection sensitivity of a wide-field multispectral scanning fiber endoscope (SFE) for clinical application, such as early esophageal cancer detection and brain tumor delineation. The approach

combines the evaluation of device fluorescence detection sensitivity with quantitative assessment of tissue autofluorescence (AF) background. A new method – Autofluorescence Equivalent Concentration (AEC) was developed and applied as a quantitative conversion of the background AF signal to the target fluorophore concentration, such that the background AF can be compared with the target fluorescence. Nanomolar sensitivity, wide-field SFE fluorescence imaging was applied to the delineation of brain tumors in a xenograft mouse model. Finally, high (>80) T/B was observed with a tissue phantom through the implementation of a real-time AF mitigation algorithm using the high sensitivity multispectral SFE.

6 Future Directions

The technologies and methodologies developed in above chapters can be used in many ways beyond those presented in this dissertation. For example, the wide-field multispectral quantitative fluorescence imaging technologies developed: Distance Compensation, Image Stitching, Crosstalk Mitigation, AF and specular reflection Mitigation algorithm, provide a suite of technologies and methodologies for advanced computer-assisted disease surveillance, diagnosis, and therapy monitoring. The body of work can be also extended for the applications in image-guided surgical intervention, and quantitative assessment of biofilm loading on medical devices *in vivo* and *in vitro*, etc. The following chapter will discuss a number of future applications/directions, which can be built on the foundation of this research.

6.1 3D quantitative multispectral fluorescence-reflectance endoscopic imaging

As endoscopy becomes increasingly attractive as an imaging modality for computer-assisted and minimally-invasive diagnosis and interventions, the current clinical practice of endoscopy is still based on merely qualitative observation from a sequence of video frames. Objective and quantitative information are needed in order to move endoscopic imaging towards computer/machine-assisted diagnosis, tele-surgery and/or intervention, out-patient clinics for routine screening or surveillance, and especially in under-served/under-developed areas where the lack experienced clinical staff is common.

Analyzing clinical endoscopic videos to obtain meaningful information about 3D anatomical structures, depth and color information (as shown in **Figure 54**) has been explored in the past decade thanks to the technological advancements in computer vision and image processing [174] [175] [176]. However, analyzing 3D information for multi-modal and multi-spectral fluorescence-

reflectance endoscopy has never been done in the past, mostly due to hardware constraints to produce spatially co-registered multispectral fluorescence-reflectance endoscopic images in real time. The unique multi-channel hardware design feature of SFE system, together with the foundational framework provided by this dissertation such as the Distance Compensation, Image Stitching, and background AF & Specular Reflection Mitigation algorithm, can be further developed into quantitative molecular endoscopy using absorbent or fluorescent dye indicators with 3-dimentional (3D) geometry in real-time to guide clinical diagnosis at point-of-care.

Figure 54. An example showing reconstructed 3D surface model of colon polyp from two different views. Top: 3D cloud point. Bottom: texturized 3D surface structure. Original figure from reference [176], page 6, figure 11.

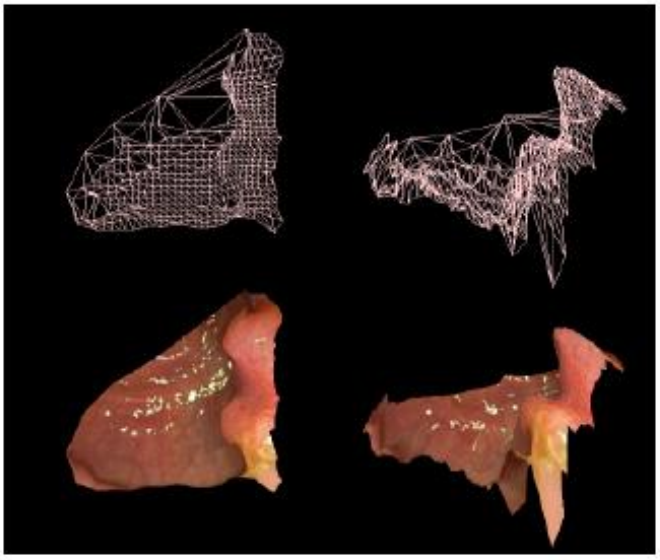

6.1.1 3D vision algorithm and methods

A rich amount of algorithm and technologies in 3D reconstruction can be found in [108]. In a previous chapter, optical flow was applied to reconstruct the 3D information of lower esophagus

endoscopic videos, due to the lack of rich anatomical features in the esophagus. Depending on the actual structures to be imaged, methods that can be further explored are (but not limited to):

a. Multi-view stereo (texture features required, and do not depend on the lighting condition)
b. Shape from motion (texture features required, and do not depend on the lighting condition)
c. Shape from shading (surface albedos are assumed to be constant)
d. Shape from silhouette (multiple concurrent cameras needed to achieve high resolution reconstruction)
e. Photometric stereo (reconstruct the surface normal by varying lightings)
f. Shape from structured light (projecting structured patterns and establish correspondences between different views)
g. Possibly confocal, interference (OCT), and LIDAR optical scanning techniques

6.1.2 Image reconstruction pipeline

The following pipeline in **Figure 55** is adapted from [176], which demonstrated a robust estimation technique for computation of 3D structures from white light endoscopic videos:

Figure 55. A proposed pipeline for generating 3D quantitative multispectral fluorescence-reflectance endoscopic imaging.

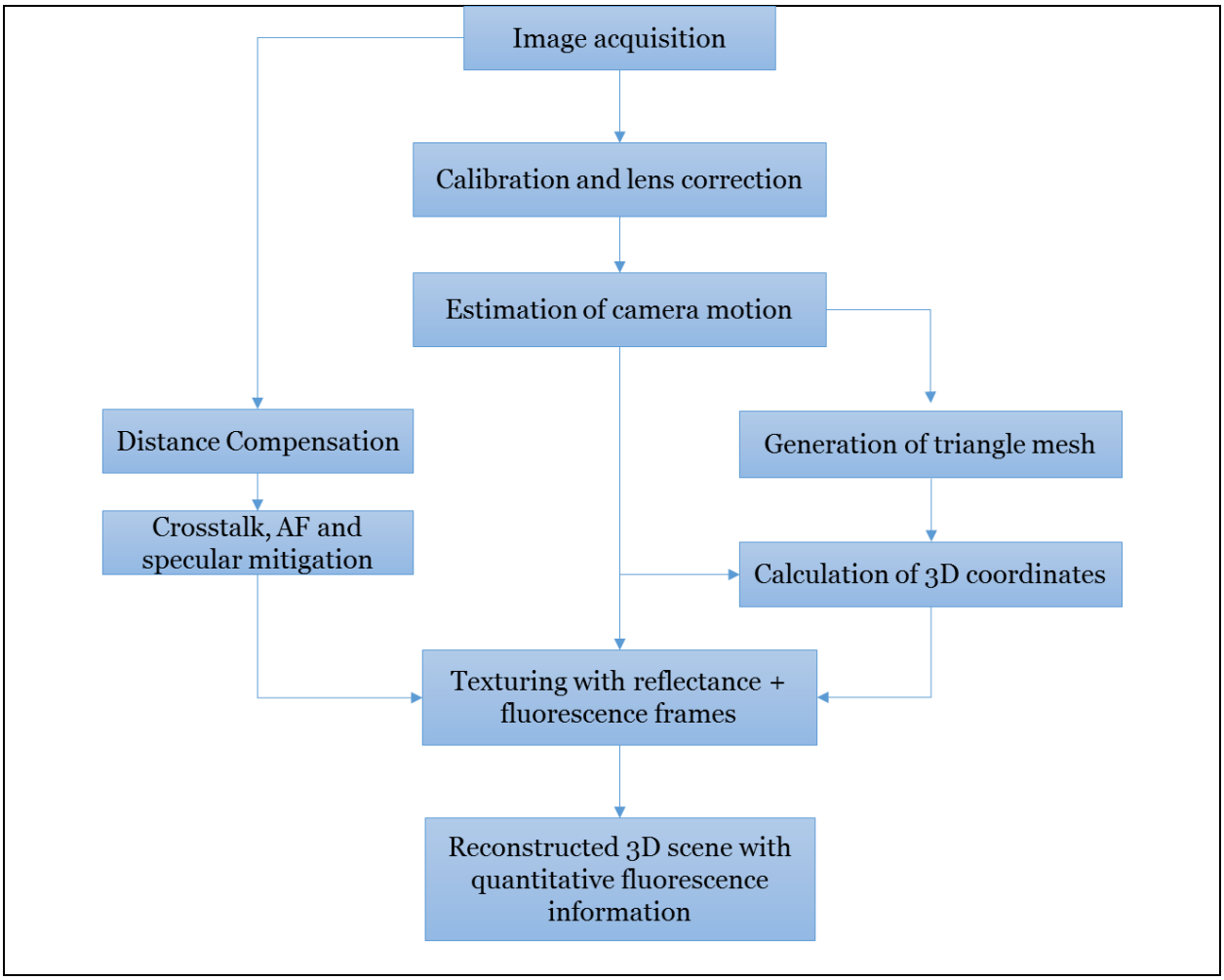

6.1.3 **Challenges in real-time video processing**

The 3D quantitative fluorescence-reflectance endoscopy will be needed in real-time for guiding biopsies and/or intraoperative interventions. However, a key challenge for the computationally intensive computer vision algorithm is the performance of the software solution (speed, memory, storage, etc.) that meets the real-time requirement, especially for most medical endoscopic devices/embedded systems which requires portability and low-power consumption without having to sacrifice the image resolution and quality.

One of the most promising solutions to improve the performance of real-time video processing is parallel computing with graphics processing unit, which was popularized by the video game industry and has rapidly gained maturity for computationally demanding applications. Meanwhile, recent advancement in real-time computer vision algorithm processing in smartphone and wearable device applications have also shown solutions to this problem. Advanced sensor tracking technology has also added possibilities to acquire additional information to assist tracking of camera motion in real time, such as the use of an accelerometer. Future exploration is needed to evaluate and transfer these cutting-edge computer science technologies into real-time 3D quantitative endoscopy.

6.2 Hot-spots identification for quantitative fluorescence molecular endoscopy

6.2.1 Hot-spots identification – current progress and future development

Fluorescence molecular endoscopy improves disease detection by targeting specific disease state related biomarkers, in the meantime, increased detection sensitivity to overcome individual disease heterogeneity is achieved by concurrent administration and imaging of multiple molecular probes. However, the realization of these powerful strengths of multi-spectral fluorescence molecular endoscopy cannot be achieved without reaching a high contrast ratio for the targeted hot-spots *in vivo* at real time.

Achieving a high contrast ratio (or T/B) and then to easily identify and track targets has been one of the major goals for this dissertation work. In Chapter 4 and 5, a real-time autofluorescence (AF) and specular reflection mitigation algorithm was developed and demonstrated a T/B improvement increase from 2 to over 80 on a tissue phantom. The background, after applying the real-time algorithm, was reduced to electronic noise floor, which in the current SFE system with high sensitive PMT detectors is minimal. Through this algorithm, the target was easily ascertained

and tracked by naked eyes, and (relative) quantitative fluorescence imaging is realized by applying the Distance Compensation algorithm (developed in Chapter 2) and will be shown as a scaled colormap on the monitor display to guide intraoperative biopsies and interventions in the upcoming in human study.

However, during *in vivo* applications, non-specific sources can occur in the background, and significantly reduce the currently established high contrast ratio on the multispectral fluorescence endoscopy. Non-specific sources usually interfere with the T/B through the following:

[1]. Non-specific pooling. As described in details in previous chapters, the molecular endoscopy procedure starts with the administration of exogenous fluorescent probes. The probes are administered either intravenously (i.v.) or topically. After several minutes (for topical application) or hours (i.v.), some fraction of the probes link to their targeted biomarkers. The next step is to rinse away the unbound molecular probes: For the topical approach, a saline wash step is applied through a working channel of the endoscope. However, due to certain anatomical unevenness and/or physiological activities (such as small body cavities, respiratory movement, bowl movement, and etc.), some unbound probes can escape the saline rinse and remain in the body (a.k.a., non-specific pooling), and be misdiagnosed as targeted hot-spots. The non-specific pooling problem can be solved by improving the hardware design of the saline wash system to guarantee a uniform application and flow of the rinsing medium. Specialized training will be needed to insure proper purging of unbound excess probe material.

[2] Non-specific binding. The i.v. administration approach is particularly prone to non-specific binding since a rinse/wash step is not applicable for deep tissue applications. In this case, non-specific binding can occur due to non-uniform transport kinetics of the molecular probe, probe-tissue binding affinity, the charge of fluorophore dye used, and etc. However, although the topical approach is less affected by non-specific binding, some probes might still escape the saline wash

and create a non-specific binding background due to probe chemistry and probe-tissue affinity changes in the tissue microenvironment.

6.2.2 Target Identification – Image Segmentation

Existence of the non-specific background is non-trivial when it comes to identification and quantification of targeted hot-spots. Furthermore, non-specific binding is un-predictable, and unlike AF it cannot be segregated based on distinctive spectral profile patterns.

Ultimately, as discussed in Chapter 5, non-specific background can be significantly reduced by molecular engineering of next-generation fluorophore. An example is the zwitterion near-infrared dye ZW800, which yielded a 3.4x T/B increase compared to IRDye800-CW and a 6.9x increase relative to Cy5.5 [123]. However, before these new fluorophores are widely produced, regulated, and adopted for *in vivo* applications, real-time image processing algorithms need to be explored to mitigate the non-specific background.

To mitigate non-specific binding from exogenous molecular probes, Liu et al. developed a ratiometric approach which was shown to reduce the negative effects of nonspecific binding and provided a quantification for the specifically bound probes. This method works by simultaneously imaging of two molecular probes. One fluorophore is linked to an isotype-matched negative control probe and another fluorophore is linked to the desired targeted probe. Then, a pixel-by-pixel ratiometric algorithm mathematically quantifies specific versus nonspecific binding affinity. Details about the approach can be found in a publication [110] by Liu and co-workers. While this method has been demonstrated effective for thick pathological tissue specimen using a microscope [110] [111], a potential question for extending this approach to *in vivo* use, is the concern over administration of double dosage exogenous molecular probes (one target probe and one negative control probe for each biomarker), which is a necessary element to make this

approach successful. However, compared to standard molecular biomarker applications (only one target probe for each biomarker), the human body now has to process and clear out a 2x amount of probe material. In addition, this double-probe ratiometric algorithm assumes that the simultaneously administered molecular probes exhibit non-specific pooling in the identical spatial fashion. However, since non-specific pooling can be caused by operator errors, locations of non-specific pooling of the target probe can be significantly different than that of the negative control probe, especially for applications such as *in vivo* endoscopy of colon and esophagus, where the inspection area is significantly larger and saline wash is significantly more difficult (due to unevenness in the anatomy), than the applications on skin surface or pathology tissue samples. Meanwhile, another confounder that might need to be taken into consideration is the difference in fluorophore dye photo degradation rate between the target and the negative probe. This could be mitigated by either selecting dyes that have closely matched photo degradation rates, or by adding a compensation factor in the mathematical equation. In summary, this ratiometric approach is robust and can be operate in real time, its application for *in vivo* wide-field multispectral fluorescence endoscopy should be evaluated in the future, including acquiring sufficient data on pharmacokinetics and pharmacodynamics effects of double doses molecular contrast agent administration.

In the meantime, image segmentation is a promising approach to delineate specific from non-specific binding areas. Image segmentation algorithms have been studied and applied in medical imaging, primarily for magnetic resonance imaging (MRI), computed tomography (CT), and digital mammography to delineate anatomical structures and other areas of interest, and assist/automate specific radiological tasks. The classic definition of image segmentation refers to partitioning an image into non-overlapping, constituent and homogenous individual regions based on certain characteristic such as intensity or texture [177].

Several image segmentation methods are listed below, and their relevance to the identification of targets from non-specific binding background will also be discussed:

a. **Thresholding**. Based on a determined intensity value – threshold, the regions of interest are segmented out through grouping all pixels with intensities greater than the threshold (intensity here can be color, texture, or any other element that has quantitative meaning). The threshold can be determined interactively by clinician operations or automatically through a pre-set value in the algorithm. It is often generated through a histogram plot of the image pixel intensities. For identification of target from non-specific background, thresholding can be a simple but effective way in cases where non-specific background creates contrasting intensity (or other quantifiable properties) than the target [177]. In some cases, multi-thresholding can be applied if more than one threshold value is needed to segment different types of targets/background.
b. **Region growing.** This method segments the regions of interest based on that a hot-spot area is connected through certain predefined criteria, such as pixel intensity information from one or multiple color depends on the specific application, edge gradient, etc. It often starts with a seed point and "grow" the region until it meets the edge (for example, when it reaches significant intensity gradient change). Region growing is similar in some way to the thresholding approach. In addition, approaches have been developed to identify "fuzzy" edges or edges with noise background [178].
c. **Active contour.** This is also referred to as deformable models. It is a model-based method for segmenting region boundaries by using closed curves or surfaces that deform under the influence of internal and external forces. Usually, a parametric circle is initialized and allow to relax/deform to reach the boundary delineation. The major advantage of active contour is that it's robust to noise and spurious edges, and therefore popular among most medical imaging applications, including in biomedical optics such as

segmenting and tracking fluorescent cells in dynamic 3D microscopy [179]. Future studies should explore this approach and its effectiveness in delineation of hotspots from unpredictable and inhomogeneous non-specific background.

Meanwhile, some other machine learning algorithms can be considered to assist the image segmentation process. These algorithms include but not limited to: clustering (K-means clustering, the fuzzy c-means algorithm, etc.), Markov Random Field modeling, Artificial Neural Networks, and etc.

6.2.3 Potential Challenges

One difficulty that can impact the accuracy of hotspots segmentation is intensity inhomogeneity which can be resulted from certain confounders such as geometry and tissue property inhomogeneity. Compensation algorithms need to be developed to mitigate this problem prior to the segmentation step. Distance Compensation developed from this dissertation work can be used to compensate geometry-caused intensity inhomogeneity.

Another problem is the tradeoff between clinician-supervised (semi-automated) segmentation and fully automated segmentation. Often times, image segmentation that's guided by medical experts can lead to more accurate results, but it also slows down the process and hard to fit into the busy clinical workflow. Fully automated segmentation is hard to implement as a consequence of intensity inhomogeneity and patient heterogeneity.

The **accuracy** and **precision** of the segmentation algorithm should be evaluated (stared with different *in vitro* phantom models and gradually move to *in vivo* models). Meanwhile, the speed and general performance of the segmentation software also needs to be considered as an important factor, and tradeoffs need to be made between speed, accuracy and acceptance into the clinicians' workflow.

6.3 Further development of fluorescence calibration standard

For quantitative fluorescence imaging, calibration standards are necessary for the quality assurance of the imaging device, as well as for algorithm/methodology development. These standards are also crucial for the establishment of cross-center and cross-device optical measurements in multi-center studies for the screening and diagnosis of early-stage disease (cancer) states.

A dye-in-polymer technology was developed in the dissertation project, to construct photo-stable, distinctively shaped, quantitative and portable fluorescence calibration standards, which also match with the absorption-emission spectral profile of the dyes to be used in the *in vivo* studies for the Barrett's Esophagus Translational Research Network.

Some future directions on expanding this area:

a. **Fluorescence calibration standards with scattering properties for deep tissue imaging.** In this case, scattering particles such as titanium dioxide can be quantitatively and evenly dispersed in the dye-in-polymer material to match with the scattering property of the tissue to be studied. This addition is also very important in the fabrication of NIR fluorescence calibration standards, as most NIR fluorescence imaging can penetrate deep into the tissue (centimeters), and therefore, scattering properties should be considered in standards for NIR dye standards.
b. **Resolution test targets for fluorescence endoscopic imaging.** For conventional white light imaging, the 1951 USAF resolution test chart is often used as the test target to evaluate image resolution. However, this test chart is only suitable for reflectance imaging. To evaluate the resolution of fluorescence imaging, off-the-shelf but expensive microspheres/beads or nanospheres/beads are often found in publications. Meanwhile,

UV fused silica and fluorescent USAF 1951 resolution targets are also commercially available (Edmund Optics, Inc) but for UV excitation wavelength (365nm) only. With the convenience and low-cost of the dye-in-polymer fabrication method, it is possible to add "resolution calibration" as part of the features in the quantitative fluorescent targets for a wide-range of visible and NIR dyes.

c. **All-in-one quantitative calibration targets for multimodal medical imaging**. Embedding CT/MRI fiducial markers, to allow for multi-modality imaging strategies for disease diagnostic and treatment, is another future embodiment of the calibration targets. For example, the co-registration of optical images with CT/MRI volumetric imaging could enable new optical-to-CT/MRI combined data for pre/post tumor resection surgery comparisons. Magnetic Microspheres (Bangs Laboratories, Inc) are stable and dispersible in the urethane resin material, and can be made to contain both magnetic and fluorescent material. Properly functionalized spheres could be dispersed in urethane resins and included in the fabrication process to allow this multi-modal imaging.

6.4 Improving Software and hardware components to mitigate emission spectra overlap in wide-field multispectral fluorescence endoscopy

One of the challenges for the implementation of multispectral fluorescence molecular endoscopy is the spectral overlap, or cross-talk of the fluorophore emission spectra, as laser sources can help to reduce overlap in excitation. In this dissertation, three different approaches: 1. Image Stitching, 2. Concurrent imaging with Cross-talk Ratio Subtraction (CRS) algorithm, and 3. Frame-sequential Imaging were developed and evaluated for the mitigation of fluorescence emission cross-talk in the wide-field multispectral SFE system.

After comparing the 3 approaches, as discussed in Chapter 4, the Concurrent imaging using CRS algorithm was the best solution for the short-term, and was implemented in the newly developed

multispectral SFE system for real-time applications in the upcoming BETRNet *in vivo* study. The limitation of this method is that a pre-scan calibration is needed and device settings (gains/offsets on the digital display and PMT detectors) have to be maintained. For the long-term, as the number of detection channel (emission overlapped channel) increases, the complexity for the pre-scan calibration procedure increases from minimal technical training and <3 minutes calibration time (current situation) to increased technical skill and >5 minutes calibration time.

Therefore, improvements for both software solutions for the Image Stitching method and hardware solutions for the Pixel-sequential Imaging approach (Chapter 4, Discussion) should be studied and implemented in a future multichannel fluorescence-reflectance SFE system.

For the Image Stitching approach, two software/algorithm improvements are suggested:

[1]. Optimizations on the current software solution to enhance the speed for data processing. Advanced Graphics Processing Unit and parallel computing algorithm can be considered in addition to improve the performance. Ultimately, this solution will be able to operate in real time.

[2]. Increase the robustness of the currently used algorithm/pipeline by adding in steps to compensate for unpredictable motion during *in vivo* imaging. The current software pipeline, as described in details in Chapter 3, uses a pairwise pose estimation to look for two camera poses given every two consecutive input video frames. To construct the full panorama, the pairwise registration was applied to each pair of the consecutive frames. This method, although less computationally intensive, can increase the error in registration, as it could result in two inconsistent pose estimates at each frame. To obtain a more accurate/robust post at each frame, a global optimization algorithm is needed which should be able to minimize the error between successive frames simultaneously.

Details of this global optimization algorithm can be found in [180]. This global optimization approach is similar to structure from motion (SfM) and bundle adjustment. However, bundle adjustment requires tracked features as input, which is not realistic for endoscopic applications, given that a lot of anatomical surfaces lack distinctive features. But in cases distinctive features are possible, such as in the human bladder, human teeth, or combined multi-channel fluorescence-reflectance images, SfM with global optimization should still always be considered as an option to increase the accuracy and speed for the current approach.

Improve the Sequential Imaging approach through hardware advancement

As discussed at the end of Chapter 4, the Pixel-sequential Imaging approach could be the best solution for the long-term, as it can not only avoid dye emission crosstalk, but also operate in real time with no pre-scan calibration required. These strengths are ideal for the *in vivo* clinical scenario. However, at the current SFE system operation, the Frame-sequential Imaging approach only runs at 10Hz frame rate, and additional lag time was added as video processing is needed to combine the sequential and individual frames into multi-spectral video frames using an added frame grabber device (Epiphan, Inc, Ottawa, CA). Therefore, the frame rate for this approach must increase by a factor larger than the number of fluorophores in order to display a real time view that adapts to body movement *in vivo*. A feasible approach will be to upgrade the present SFE endoscope system with faster modulation laser components. In conjunction, laser control software on the Field-programmable gate array (FPGA) of the SFE system need to be updated to modulate the lasers at a much faster rate. The technical aspects of the upgrade was discussed in Chapter 4, Discussion section.

6.5 Design and Develop Hotspots Visualization and Documentation for Wide-field Multispectral Fluorescence Endoscopy in the Clinical Setting

The multispectral SFE will, for the first time, provide clinicians with multicolor fluorescence molecular endoscopic imaging in real time. This new technology has created opportunities to the whole new field of computer-aided decision support systems in medical endoscopy, and at the same time also adds a wealth of information/data for the existing clinical workflow. Visualization technologies/software is in need to integrate this newly added data into the current clinical work flow. Documentation of this new patient data should also be included in this integration. Development in this area should start with understanding of the clinical workflow (**Figure 56**), and integrate the quantitative multi-spectral fluorescence SFE imaging technologies through design and implementation of user-interface with image processing and computer vision technologies. Ultimately, it will be a combination of software solutions to provide the ability and analysis for translating the wide-field multispectral/multicolor fluorescence molecular endoscopy in the clinic setting.

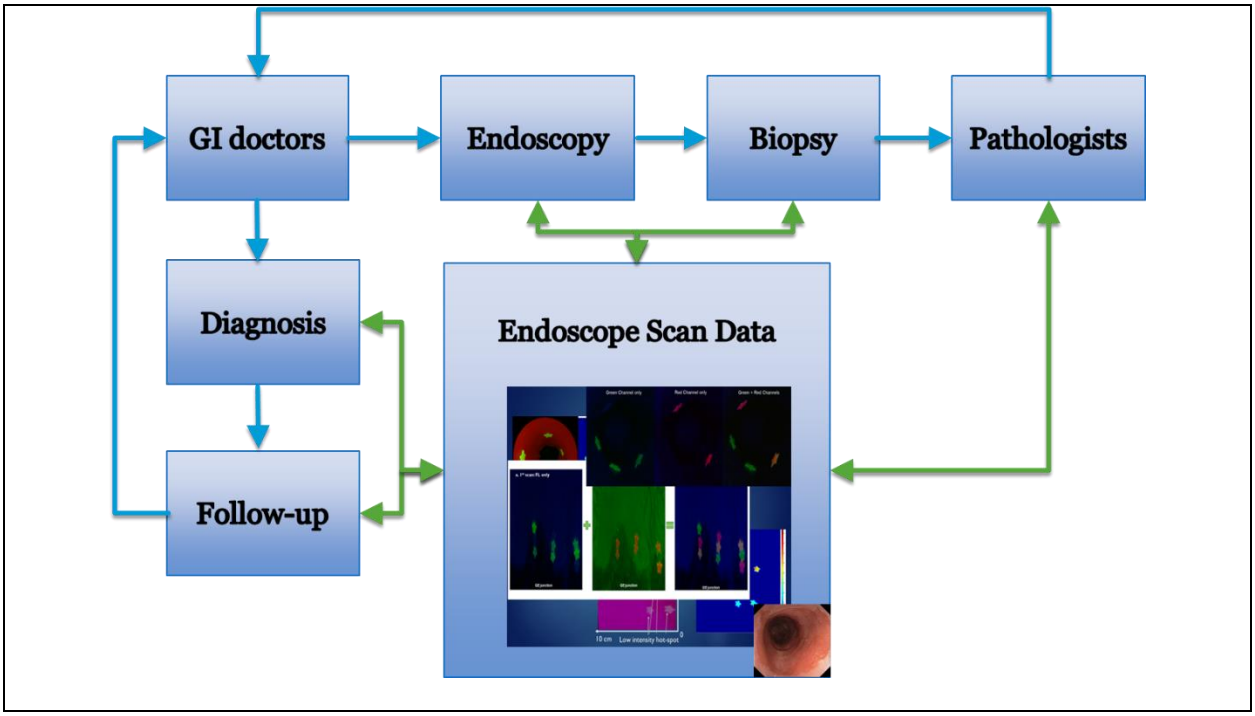

Figure 56. Visualization & Documentation for *in vivo* multispectral fluorescence endoscopic imaging integration with the current clinical work flow.

6.5.1 Design goals of the visualization solution

During endoscopy procedure,

1. Provide a mapping system/approach to "red flag" the presence of hotspots (e.g., HGD and early cancerous lesions) either integrated or overlaid with conventional white-light endoscopy on a single display, for image-guided biopsy and/or surgical intervention.

2. Grading (possibly based on measured shape, size, location, texture, intensity, color) of the red-flagged hot-spots using thresholds chosen by clinical researchers on the quantitative SFE fluorescence imaging.

3. Color-coded visualization of multiple molecular probes' spatial localization and co-localization, overlaid with conventional white-light endoscopic view or in a separate panoramic view generated using image stitching software solutions.

Documentation of quantitative multi-spectral fluorescence endoscopy information as electronic record:

1. Documentation of the hot-spots spatial localization and quantification in a panoramic map, possibly three-dimensional and scaled for future registration to other imaging modalities like X-ray, CT, MRI, PET, Ultrasound, etc.

2. Documentation of each biopsy sample's spatial location, fluorescence intensities, and molecular probe composition.

3. The documentation will be saved as standard clinical file format, such as Digital Imaging and Communications in Medicine (DICOM), and should follow codes for HIPPA regulations.

4. The documentation will be part of patient information, and also de-identified data can be used for clinical research studies following the research institution's specific regulations.

Basic methodologies and algorithm for quantitative multi-spectral fluorescence SFE imaging have been developed in this dissertation. Further optimization of the software/algorithm will be needed to integrate the solutions at real time clinical settings.

6.5.2 Suggested process for integrating the multispectral SFE into the clinical workflow

The user experience design and its integration with clinical workflow are critical and can be addressed in the following plan:

1. Work with clinicians and pathologist to understand clinical workflow

2. Give presentations to clinicians about multi-spectral fluorescence endoscopy and follow up with MDs for first round of interview about integration of this technology into clinical work flow – This can be done at both UW Medicine, and at clinical conference sessions focused on advanced endoscopic imaging technologies such as the Digestive Disease Week for GI.

3. The general comments initialized from 2) will give guidance to design and development of software solutions for data visualization and image fusion for *in vivo* quantitative multispectral fluorescence endoscopic imaging

4. Conduct user study to evaluate the solutions with clinicians.

6.5.3 User Study

The planned steps of the user study are as following:

Step 1: Interview 5-10 potential users/professionals. (Make sure all interviewees have a good diversity of professional background, for example, senior doctors vs. junior fellows/residents, clinicians vs. engineers, doctors vs. physician's assistants/nurse practitioners.) The goal is to come up with a list of common features that are important from a diverse user pool.

Step 2: Develop paper/flipbook prototypes for user study in the interviewees in step 1. Qualitative evaluation/measurement of the prototypes will be conducted focusing on the user error, consistency of positive/negative comments and ratings on each prototypes.

Step 3: Based on feedback and results from step2, create the UI prototype on computer using Powerpoint presentation, or Javascript with HTML5/CSS – Note: this is not the whole interface but things/features that are important to be tested. Iterate the design evaluations as step2.

Step 2 and 3 will use images/videos from the realistic phantom.

Step 4: Make iterative changes based on qualitative results from step 2 and 3, refining the visualization design of list from Step 1. In this step, the prototype can incorporate *in vivo* experiment videos (mouse colon, or human subject studies with multi-fluorescence).

Again, the goal of the study is NOT about coming up with a software package/user interface. Instead the goal is to get information from scientifically designed studies to come up with solutions/guidelines for the integration of quantitative multi-spectral fluorescence SFE imaging technologies for the *in vivo* setting.

6.6 Improve Diagnostic Accuracy with Computer-Aided Decision Support System through Data generated from Quantitative Multispectral Fluorescence Molecular Endoscopy

Molecular imaging with a wide-field multispectral fluorescence-reflectance endoscope enables visualization of specific markers that tracks disease progression at cellular and sub-cellular level. This new type of endoscopic imaging modality will be combined with advanced computerized image processing technologies, to provide quantitative and objective information and assist disease detection in early development stages and reduce mortality rate. The key goal for multispectral molecular endoscopy, is to improve the specificity and sensitivity of disease/early cancer diagnosis by providing more information and analytics at cellular and molecular level.

6.6.1 New information/data generated and contribute to medical endoscopy

New types of information generated from this dissertation, together with technologies already developed on the ultrathin SFE system are:

a. Continuous wide-field (>80 degree) and high resolution (<50 microns) multispectral fluorescence-reflectance endoscopic videos in real time (30Hz).
b. Quantifiable fluorescence intensities of fluorescent probe labelled disease specific lesions, which could be converted into absolute fluorescence intensities with a fluorescence calibration standard.
c. For each hot-spot, knowledge about its spatial location, co-registered reflectance-fluorescence intensity information, and anatomical features.
d. All hot-spots can be shown in a 2D or 3D panoramic map (including spatial and reflectance-fluorescence image intensity information), and hot-spot distribution patterns can be generated through analyzing the panoramic map.
e. 3D structural information of the inspected area with hot-spots fluorescence intensities overlaid and registered with other 3D imaging modalities.

f. Some disease-related spatial patterns, such as: Hot-spots that contain co-localized biomarkers (usually happens when >2 biomarkers are positively associated with disease state), and/or hot-spots that show complementary spatial pattern of biomarkers (usually happens when one biomarker is positively associated with disease state, while the other biomarker is negatively associated with disease state). Other types of disease-related special patterns can also be included in this category.
g. Longitudinal analysis of hot-spots over time, especially important in surveillance and therapy of chronic diseases such as Barrett's esophagus

The effectiveness and efficacy of applying molecular endoscopy into disease diagnosis are currently under research and development. However, it is expected that these new information, when combined with gold-stand pathologies, will ultimately increase the level of confidence in predicting disease pathological status, and assist clinicians to improve the accuracy of endoscopy-guided biopsies and diagnosis [181]. To be able to efficiently utilize the new data from quantitative molecular fluorescence endoscopic imaging, a data-driven, computer-aided supporting system should be developed.

6.6.2 Main functions of the computer-aided supporting system for endoscopy

The computer-aided (assisted) system will be built based on advanced statistical modeling and machine learning algorithm, where detection of features will be automated/semi-automated through a set of sufficient training data selected by medical experts. Such as system focuses on serving the following clinical scenarios:

(1) During operation, identify regions of particular interest for clinicians, and reduce the number of necessary biopsies to be taken. The regions-of-interest will be identified automatically, or semi-automatically through guidance of a medical expert. Ultimately, this action will reduce the time and cost for a procedure, as well as to reduce the discomfort of the patient.

(2) During an off-line and possibly remote case discussion session, when endoscopy videos are evaluated, such system will also be able to automatically remember/identify the regions-of-interest, and therefore reduces the time and effort for inspection of such data intensive and time consuming endoscopic video record.

(3) Not only does such system provides more objective data to inform clinicians, but it also enhances the accuracy of disease diagnosis by "always concentrating". As sometimes, small but critical abnormalities might be missed due to human errors. A computer assisted system will always monitor, detect, and track any possible lesions.

(4) The computer-assisted system will also be able to support medical education. Using such as system, a new clinician can be trained and evaluated to use molecular endoscopy. For example, the new clinician can make diagnosis/virtual-biopsies based on endoscopic videos, and compare his/her diagnosis with a computer system which has learned to automatically to detect disease-associated features through experts' selected training sets.

Prior work on the development of computer-aided system in guiding medical endoscopy has been discussed in a recent review paper [182]. However, the development of such a system has mostly been based on capturing features from conventional white-light endoscopy, or sometimes narrow-band imaging, and then combine with pathological results.

6.6.3 Design schematics of the computer-assisted supporting system

The design of a computer-assisted (aided) supporting system for endoscopic imaging contains in general 2 steps:

Step 1 (illustrated in **Figure 57**): Creating training endoscopy frame set with ground truth. Endoscopic frames are selected from existing diagnosed cases by medical experts. Usually the training sets' pathological or other related information are also known. The diagnosis can be positive and/or negative.

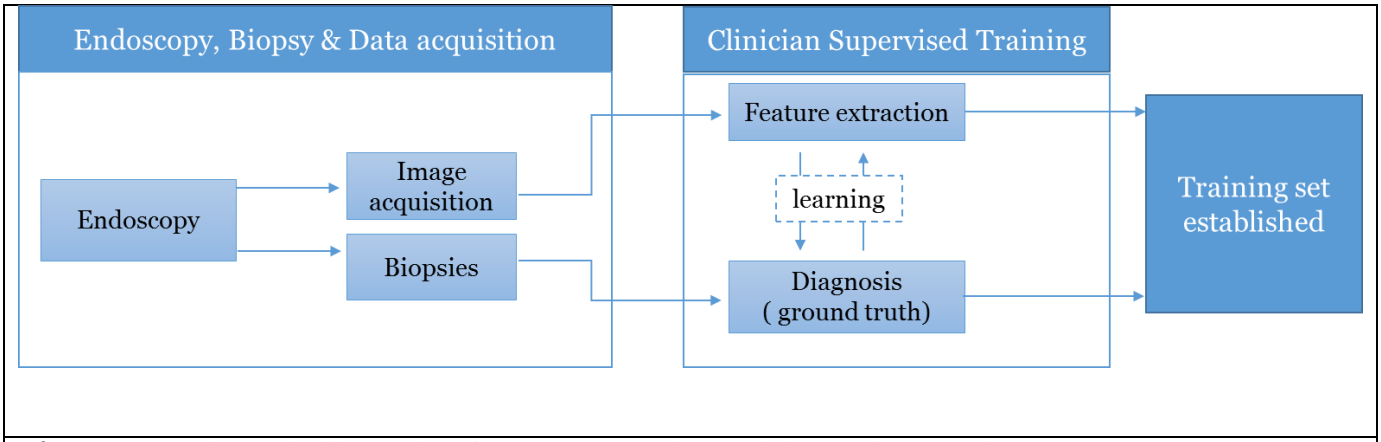

Figure 57. Schematic illustration for Step 1: Creating training endoscopy frame set.

Step 2 (illustrated in **Figure 58**): Performing diagnosis prediction from an image with unknown pathological results, based comparing/matching with knowledge from the training set.

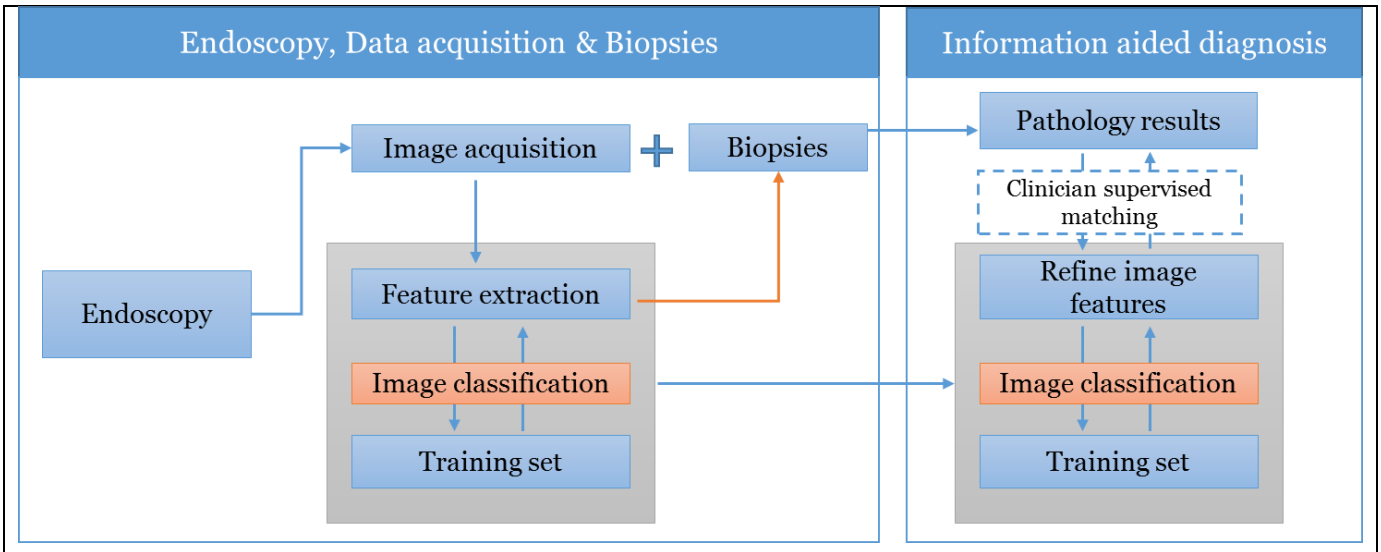

Figure 58. Schematic illustration for Step 2: Performing diagnosis prediction from an image with unknown pathological results. The prediction starts with extracting features from current endoscopy scan and compare them against the training set through pre-defined image classifiers (automatically), and then biopsies are taken based on both clinician's inspections through raw real-time video and suggestions from automatically detected hot-spots. Next, pathology results of the same hot-spot are compared with image features extracted from current scan, and/or similar hot-spots from previously diagnosed cases from the training set, and with the supported information, clinicians make a diagnosis of the current case.

Possible future step (illustrated in **Figure 59**): Assisting Personalized Diagnosis and Treatment

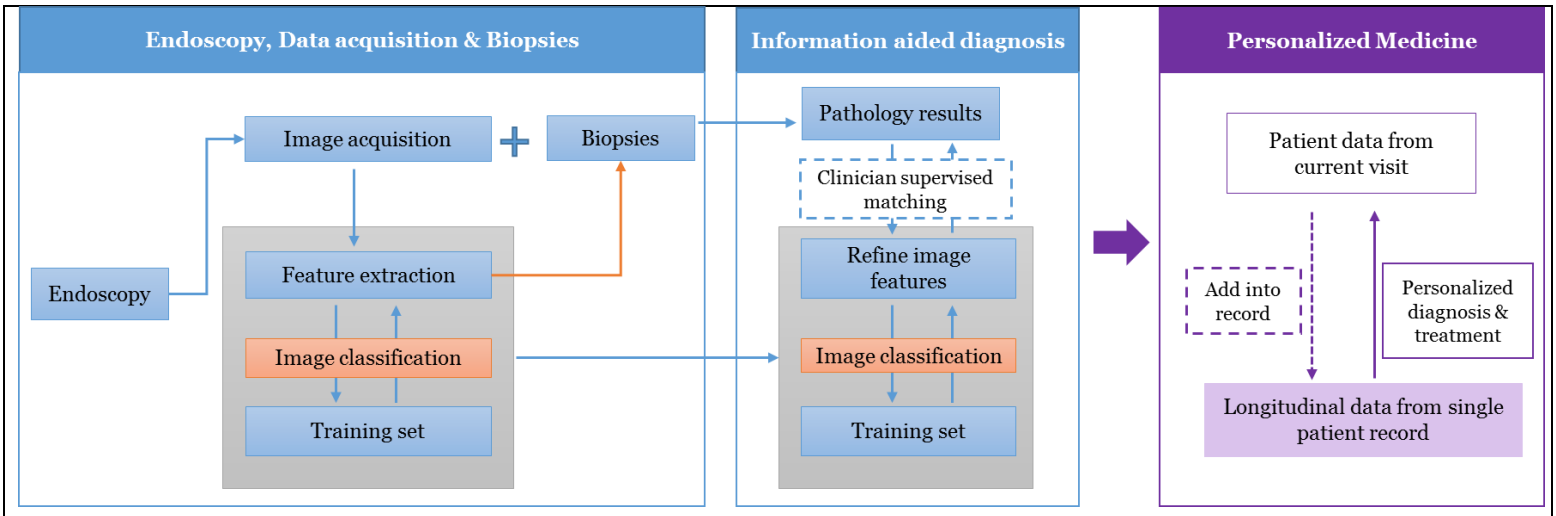

Figure 59. In addition, the computer-aided supporting system will be able to improve the speed and convenience of future personalized medicine. The current endoscopy can be compared with the previous endoscopies of the same patient, as well as combined with other clinical data. The longitudinal database contains all the information about the patient's prior diagnostic and treatment history. It is possible, that in the future, the structured personalized database, together with advanced search algorithm with natural language processing solutions, can extract and leverage knowledge from the patient history, which then seamlessly guide personalized medical diagnosis and treatment in the clinical setting.

6.6.4 Evaluation of the computer-assisted supporting system for medical endoscopy

The evaluation metrics for the system will majorly focus on (but not limited to):

1. Accuracy and Precision of such a system in predicting diagnosis or therapy outcome
2. Sensitivity and Specificity in predicting diagnostic or therapeutic results
3. The area under the Receiver Operating Characteristic (ROC) Curve
4. Sample size and quality of the training set (across different people and within a longitudinal set of endoscopies within the same individual, maybe under therapy)

5. Accuracy of the algorithm used to create classifiers (for matching up features)
6. Software runtime performance (e.g., for real-time suggestions in guiding biopsy, the speed in identifying hot-spots should be within milli-second, and for off-line suggestions in guiding diagnosis, the speed can be slower but should still be within seconds.).

7 Conclusion

This dissertation aims at improving early disease state diagnosis and intervention through the development of wide-field and quantitative multi-spectral fluorescence-reflectance endoscopic imaging. This entails the development of algorithms and technologies for quantitative fluorescence molecular endoscopy on a wide-field ultrathin and flexible multispectral fluorescence scanning fiber endoscope (SFE) device.

In the first aim, for the quantification and real-time visualization of probe-biomarker binding on the mucosa surface of the esophagus, an innovative realistic esophagus phantom was developed which matched the colors of the normal and diseased regions of the esophagus, and next, calibrated fluorescence standards were fabricated using a dye-in-polymer technology which contributed to the phantom to mimic the visualization of HGD lesions *in vivo*. Furthermore, a new algorithm: Distance Compensation was developed on the phantom which utilized the unique concurrent multi-channel feature of the SFE, and demonstrated *in vitro* the elimination of distance as a confounder and showed quantifiable fluorescence intensities for hot-spots quantification. Subsequently, an image stitching algorithm and software pipeline was developed on the phantom to generate enhanced visualization of the endoscopy by stitching video frames of the fluorescence molecular endoscopic imaging procedure on a single dual-mode panoramic map. The distance compensation algorithm, combined with 3D reconstruction of the surface imaging,

could be used not only for quantification of lesion intensity, but also for spatial calibration for determining size of lesions.

In the 2nd aim, a body of work was developed to provide solutions to the spectral overlap (cross-talk) issue, which is a major growing problem in the field of multi-color/multi-spectral fluorescence imaging. To attain the goal of separating emission overlapped fluorescence species for quantitative molecular imaging, three different solutions were developed and compared initially on the realistic phantom using the SFE at real-time (30Hz). This was to the best of our knowledge, the first time that such solutions were developed and demonstrated in real-time for wide-field multicolor fluorescence endoscope system. Furthermore, the 2nd and 3rd solution: Cross-talk Ratio Subtraction algorithm and Sequential Imaging were implemented in a newly developed multispectral fluorescence-reflectance SFE system for in human application as part of the BETRNet project. Although this BETRNet system is limited to 3 channels, the total number channels can be extended to above 10 for the SFE technology with modifications in hardware and software.

The final aim focused on providing clinical tools for increasing detection sensitivity and contrast ratio in disease diagnosis using multi-spectral fluorescence molecular endoscopic imaging. Detection sensitivity limited by the tissue background AF has been one of the biggest problems for the clinical applications of molecular endoscopy using exogenous probes, and no real-time approach was reported. To overcome this challenge, a tissue AF and specular reflection mitigation algorithm was developed and demonstrated at video rates (30Hz) using a newly developed wide-field multispectral fluorescence SFE, with a significantly enhanced target-to-background ratio (>80), and quantitative fluorescence molecular endoscopic imaging with nanomolar detection sensitivity on a tissue phantom. Meanwhile, using *ex vivo* tissue, this work also presented a novel method to evaluate the fluorescence detection sensitivity of an imaging device through quantitative conversion of the tissue AF to the equivalent fluorophore concentration of the target

across the visible and NIR spectra. Finally, the real-time AF mitigation algorithm was implemented on a multispectral SFE system and will be used for the BETRNet human subject study.

Techniques developed in this dissertation was initially for the early stage detection and image-guided biopsies of HGD lesions in Barrett's esophagus, but same technologies developed can also be transferred to the diagnosis and/or intervention in other parts of the body, such as oral tissue, dental cavities, respiratory system, bile duct, fallopian tube, bladder, and minimally invasive image-guided surgery, using an ultrathin and flexible endoscope. Meanwhile, these methodologies could be extended to apply outside medical procedures, as endoscopes are also used in a variety of other areas, such as inspection of airplane turbines, car engines, ship tanks, pipes in buildings or industrial machinery, as well as for veterinary endoscopy.

In summary, technologies have been developed on an ultrathin flexible endoscope system to achieve quantitative, high-contrast and artifact-free multispectral fluorescence-reflectance imaging with high detection sensitivity at nanomolar range. These new algorithms and methodologies utilized the unique hardware feature that concurrent laser excitation and multi-channel fluorescence detection with all channels in spatial registration. However, the SFE technology is highly versatile and can provide many more channels of imaging information than the concurrent one reflectance channel and three fluorescence channels. The dissertation established foundations for the upcoming in human testing, in which a variety of fluorophore conjugated probe combinations from visible to NIR emission range will be evaluated. Meanwhile, this dissertation work also led the development of advanced medical endoscopy into quantitative, data-driven, and computer-aided supporting system, which will ultimately improve disease diagnostic accuracy and reduce mortality rate at point of care.

8. References

[1] K. L. Wang, T.-T. Wu, I. S. Choi, H. Wang, E. Reseetkova, A. M. Correa, W. L. Hofstetter, S. G. Swisher, J. A. Ajani, A. Rashid and C. T. Albarracin, "Expression of Epidermal Growth Factor Receptor in Esophageal and Esophagogastric Junction Adenocarcinomas Association With Poor Outcome," *Cancer,* vol. 109, no. 4, pp. 658-667, 2007.

[2] M. Solaymani-Dodaran, R. Logan, J. West, T. Card and C. Coupland, "Risk of oesophageal cancer in Barrett's oesophagus and gastro-oesophageal reflux," *Gut,* vol. 53, no. 8, pp. 1070-1074, 2004.

[3] X. Duan, B. Joshi, E. Rabinsky, C. Yang, E. J. Seibel, D. K. Turgeon and T. D. Wang, "Image quantification for widefield molecular endoscopy to detect esophageal neoplasia," in *SPIE Photonics West Endoscopic Microscopy IX, Paper 8927-15*, San Francisco, CA, 2014.

[4] S. F. Elahi and T. D. Wang, "Future and advances in endoscopy," *J. Biophotonics,* vol. 4, pp. 471-481, 2011.

[5] M. Goetz and T. D. Wang, "Molecular Imaging in Gastrointestinal Endoscopy," *Gastroenterology,* vol. 138, pp. 828-833, 2010.

[6] B. C. Wilson, "Detection and treatment of dysplasia in Barrett's esophagus: a pivotal challenge in translating biophotonics from bench to bedside," *Journal of Biomedical Optics,* vol. 12, no. 5, p. 051401, 2007.

[7] M. H. Lee, K. Butterbaugh, R. Richards-Kortum and S. Anandasabapath, "Advanced Endoscopic Imaging for Barrett's Esophagus: Current Options and Future Directions," *Curr Gastroenterol Rep,* vol. 14, pp. 216-225, 2012.

[8] S. J. Miller, C. M. Lee, B. P. Joshi, A. Gaustad, E. J. Seibel and T. D. Wang, "Targeted detection of murine colonic dysplasia in vivo with flexible multispectral scanning fiber endoscopy," *Journal of Biomedical Optics,* vol. 17, pp. 021-103, 2012.

[9] P.-L. Hsiung, J. Hardy, S. Friedland, R. Soetikno, C. B. Du, A. P. Wu, P. Sahbaie, J. M. Crawford, A. W. Lowe, C. H. Contag and T. D. Wang, "Detection of colonic dysplasia in vivo using a targeted heptapeptide and confocal microendoscopy," *Nature Medicine,* vol. 14, no. 4, pp. 454-458, 2008.

[10] E. L. Bird-Lieberman, A. A. Neves, P. Lao-Sirieix, M. O'Donovan, M. Novelli, L. B. Lovat, W. S. Eng, L. K. Mahal, K. M. Brindle and R. C. Fitzgerald, "Molecular imaging using fluorescent lectins permits rapid endoscopic identification of dysplasia in Barrett's esophagus," *nature medicine,* vol. 18, no. 2, pp. 315-322, 2012.

[11] R. Upadhyay, R. A. Sheth, R. Weissleder and U. Mahmood, "Quantitative Real-time Catheter-based Fluorescence Molecular Imaging in Mice," *Radiology,* vol. 245, pp. 523-531, 2007.

[12] P. L. Choyke, "Science to Practice: Is It Possible to Quantify Fluorescence during Optical Endoscopy?," *Radiology,* vol. 245, pp. 307-308, 2007.

[13] M. Li and T. D. Wang, "Targeted Endoscopic Imaging," *Gastrointest Endosc Clin N Am.,* vol. 19, no. 2, pp. 283-298, 2009.

[14] M. LI, C. P. ANASTASSIADES, B. JOSHI, C. M. KOMARCK, C. PIRAKA, B. J. ELMUNZER, D. K. TURGEON, T. D. JOHNSON, H. APPELMAN, D. G. BEER and T. D. WANG, "Affinity Peptide for Targeted Detection of Dysplasia in Barrett's Esophagus," *Gastroenterology,* vol. 139, no. 5, pp. 1472-1480, 2010.

[15] B. W. Pogue and M. S. Patterson, "Review of tissue simulating phantoms for optical spectroscopy, imaging and dosimetry," *Journal of Biomedical Optics,* vol. 11, no. 4, p. 041102, 2006.

[16] M. Lualdi, A. Colombo, B. Farina, S. Tomatis and R. Marchesini, "A Phantom With Tissue-Like Optical Properties in the Visible and Near Infrared for Use in Photomedicine," *Lasers in Surgery and Medicine,* vol. 28, pp. 237-243, 2001.

[17] U. J. Netz, J. Toelsner and U. Bindig, "Calibration standards and phantoms for fluorescence optical measurements," *Medical Laser Application,* vol. 26, pp. 101-108, 2011.

[18] D. M. de Bruin, R. H. Bremmer, V. M. Kodach, R. de Kinkelder, J. van Marle, T. G. van Leeuwen and D. J. Faber, "Optical phantoms of varying geometry based on thin building blocks with controlled optical properties," *Journal of Biomedical Optics,* vol. 15, no. 2, p. 025001, 2010.

[19] T. T. Nguyen, H. N. Le, M. Vo, Z. Wang, L. Luu and J. C. Ramella-Roman, "Three-dimensional phantoms for curvature correction in spatial frequency domain imaging," *BIOMEDICAL OPTICS EXPRESS,* vol. 3, pp. 1200-1214, 2012.

[20] R. Bays, G. Wagnières, D. Robert, J.-F. Theumann, A. Vitkin, J.-F. Savary, P. Monnier and H. van den Bergh, "Three-Dimensional Optical Phantom and Its Application in Photodynamic Therapy," *Lasers in Surgery and Medicine,* vol. 21, pp. 227-234, 1997.

[21] H. Kang, M. L. Clarke, S. H. De Paoli Lacerda, A. Karim, L. F. Pease III and J. Hwang, "Multimodal optical studies of single and clustered colloidal quantum dots for the longterm optical property evaluation of quantum dot-based molecular imaging phantoms," *BIOMEDICAL OPTICS EXPRESS,* vol. 3, pp. 1312-1325, 2012.

[22] M. Roy, A. Kim, F. Dadani and B. C. Wilson, "Homogenized tissue phantoms for quantitative evaluation of subsurface fluorescence contrast," *Journal of Biomedical Optics,* vol. 16, p. 016013, 2011.

[23] K. Sokolov, J. Galvan, A. Myakov, A. Lacy, R. Lotan and R. Richards-Kortum, "Realistic three-dimensional epithelial tissue phantoms for biomedical optics," *Journal of Biomedical Optics,* vol. 7, no. 1, pp. 148-156, 2002.

[24] B. P. Joshi and T. D. Wang, "Exogenous Molecular Probes for Targeted Imaging in Cancer: Focus on Multi-modal Imaging," *Cancers,* vol. 2, pp. 1251-1287, 2010.

[25] "www.silpak.com".

[26] M. L. Lesiecki and J. M. Drake, "Use of the thermal lens technique to measure the luminescent quantum yields of dyes in PMMA for luminescent solar concentrators," *APPLIED OPTICS,* pp. 557-560, 1982.

[27] M. Lambropoulos, "FLUOROL 7GA: AN EFFICIENT YELLOW-GREEN DYE FOR FLASHLAMP-PUMPED LASERS," *OPTICS COMMUNICATIONS,* pp. 35-37, 1975.

[28] T. D. Wang, *University of Michigan, Private Conversation.*

[29] L. Zhang, L. Y. Nelson and E. J. Seibel, "Red-shifted fluorescence of sound dental hard tissue," *Journal of Biomedical Optics,* vol. 16, no. 7, p. 071411, 2011.

[30] C. M. Lee, C. J. Engelbrecht, T. D. Soper, F. Helmchen and E. J. Seibel, "Scanning fiber endoscopy with highly flexible, 1 mm catheterscopes for wide-field, full-color imaging," *J. Biophoton.,* vol. 3, no. No. 5-6, pp. 385-407, 2010.

[31] I. Georgakoudi, B. C. Jacobson, J. van Dam, V. Backman, M. B. Wallace, M. G. Müller, Q. Zhang, K. Badizadegan, D. Sun, G. A. Thomas, L. T. Perelman and M. S. Feld, "Fluorescence, Reflectance, and Light-Scattering Spectroscopy for Evaluating Dysplasia in Patients With Barrett's Esophagus," *GASTROENTEROLOGY,* vol. 120, p. 1620–1629, 2001.

[32] I. Georgakoudi, "The color of cancer," *Journal of Luminescence,* Vols. 119-120, p. 75–83, 2006.

[33] S. Rajendra and P. Sharma, "Barrett's Esophagus and Cancer Risk: A More Realistic Estimate," *Seminars in Thoracic and Cardiovascular Surgery,* vol. 23, no. 4, pp. 261-262, 2011.

[34] R. S. Berns, Billmeyer and Saltzman's Principles of Color Technology, 3rd Edition, 2000.

[35] S. Ottestad, O. Sørheim, K. Heia, J. Skaret and J. Petter Wold, "Effects of Storage Atmosphere and Heme State on the Color and Visible Reflectance Spectra of Salmon (Salmo salar) Fillets," *J. Agric. Food Chem.,* vol. 59, pp. 7825-7831, 2011.

[36] Excelitas Cermax Xenon Lamps http://www.excelitas.com/Downloads/Cermax_Eng_Guide.pdf.

[37] D. C. de Veld, M. Skurichina, M. J. Witjes, R. P. Duin, H. J. Sterenborg and J. L. Roodenburg, "Autofluorescence and Diffuse Reflectance Spectroscopy for Oral Oncology.," *Lasers Surg Med.,* vol. 36, no. 5, pp. 356-364, 2005.

[38] Y. Ti and W.-C. Lin, "Effects of probe contact pressure on in vivo optical spectroscopy," *OPTICS EXPRESS,* vol. 16, no. 6, pp. 4250-4262, 2008.

[39] S. Ruderman, A. J. Gomes, V. Stoyneva, J. D. Rogers, A. J. Fought, B. D. Jovanovic and V. Backman, "Analysis of pressure, angle and temporal effects on tissue optical properties from polarizationgated spectroscopic probe measurements," *BIOMEDICAL OPTICS EXPRESS,* vol. 1, no. 2, pp. 489-499, 2010.

[40] R. Reif, M. S. Amorosino, K. W. Calabro, O. A'Amar, S. K. Singh and I. J. Bigio, "Analysis of changes in reflectance measurements on biological tissues subjeced to different probe pressures," *Journal of Biomedical Optics,* vol. 13, no. 1, p. 010502, 2008.

[41] K. Gono, T. Obi, M. Yamaguchi, N. Ohyama, H. Machida, Y. Sano, S. Yoshida, Y. Hamamoto and T. Endo, "Appearance of enhanced tissue features in narrow-band endoscopic imaging," *Journal of Biomedical Optics,* vol. 9, no. 3, p. 568–577, 2004.

[42] B. Li and M. Q.-H. Meng, "Computer-based detection of bleeding and ulcer in wireless capsule endoscopy images by chromaticity moments," *Computers in Biology and Medicine,* vol. 39, pp. 141-147, 2009.

[43] S. Kodashima and M. Fujishiro, "Novel image-enhanced endoscopy with i-scan technology," *World J Gastroenterol,* vol. 16, no. 9, pp. 1043-1049, 2010.

[44] C. K. Lee, S.-H. Lee and Y. Hwangbo, "Narrow-band imaging versus I-Scan for the real-time histological prediction of diminutive colonic polyps: a prospective comparative study by using the simple unified endoscopic classification," *GASTROINTESTINAL ENDOSCOPY,* vol. 74, no. 3, pp. 603-609, 2011.

[45] E. J. Seibel, T. A. Brentnall and J. A. Dominitz, "New endoscopic and cytologic tools for cancer surveillance in the digestive tract," *Gastrointest Endoscopy Clin N Am,* vol. 19, pp. 299-307, 2009.

[46] L. A. Herrero, B. L. Weusten and J. J. Bergman, "Autofluorescence and Narrow Band Imaging in Barrett's Esophagus," *Gastroenterol Clin N Am,* vol. 39, p. 747–758, 2010.

[47] E. Edell, S. Lam, H. Pass, Y. E. Miller, T. Sutedja, T. Kennedy, G. Loewen and R. L. Keith, "Detection and Localization of Intraepithelial Neoplasia and Invasive Carcinoma Using Fluorescence-Reflectance Bronchoscopy An International, Multicenter Clinical Trial," *Journal of Thoracic Oncology,* vol. 4, no. 1, pp. 49-54, 2009.

[48] M. Kara, R. S. DaCosta, B. C. Wilson, N. E. Marcon and J. Bergman, "Autofluorescence-Based Detection of Early Neoplasia in Patients with Barrett's Esophagus," *Digestive Diseases,* vol. 22, pp. 134-141, 2004.

[49] B. Lin, S. Urayama, R. M. Saroufeem, D. L. Matthews and S. G. Demos, "Characterizing the origin of autofluorescence in human esophageal epithelium under ultraviolet excitation," *OPTICS EXPRESS,* vol. 18, no. 20, pp. 21074-21082, 2010.

[50] N. D. Kirkpatrick, J. B. Hoying, S. K. Botting, J. A. Weiss and U. Utzinger, "In vitro model for endogenous optical signatures of collagen," *Journal of Biomedical Optics,* vol. 11, no. 5, p. 054021, 2006.

[51] R. S. DaCosta, H. Andersson and B. C. Wilson, "Molecular Fluorescence Excitation–Emission Matrices Relevant to Tissue Spectroscopy," *Photochemistry and Photobiology,* vol. 78, no. 4, pp. 384-392, 2003.

[52] L. Coghlan, U. Utzinger, R. Drezek, D. Heintzelman, A. Zuluga, C. Brookner, R. Richards-Kortum, I. Gimenez-Couti and M. Follen, "Optimal fluorescence excitation wavelengths for detection of squamous intra-epithelial neoplasia: results from an animal model," *OPTICS EXPRESS,* vol. 7, no. 12, pp. 436-446, 2000.

[53] W. Zheng, W. Lau, C. Cheng, K. C. Soo and M. Olivo, "OPTIMAL EXCITATION-EMISSION WAVELENGTHS FOR AUTOFLUORESCENCE DIAGNOSIS OF BLADDER TUMORS," *Int. J. Cancer,* vol. 104, pp. 477-481, 2003.

[54] R. S. DaCosta, B. C. Wilson and N. E. Marcon, "Spectroscopy and fluorescence in esophageal diseases," *Best Practice & Research Clinical Gastroenterology,* vol. 20, no. 1, pp. 41-57, 2006.

[55] J. Cronin, E. McAdam, A. Danikas, C. Tselepis, P. Griffiths, J. Baxter, L. Thomas, J. Manson and G. Jenkins, "Epidermal Growth Factor Receptor (EGFR) Is Overexpressed in High-Grade Dysplasia and

Adenocarcinoma of the Esophagus and May Represent a Biomarker of Histological Progression in Barrett ' s Esophagus (BE)," *Am J Gastroenterol,* vol. 106, p. 46–56, 2011.

[56] S. Yentz and T. D. Wang, "Molecular Imaging for Guiding Oncologic Prognosis and Therapy in Esophageal Adenocarcinoma," *Hosp Pract (Minneap).,* vol. 39, no. 2, pp. 97-106, 2011.

[57] B. J. Reid, D. S. Levine, G. Longton, P. L. Blount and P. S. Rabinovitch, "Predictors of Progression to Cancer in Barrett's Esophagus: Baseline Histology and Flow Cytometry Identify Low- and High-Risk Patient Subsets," *Am J Gastroenterol ,* vol. 95, pp. 1669-1676 , 2000.

[58] E. J. Seibel, R. E. Carroll, J. A. Dominitz, R. S. Johnston, C. D. Melville, C. M. Lee, S. M. Seitz and M. B. Kimmey, "Tethered Capsule Endoscopy, A Low-Cost and High-Performance Alternative Technology for the Screening of Esophageal Cancer," *IEEE TRANSACTIONS ON BIOMEDICAL ENGINEERING,* vol. 55, no. 3, pp. 1032-1042, 2008.

[59] R. Szeliski, "Image Alignment and Stitching: A Tutorial," *Foundations and Trends in Computer Graphics and Vision,* vol. 2, no. 1, pp. 1-104, 2006.

[60] T. D. Soper, M. P. Porter and E. J. Seibel, "Surface Mosaics of the Bladder Reconstructed From Endoscopic Video for Automated Surveillance," *IEEE TRANSACTIONS ON BIOMEDICAL ENGINEERING,* vol. 59, no. 6, pp. 1670-1680, 2012.

[61] P.-L. Hsiung, J. Hardy, S. Friedland, R. Soetikno, C. B. Du, A. P. Wu, P. Sahbaie, J. M. Crawford, A. W. Lowe, C. H. Contag and T. D. Wang, "Detection of colonic dysplasia in vivo using a targeted heptapeptide and confocal microendoscopy," *Nature Medicine,* vol. 14, no. 4, pp. 454-458, 2008.

[62] E. L. Bird-Lieberman, A. A. Neves, P. Lao-Sirieix, M. O'Donovan, M. Novelli, L. B. Lovat, W. S. Eng, L. K. Mahal, K. M. Brindle and R. C. Fitzgerald, "Molecular imaging using fluorescent lectins permits rapid endoscopic identification of dysplasia in Barrett's esophagus," *Nature Medicine,* vol. 18, no. 2, pp. 315-322, 2012.

[63] E. J. Seibel, T. D. Soper, M. R. Burkhardt, M. P. Porter and W. J. Yoon, "Multimodal flexible cystoscopy for creating co-registered panoramas of the bladder urothelium," *Proceedings of SPIE ,* vol. 8207, p. 82071A, 2012.

[64] E. J. Seibel, J. A. Jo, C. D. Meiville, R. S. Johnston, C. R. Naumann and M. D. Saunders, "Image-guided intervention in the human bile duct using scanning fiber endoscope system," in *SPIE Proceedings Optical Fibers and Sensors for Medical Diagnostics and Treatment Applications XII*, San Francisco, California, 2012.

[65] L. Zhang, L. Y. Nelson and E. J. Seibel, "Spectrally enhanced imaging of occlusal surfaces and artificial shallow enamel erosions with a scanning fiber endoscope," *Journal of Biomedical Optics,* vol. 17, no. 7, p. 076019, 2012.

[66] T. D. Soper, D. R. Haynor, R. W. Glenny and E. J. Seibel, "In Vivo Validation of a Hybrid Tracking System for Navigation of an Ultrathin Bronchoscope Within Peripheral Airways," *IEEE TRANSACTIONS ON BIOMEDICAL ENGINEERING,* vol. 57, no. 3, pp. 736-745, 2010.

[67] C. Yang, V. Hou, L. Y. Nelson and E. J. Seibel, "Color-matched and fluorescence-labeled esophagus phantom and its applications," *Journal of Biomedical Optics,* vol. 18, no. 2, p. 026020, 2013.

[68] B. Rousso, S. Peleg, I. Finci and A. Rav-Acha, "Universal mosaicing using pipe projection," in *in Proceeding of International Conference on Computer Vision (ICCV)*, 1998, pp.945-952.

[69] S. Baker and I. Matthews, "Lucas-Kanade 20 Years On: A Unifying Framework," *International Journal of Computer Vision - IJCV,* vol. 56, no. 3, pp. 221-255, 2004.

[70] J. P. Lewis, "Fast Normalized Cross-Correlation," *Industrial Light & Magic.*

[71] R. M. Haralick and L. G. Shapiro, Computer and Robot Vision, Volume II, vol. Volume II, Addison-Wesley, 1992, pp. 316-317..

[72] J. V. Frangioni, "New Technologies for Human Cancer Imaging," *J Clin Oncol,* vol. 26, pp. 4012-4021, 2008.

[73] M. C. Pierce, D. J. Javier and R. Richards-Kortum, "Optical contrast agents and imaging systems for detection and diagnosis of cancer," *Int. J. Cancer,* vol. 123, p. 1979–1990, 2008.

[74] M. Goetz and T. D. Wang, "Molecular Imaging in Gastrointestinal Endoscopy," *GASTROENTEROLOGY,* vol. 138, pp. 828-833, 2010.

[75] G. M. van Dam, G. Themelis, L. M. A. Crane and et. al., "Intraoperative tumor-specific fluorescence imaging in ovarian cancer by folate receptor-α targeting: first in-human results," *Nature Medicine,* vol. 17, no. 10, pp. 1315-1319, 2011.

[76] M. Kriegmair, R. Baumgartner, R. Knuchel, H. Stepp, F. Hofstadter and A. Hofsteter, "Detection OF Early Bladder Cancer By 5-Aminolevulnic Acid Induced Porphyrin Fluorescence," *The Journal of Urology,* vol. 155, pp. 105-110, 1996.

[77] M. R. Stroud, S. J. Hansen and J. M. Olson, "In Vivo Bio-imaging Using Chlorotoxin-based Conjugates," *Curr Pharm Des.,* vol. 17, no. 38, p. 4362–4371, 2011.

[78] A. Hellebust and R. Richards-Kortum, "Advances in molecular imaging: targeted optical contrast agents for cancer diagnostics," *Nanomedicine,* vol. 7, no. 3, p. 429–445, 2012.

[79] K. J. Rosbach, M. D. Williams, A. M. Gillenwater and R. R. Richards-Kortum, "Optical Molecular Imaging of Multiple Biomarkers of Epithelial Neoplasia: Epidermal Growth Factor Receptor Expression and Metabolic Activity in Oral Mucosa," *Translational Oncology,* vol. 5, pp. 160-171, 2012.

[80] S. J. Miller, C. M. Lee, B. P. Joshi, A. Gaustad, E. J. Seibel and T. D. Wang, "Targeted detection of murine colonic dysplasia in vivo with flexible multispectral scanning fiber endoscopy," *Journal of Biomedical Optics,* vol. 17, no. 2, p. 021103, 2012.

[81] R. J. Langsner, L. P. Middleton, J. Sun, F. Meric-Bernstam, K. K. Hunt, R. A. Drezek and T. K. Yu, "Wide-field imaging of fluorescent deoxy-glucose in ex vivo malignant and normal breast tissue," *BIOMEDICAL OPTICS EXPRESS,* vol. 2, no. 6, pp. 1514-1523, 2011.

[82] R. Weissleder, C.-H. Tung, U. Mahmood and A. Bogdanov Jr., "In vivo imaging of tumors with protease-activated near-infrared fluorescent probes," *NATURE BIOTECHNOLOGY,* vol. 17, pp. 375-378, 1999.

[83] Q. T. Nguyen, E. S. Olson, T. A. Aguilera, T. Jiang, M. Scadeng, L. G. Ellies and R. Y. Tsien, "Surgery with molecular fluorescence imaging using activatable cell-penetrating peptides decreases residual cancer and improves survival," *Proceedings of the National Academy of Sciences of the United States of America,* vol. 107, no. 9, pp. 4317-4322, 2010.

[84] R. Anil Sheth, R. Upadhyay, L. Stangenberg, R. Sheth, R. Weissleder and U. Mahmood, "Improved detection of ovarian cancer metastases by intraoperative quantitative fluorescence protease imaging in a pre-clinical model," *Gynecologic Oncology,* vol. 112, pp. 616-622, 2009.

[85] H. Kobayashi, Y. Koyama, T. Barrett, Y. Hama, C. A. Regino, I. S. Shin, B.-S. Jang, N. Le, C. H. Nhat, P. L. Choyke and Y. Urano, "Multimodal Nanoprobes for Radionuclide and Five-Color Near-Infrared Optical Lymphatic Imaging," *ACS Nano,* vol. 1, no. 4, pp. 258-264, 2007.

[86] H. Kobayashi, M. Ogawa, R. Alford, P. L. Choyke and Y. Urano, "New Strategies for Fluorescent Probe Design in Medical Diagnostic Imaging," *Chem Rev.,* vol. 110, no. 5, p. 2620–2640, 2010.

[87] M. Mitsunaga, N. Kosaka, R. C. Kines and et al., "In Vivo Longitudinal Imaging of Experimental Human Papillomavirus Infection in Mice with a Multicolor Fluorescence Mini-Endoscopy System," *Cancer Prev Res,* vol. 4, pp. 767-773, 2011.

[88] S. F. Elahi and T. D. Wang, "Future and advances in endoscopy," *J. Biophotonics,* vol. 4, no. 7-8, p. 471–481, 2011.

[89] M. Longmire, N. Kosaka, M. Ogawa, P. L. Choyke and H. Kobayashi, "Multi-color in vivo targeted imaging to guide real-time surgery of HER2-positive micrometastases in a two tumor coincident model of ovarian cancer," *Cancer Sci.,* vol. 100, no. 6, p. 1099–1104, 2009.

[90] U. Resch-Genger, M. Grabolle, S. Cavaliere-Jaricot, R. Nitschke and T. Nann, "Quantum dots versus organic dyes as fluorescent labels," *Nature Methods,* vol. 5, no. 9, pp. 763-775, 2008.

[91] M. E. Dickinson, G. Bearman, S. Tille, R. Lansford and S. E. Fraser, "Multi-Spectral Imaging and Linear Unmixing Add a Whole New Dimension to Laser Scanning Fluorescence Microscopy," *BioTechniques,* vol. 31, no. 6, pp. 1272-1278, 2001.

[92] T. Zimmermann, J. Rietdorf and R. Pepperkok, "Spectral imaging and its applications in live cell microscopy," *FEBS Letters,* vol. 546, pp. 87-92, 2003.

[93] T. Zimmermann, "Spectral Imaging and Linear Unmixing in Light Microscopy," *Adv Biochem Engin/Biotechnol,* vol. 95, pp. 245-265, 2005.

[94] J. Ohn, J. Yang, S. E. Fraser, R. Lansford and M. Liebling, "High-Speed Multi-Color Microscopy of Repeating Dynamic Processes," *Genesis.,* vol. 49, no. 7, p. 514–521, 2011.

[95] D. Fu, J. Ma and J. Chen, "Dual-wavelength microarray fluorescence detection system using volume holographic filter," *Journal of Biomedical Optics,* vol. 12, no. 1, p. 014040, 2007.

[96] B. K. Muller, E. Zaychikov, C. Brauchle and D. C. Lamb, "Pulsed Interleaved Excitation," *Biophysical Journal,* vol. 89, p. 3508–3522, 2005.

[97] S. J. Miller, B. P. Joshi, Y. Feng, A. Gaustad, E. R. Fearon and T. D. Wang, "In Vivo Fluorescence-Based Endoscopic Detection of Colon Dysplasia in the Mouse Using a Novel Peptide Probe," *PLoS ONE,* vol. 6, no. 3, p. e17384, 2011.

[98] Z. Liu, S. J. Miller, B. P. Joshi and T. D. Wang, "In vivo targeting of colonic dysplasia on fluorescence endoscopy with near-infrared octapeptide," *Gut,* vol. 62, pp. 395-403, 2012.

[99] M. Al-Kasspooles, J. H. Moore, M. B. Orringer and D. G. Beer, "Amplification and overexpression of the EGFR and erbB2 genes in human esophageal adenocarcinomas," *Int J Cancer,* vol. 54, pp. 213-219, 1993.

[100] B. P. Joshi and T. D. Wang, "Exogenous Molecular Probes for Targeted Imaging in Cancer: Focus on Multi-modal Imaging," *Cancers,* vol. 2, pp. 1251-1287, 2010.

[101] C. Yang, T. D. Soper and E. J. Seibel, "Detecting fluorescence hot-spots using mosaic maps generated from multimodal endoscope imaging," *SPIE Proceedings Endoscopic Microscopy VIII,* p. 8575, 2013.

[102] M. LAMBROPOULOS, "FLUOROL 7GA: AN EFFICIENT YELLOW-GREEN DYE FOR FLASHLAMP-PUMPED LASERS," *OPTICS COMMUNICATIONS,* vol. 15, no. 1, pp. 35-37, 1975.

[103] M. L. Lesiecki and J. . M. Drake, "Use of the thermal lens technique to measure the luminescent quantum yields of dyes in PMMA for luminescent solar concentrators," *APPLIED OPTICS,* vol. 21, no. 3, pp. 557-560, 1982.

[104] D. R. Davydov, N. Y. Davydova and J. R. Halpert, "Allosteric Transitions in Cytochrome P450eryF Explored with Pressure-Perturbation Spectroscopy, Lifetime FRET, and a Novel Fluorescent Substrate, Fluorol-7GA," *Biochemistry,* vol. 47, p. 11348–11359, 2008.

[105] J. B. Prieto, F. L. Arbeloa, V. M. Martinez, T. A. Lopez and I. L. Arbeloa, "Photophysical Properties of the Pyrromethene 597 Dye: Solvent Effect," *J. Phys. Chem.,* vol. 108, no. 26, pp. 5504-5508, 2004.

[106] T. Susdorf, D. Del agua, A. Tyagi, A. Penzkofer, O. Garcıa, R. Sastre, A. Costela and I. Garcıa-moreno, "Photophysical characterization of pyrromethene 597 laser dye in silicon-containing organic matrices," *Appl. Phys.,* vol. B86, p. 537–545, 2007.

[107] C. M. Lee, C. J. Engelbrecht, T. D. Soper, F. Helmchen and E. J. Seibel, "Scanning fiber endoscopy with highly flexible, 1 mm catheterscopes for wide-field, full-color imaging," *J. Biophoton.,* vol. 3, no. 5-6, p. 385–407, 2010.

[108] R. Szeliski, "Computer Vision: Algorithms and Applications," Springer, 2010, pp. 430-463.

[109] G. A. Prasad, A. Bansal, P. Sharma and K. K. Wang, "Predictors of Progression in Barrett's Esophagus: Current Knowledge and Future Directions," *The American Journal of Gastroenterology,* vol. 105, pp. 1490-1502, 2010.

[110] J. T. C. Liu, M. W. Helms, M. J. Mandella, J. M. Crawford, G. S. Kino and C. H. Contag, "Quantifying Cell-Surface Biomarker Expression in Thick Tissues with Ratiometric Three-Dimensional Microscopy," *Biophysical Journal,* vol. 96, p. 2405–2414, 2009.

[111] D. Wang, Y. Chen, S. Y. Leigh, H. Haeberle, C. H. Contag and J. T. Liu, "Microscopic Delineation of Medulloblastoma Margins in a Transgenic Mouse Model Using a Topically Applied VEGFR-1 Probe," *Translational Oncology,* vol. 5, no. 6, p. 408–414, 2012.

[112] M. Kara, R. DaCosta, B. C. Wilson, N. E. Marcon and J. Bergman, "Autofluorescence-Based Detection of Early Neoplasia in Patients with Barrett's Esophagus," *Digestive Diseases,* vol. 22, pp. 134-141, 2004.

[113] B. Lin, S. Urayama, R. M. Saroufeem and et. al., "Characterizing the origin of autofluorescence in human esophageal epithelium under ultraviolet excitation," *OPTICS EXPRESS,* vol. 18, no. 20, pp. 21074-21082, 2010.

[114] B. Banerjee, T. Renkoski, L. R. Graves and et. al., "Tryptophan autofluorescence imaging of neoplasms of the human colon," *Journal of Biomedical Optics,* vol. 17, no. 1, p. 016003, 2012.

[115] Y. Sun, H. Yu, D. Zheng, Q. Cao, Y. Wang, D. Harris and Y. Wang, "Sudan Black B Reduces Autofluorescence in Murine Renal Tissue," *Arch Pathol Lab Med,* vol. 135, pp. 1335-1342, 2011.

[116] A. E. Profio, O. J. Balchum and F. Carstens, "Digital background subtraction for fluorescence imaging," *Med. Phys.,* vol. 13, no. 5, pp. 717-721, 1986.

[117] P. E. I. "IVIS 200 Pre-clinical In Vivo Imaging System | Perkin Elmer," 1998-2003. [Online]. Available: http://www.perkinelmer.com/Catalog/Product/ID/IVIS200. [Accessed July 2013].

[118] R. Alford, H. M. Simpson, J. Duberman, G. C. Hill, M. Ogawa, C. Regino, H. Kobayashi and P. L. Choyke, "Toxicity of Organic Fluorophores Used in Molecular Imaging: Literature Review," *Molecular Imaging,* vol. 8, no. 6, p. 341–354, 2009.

[119] V. J. Pansare, S. Hejazi, W. J. Faenza and R. K. Prud'homme, "Review of Long-Wavelength Optical and NIR Imaging Materials: Contrast Agents, Fluorophores, and Multifunctional Nano Carriers," *Chem. Mater.,* vol. 24, pp. 812-827, 2012.

[120] X. Wang, S. Bhaumik, Q. Li, V. P. Staudinger and S. Yazdanfar, "Compact instrument for fluorescence image-guided surgery," *Journal of Biomedical Optics | Letters,* vol. 15, no. 2, p. 020509, 2010.

[121] D. Wirth, M. Snuderl, S. Sheth, C.-S. Kwon, M. P. Frosch, W. Curry and A. N. Yaroslavsky, "Identifying brain neoplasms using dye-enhanced multimodal confocal imaging," *Journal of Biomedical Optics,* vol. 17, no. 2, p. 026012, 2012.

[122] Y. Ashitate, C. S. Vooght, M. Hutteman, R. Oketokoun, H. S. Choi and J. V. Frangioni, "Simultaneous Assessment of Luminal Integrity and Vascular Perfusion of the Gastrointestinal Tract using Dual-Channel Near-Infrared Fluorescence," *Molecular Imaging,* vol. 11, no. 4, pp. 301-308, 2012.

[123] H. S. Choi, S. L. Gibbs, J. H. Lee, S. H. Kim, Y. Ashitate, F. Liu, H. Hyun, G. Park, Y. Xie, S. Bae, M. Henary and J. V. Frangioni, "Targeted zwitterionic near-infrared fluorophores for improved optical imaging," *Nature Biotechnology,* vol. 31, p. 148–153, 2013.

[124] V. B. Rodriguez, S. M. Henry, A. S. Hoffman, P. S. Stayton, X. Li and S. H. Pun, "Encapsulation and stabilization of indocyanine green within poly(styrene-alt-maleic anhydride) blockpoly(styrene) micelles for near-infrared imaging," *Journal of Biomedical Optics,* vol. 13, no. 1, p. 014025, 2008.

[125] "Barrett's Esophagus Translational Research Network (BETRNet)-Imaging Agents," [Online]. Available: http://sitemaker.umich.edu/betrnet/imaging_agents. [Accessed May 2013].

[126] G. Zacharakis, R. Favicchio, M. Simantiraki and J. Ripoll, "Spectroscopic detection improves multi-color quantification in fluorescence tomography," *BIOMEDICAL OPTICS EXPRESS,* vol. 2, no. 3, pp. 431-439, 2011.

[127] R. Pepperkok, A. Squire, S. Geley and P. I. Bastiaens, "Simultaneous detection of multiple green fluorescent proteins in live cells by fluorescence lifetime imaging microscopy," *Current Biology,* vol. 9, p. 269–272, 1999.

[128] L. Marcu, "Fluorescence Lifetime Techniques in Medical Applications," *Annals of Biomedical Engineering,* vol. 40, no. 2, p. 304–331, 2012.

[129] E. J. Seibel, J. A. Jo, C. D. Melville and et. al., "Image-guided intervention in the human bile duct using scanning fiber endoscope system," *Proc. of SPIE Optical Fibers and Sensors for Medical Diagnostics and Treatment Applications XI,* vol. 8218, p. 82180B, 2012.

[130] M. Roy, F. Dadani, C. J. Niu, A. Kim and B. C. Wilson, "Effect of tissue optics on wavelength optimization for quantum dot-based surface and subsurface fluorescence imaging," *Journal of Biomedical Optics,* vol. 17, no. 2, p. 026002, 2012.

[131] N. Kosaka, M. Ogawa, N. Sato, P. L. Choyke and H. Kobayashi, "In Vivo Real-Time, Multicolor, Quantum Dot Lymphatic Imaging," *Journal of Investigative Dermatology,* vol. 129, pp. 2818-2822, 2009.

[132] A. M. Smith, S. Dave, S. Nie, L. True and X. Gao, "Multicolor quantum dots for molecular diagnostics of cancer," *Expert Rev. Mol. Diagn.,* vol. 6, no. 2, pp. 231-244, 2006.

[133] E. R. Goldman, A. R. Clapp, G. P. Anderson, H. T. Uyeda, J. M. Mauro, I. L. Medintz and H. Mattoussi, "Multiplexed Toxin Analysis Using Four Colors of Quantum Dot Fluororeagents," *Anal. Chem.,* vol. 76, pp. 684-688, 2004.

[134] M. Goetz and T. D. Wang, "Molecular Imaging in Gastrointestinal Endoscopy," *Gastroenterology,* vol. 138, pp. 828-833, 2010.

[135] B. C. Wilson, "Detection and treatment of dysplasia in Barrett's esophagus: a pivotal challenge in translating biophotonics from bench to bedside," *Journal of Biomedical Optics,* vol. 12, no. 5, p. 051401, 2007.

[136] R. Atreya and M. Goetz, "Molecular imaging in gastroenterology," *Nature Reviews Gastroenterology & Hepatology,* vol. 10, no. 12, pp. 704-712, 2013.

[137] P. J. Pasricha and M. Motamedi, "Optical biopsies, “bioendoscopy,” and why the sky is blue: The coming revolution in gastrointestinal imaging," *Gastroenterology,* vol. 122, no. 2, pp. 571-575, 2002.

[138] M. B. Sturm, B. P. Joshi, S. Lu and et al., "Targeted Imaging of Esophageal Neoplasia with a Fluorescently Labeled Peptide: First-in-Human Results," *Science Translational Medicine,* vol. 5, no. 184, p. 184ra61, 2013.

[139] M. Veiseh, P. Gabikian, S.-B. Bahrami and et. al, "Tumor Paint: A Chlorotoxin:Cy5.5 Bioconjugate for Intraoperative Visualization of Cancer Foci," *Cancer Research,* vol. 67, no. 14, pp. 6882-6888, 2007.

[140] M. Kriegmair, R. Baumgartner, R. Knuchel, H. Stepp, F. Hofstadter and A. Hofsteter, "Detection of early bladder cancer by 5-aminolevulinic acid induced porphyrin fluorescence," *The Journal of Urology,* vol. 155, no. 1, pp. 105-110, 1996.

[141] G. M. van Dam, G. Themelis, L. M. Crane, N. J. Harlaar, R. G. Pleijhuis, W. Kelder, A. Sarantopoulos, J. S. de Jong, H. J. G Arts, A. G. J. van der Zee, J. Bart, P. S. Low and V. Ntziachristos, "Intraoperative tumor-specific fluorescence imaging in ovarian cancer by folate receptor-α targeting: first in-human results," *Nature Medicine,* vol. 17, no. 10, pp. 1315-1319, 2011.

[142] M. S. Hoetker and M. Goetz, "Molecular imaging in endoscopy," *United European Gastroenterology Journal,* vol. 1, no. 2, pp. 84-92, 2013.

[143] R. S. DaCosta, B. C. Wilson and N. E. Marcon, "Spectroscopy and fluorescence in esophageal," *Best Practice & Research Clinical Gastroenterology,* vol. 20, no. 1, pp. 41-57, 2006.

[144] R. Y. Tsien, L. Ernst and A. Waggoner, "Fluorophores for Confocal Microscopy: Photophysics and Photochemistry," in *Handbook Of Biological Confocal Microscopy*, Springer US, 2006, pp. 338-352.

[145] M. S. T. Goncalves, "Fluorescent Labeling of Biomolecules with Organic Probes," *Chemical Reviews,* vol. 109, no. 1, pp. 190-212, 2009.

[146] R. Y. Tsien, "Fluorescent indicators of ion concentrations," in *Methods in Cell Biology, Volume 30*, Academic Press, 1989, pp. 127-156.

[147] Q. T. Nguyen and R. Y. Tsien, "Fluorescence-guided surgery with live molecular navigation — a new live cutting edge," *Nature Reviews,* vol. 13, no. 9, pp. 653-662, 2013.

[148] R. Weissleder and M. J. Pittet, "Imaging in the era of molecular oncology," *Nature,* vol. 452, no. 4, pp. 580-589 , 2008.

[149] J. Gao, P. Wang and R. W. Giese, "Xanthamide Fluorescent Dyes," *Analytical Chemistry,* vol. 74, no. 24, pp. 6397-6401, 2002.

[150] O. N. Burchak, L. Mugherli, F. Chatelain and M. Y. Balakirev, "Fluorescein-based amino acids for solid phase synthesis of fluorogenic protease substrates," *Bioorganic & Medicinal Chemistry,* vol. 14, no. 8, pp. 2559-2568, 2006.

[151] V. Venugopal, M. Park, Y. Ashitate, F. Neacsu, F. Kettenring, J. V. Frangioni, S. P. Gangadharan and S. Gioux, "Design and characterization of an optimized simultaneous color and near-infrared fluorescence rigid endoscopic imaging system," *Journal of Biomedical Optics,* vol. 18, no. 12, p. 126018, 2013.

[152] A. Bogaards, H. Sterenborg and B. C. Wilson, "In vivo quantification of fluorescent molecular markers in real-time: A review to evaluate the performance of five existing methods," *Photodiagnosis and Photodynamic Therapy,* vol. 4, no. 4, p. 170—178, 2007.

[153] R. Baumgartner, H. Fisslinger, D. Jocham, H. Lenz, L. Ruprecht, H. Stepp and E. Unsold, "A Fluorescence Imaging Device for Endoscopic Detection of Early Stage Cancer - Instrumental and Experimental Studies," *Photochemistry and Photobiology,* vol. 46, no. 5, pp. 759-763, 1987.

[154] T. Troy, D. Jekic-McMullen, L. Sambucetti and B. Rice, "Quantitative comparison of the sensitivity of detection of fluorescent and bioluminescent reporters in animal models.," *Molecular Imaging,* vol. 3, no. 1, pp. 9-23, 2004.

[155] P. B. Garcia-Allende, J. Glatz, M. Koch, J. J. Maximilian, E. Hartmans, A. G. T. van Scheltinga, P. Symvoulidis, G. M. van Dam, W. B. Nagengast and V. Nagengast, "Towards clinically translatable NIR fluorescence molecular guidance for colonoscopy," *Biomedical Optics Express,* vol. 5, no. 1, pp. 78-92, 2014.

[156] F. Fantoni, L. Hervé, V. Poher, S. Gioux, J. I. Mars and J.-M. Dinten, "Background fluorescence reduction and absorption correction for fluorescence reflectance imaging," in *SPIE Photonics West Advanced Biomedical and Clinical Diagnostic and Surgical Guidance Systems XII, paper 8935-34*, San Francisco, 2014.

[157] R. A. Sheth, L. Josephson and U. Mahmood, "Evaluation and clinically relevant applications of a fluorescent imaging analog to fluorodeoxyglucose positron emission tomography," *Journal of Biomedical Optics,* vol. 14, no. 6, p. 064014, 2009.

[158] N. Thekkek, D. M. Maru, A. D. Polydorides, M. S. Bhutani, S. Anandasabapathy and R. Richards-Kortum, "Pre-Clinical Evaluation of Fluorescent Deoxyglucose as a Topical Contrast Agent for the Detection of Barrett's-Associated Neoplasia During Confocal Imaging," *Technology in Cancer Research and Treatment,* vol. 10, no. 5, pp. 431-441, 2011.

[159] N. Nitin, A. L. Carlson, T. Muldoon, A. K. El-Naggar, A. Gillenwater and R. Richards-Kortum, "Molecular imaging of glucose uptake in oral neoplasia following topical application of fluorescently labeled deoxy-glucose," *International Journal of Cancer,* vol. 124, no. 12, p. 2634–2642, 2009.

[160] Y. Liu, R. Njuguna, T. Matthews, W. J. Akers, G. P. Sudlow, S. Mondal, R. Tang, V. Gruev and S. Achilefu, "Near-infrared fluorescence goggle system with complementary metal–oxide–semiconductor imaging sensor and see-through display," *Journal of Biomedical Optics,* vol. 18, no. 10, p. 101303, 2013.

[161] J. Glatz, J. Varga, P. B. Garcia-Allende, M. Koch, F. R. Greten and V. Ntziachristos, "Concurrent video-rate color and near-infrared fluorescence laparoscopy," *Journal of Biomedical Optics,* vol. 18, no. 10, p. 101302, 2013.

[162] C. Azzi, J. Zhang, C. H. Purdon, J. M. Chapman, D. Nitcheva, J. R. Hebert and E. W. Smith, "Permeation and reservoir formation of 4-(methylnitrosamino)-1-(3-pyridyl)-1-butanone (NNK) and benzo[a]pyrene (B[a]P) across porcine esophageal tissue in the presence of ethanol and menthol," *Carcinogenesis,* vol. 27, no. 1, pp. 137-145, 2005.

[163] C. Yang, V. W. Hou, L. Y. Nelson, R. S. Johnston, C. D. Melville and E. J. Seibel, "Scanning Fiber Endoscope with multiple fluorescence-reflectance imaging channels for guiding biopsy," in *SPIE Photonics West Design and Quality for Biomedical Technologies VI, paper 8936-27*, San Francisco, 2014.

[164] V. W. Hou, C. Yang, L. Y. Nelson and E. J. Seibel, "The development of a simplified epithelial tissue phantom for the evaluation of an autofluorescence mitigation algorithm," in *SPIE Photonics West, Design and Performance Validation of Phantoms Used in Conjunction with Optical Measurement of Tissue VI, paper 8945-5*, San Francisco, 2014.

[165] "Coherent Inc. OBIS Galaxy - Laser Beam Combiner," Coherent Inc., 2014. [Online]. Available: http://www.coherent.com/products/?2080/OBIS-Galaxy. [Accessed 14 February 2014].

[166] C. Yang, V. W. Hou, L. Y. Nelson, R. S. Johnston, C. D. Melville and E. J. Seibel, "Multispectral Scanning Fiber Endoscope with concurrent autofluorescence baackground mitigation for improved target-to-background ratio," in *SPIE Photonics West Endoscopic Microscopy IX, paper 8927-18*, San Francisco, 2014.

[167] C. Yang, V. W. Hou, L. Y. Nelson and E. J. Seibel, "Mitigating fluorescence spectral overlap in wide-field endoscopic imaging," *Journal of Biomedical Optics,* vol. 18, no. 8, p. 086012, 2013.

[168] M. A. Kara, R. S. DaCosta, C. J. Streutker, N. E. Marcon, J. J. Bergman and B. C. Wilson, "Characterization of tissue autofluorescence in Barrett's esophagus by confocal fluorescence microscopy," *Diseases of the Esophagus,* vol. 20, pp. 141-150, 2007.

[169] C. H. van de Lest, E. M. Versteeg, J. H. Veerkamp and T. H. van Kuppevelt, "Elimination of Autofluorescence in Immunofluorescence Microscopy with Digital Image Processing," *The Joumal of Histochemistry and Cytochemistry,* vol. 43, no. 7, pp. 727-730, 1995.

[170] M. Zellweger, D. Goujon, R. Conde, M. Forrer, H. van den Bergh and G. Wagnie`res, "Absolute autofluorescence spectra of human healthy, metaplastic, and early cancerous bronchial tissue in vivo," *Applied Optics,* vol. 40, no. 22, pp. 3784-3791, 2001.

[171] H. Chung, H. Jin, J. F. Dempsey, C. Liu, J. Palta, T.-S. Suh and S. Kim, "Evaluation of surface and build-up region dose for intensity-modulated radiation therapy in head and neck cancer," *Medical Physics,* vol. 32, no. 8, pp. 2682-2689, 2005.

[172] S. Prahl, "Optical Absorption of Hemoglobin," SAP, 15 December 1999. [Online]. Available: http://omlc.ogi.edu/spectra/hemoglobin/. [Accessed 30 January 2014].

[173] H. S. Choi, K. Nasr, S. Alyabyev, D. Feith, J. H. Lee, S. H. Kim, Y. Ashitate, H. Hyun, G. Patonay, L. Strekowski, M. Henary and J. V. Frangioni, "Synthesis and In Vivo Fate of Zwitterionic Near-Infrared Fluorophores," *Angewandte Chemie International Edition English,* vol. 50, no. 28, p. 6258–6263, 2011.

[174] C. Wu, "3D Reconstruction of Anatomical Structures from Endoscopic Images, doctoral dissertation, tech. report CMU-RI-TR-10-04," Robotics Institute, Carnegie Mellon University, , January 2010.

[175] A. Koulaouzidis and A. Karargyris, "Three-dimensional image reconstruction in capsule endoscopy," *World Journal of Gastroenterology,* vol. 18, no. 31, pp. 4086-4090, 2012.

[176] T. Thormahlen, H. Broszio and P. N. Meier, "Three-Dimensional Endoscopy," in *Medical Imaging in Gastroenterology and Hepatology*, Hannover, Germany, Kluwer Academic Publishers, September 2001, p. Falk Symposium No. 124.

[177] D. L. Pham, C. Xu and J. L. Prince, "Current Methods in Medical Image Segmentation," *Annual Review of Biomedical Engineering,* vol. 2, pp. 315-337, 2000.

[178] A. Dufour, V. Shinin, S. Tajbakhsh, N. Guillén-Aghion, J.-C. Olivo-Marin and C. Zimmer, "Segmenting and Tracking Fluorescent Cells in Dynamic 3-D Microscopy With Coupled Active Surfaces," *IEEE Transactions on Image Processing,* vol. 14, no. 9, pp. 1396-1410, 2005.

[179] J. K. Udupa and S. Samarasekera, "Fuzzy Connectedness and Object Definition: Theory, Algorithms, and Applications in Image Segmentation," *Graphical Models and Image Processing,* vol. 58, no. 3, pp. 246-261, 1996.

[180] A. Agarwala, M. Dontcheva, M. Agrawala, S. Drucker, A. Colburn, B. Curless, D. Salesin and M. Cohen, "Interactive Digital Photomontage," in *The Association for Computing Machinery (ACM) SIGGRAPH*, New York, NY, USA , 2004.

[181] K. Doi, "Computer-Aided Diagnosis in Medical Imaging: Historical Review, Current Status and Future Potential," *Computerized Medical Imaging and Graphics,* vol. 31, no. 4-5, p. 198–211, 2007.

[182] M. Liedlgruber and A. Uhl, "Computer-aided Decision Support Systems for Endoscopy in the Gastrointestinal Tract: A Review," *IEEE Reviews in Biomedical Engineering ,* vol. 4, pp. 73-88, 2012.